

**Dynamics of cell contacts during cell intercalation
in epithelial tissue elongation of *Drosophila*
embryos**

Dissertation

for the award of the degree

"Doctor rerum naturalium" (Dr.rer.nat.)

of the Georg-August-Universität Göttingen

within the doctoral program **Biology**

of the Georg-August University School of Science (GAUSS)

submitted by

Deqing Kong

from Shaanxi, China

Göttingen, 2017

Thesis Committee

Prof. Dr. J. Großhans.

Institute for Developmental Biochemistry, Medical School, University of Göttingen.

Prof. Dr. R. Schuh

Department of Molecular Developmental Biology, Max Planck Institute for Biophysical Chemistry, Göttingen.

Prof. Dr. B. Schwappach

Institute for Molecular Biology, Medical School, University of Göttingen.

Members of the Examination Board

Reviewer: Prof. Dr. J. Großhans

Institute for Developmental Biochemistry, Medical School, University of Göttingen.

Second Reviewer: Prof. Dr. R. Schuh

Department of Molecular Developmental Biology, Max Planck Institute for Biophysical Chemistry, Göttingen.

Further members of the Examination Board:

Prof. Dr. F. Wolf

Department of Nonlinear Dynamics, Max Planck Institute for Dynamics and Self-Organization, Göttingen.

Prof. Dr. G. Bucher

Department of Evolutionary Developmental Genetics, University of Göttingen, Göttingen.

PD Dr. H. Shcherbata

Max Planck Research Group of Gene Expression and Signaling, Max Planck Institute for Biophysical Chemistry, Göttingen

Prof. Dr. S. Jakobs

Department of NanoBiophotonic, Max Planck Institute for Biophysical Chemistry, Göttingen

Date of the oral examination: 20.09.2017

AFFIDAVIT

I hereby declare that I prepared the doctoral thesis “Dynamics of cell contacts during cell intercalation in epithelial tissue elongation of *Drosophila* embryos” on my own with no other sources and aids than quoted.

Deqing Kong

Göttingen, 15.08.2017

Acknowledgements

First, I would like to thank my supervisor Prof. Dr. Jörg Großhans for providing me such an interesting topic for my doctoral work. I am very grateful for that he is always available to answer questions, and discuss ideas enthusiastically. His optimism and passion for science are inspiring. I would like to thank Prof. Dr. Fred Wolf and Dr. Lars Reichl. They work with us in a team and provide not only excellent analysis but also deep insight for better understanding our topic as theorists. I am very thankful to my thesis committee members Prof. Reinhard Schuh and Prof. Dr. Blanche Schwappach-Pignataro for their helpful suggestions and constructive criticism during the thesis committee meetings. I would like to express my gratitude to my colleagues for creating an excellent working atmosphere, providing great discussions. I would like to thank Dr. Yujun Zhang, who started this project and helped me a lot in the beginning. I am grateful to Dr. Hung-wei Sung for teaching me the *Drosophila* genetics. I thank Prachi Richa and Anja Schmidt for sharing the data, results and thoughts during Fridays meeting, and also for proofreading my thesis. I thank Dr. Zhiyi Lv for long-term discussing scientific questions during coffee break, although sometimes we have different opinions.

I would like to thank Prof. Tadashi Uemura for sending me E-Cad antibodies, Prof. Andreas Wodarz for the Baz antibodies, Dr. Katrin Willig for the STED imaging, Dr. Marion Silies, Prof. Stefan Luschnig, Prof. Yang Hong, Prof. Masatoshi Takeichi, Prof. Arno Müller Prof. Yuh-Nung Jan and Dr. Jennifer A. Zallen for sharing fly stocks.

Last but not the least, I would like to thank my family for their endless support and for always being there for me.

Table of Contents

ABSTRACT	I
PART I. Dynamics of cell contacts during cell intercalation in epithelial tissue elongation of <i>Drosophila</i> embryos	1
CHAPTER 1. Introduction: Forces directing germ-band extension in <i>Drosophila</i> embryos	3
1.1 Germ-band extension.....	3
1.2 Mechanical coupling of tissues	5
1.3 Anterior-posterior patterning system and polarized cell behaviors.....	10
1.4 Mechanisms of cell rearrangement.....	14
1.5 Junctional E-cadherin during germ-band extension	19
1.6 Oriented cell divisions in germ-band extension	20
1.7 Calcium signaling in germ-band extension	21
1.8 Mathematical models of germ-band extension.....	22
1.9 Concluding remarks	22
1.10 Aim of the work.....	25
CHAPTER 2. Materials and Methods	26
2.1 Materials	26
2.1.1 Oligonucleotides used in the study	26
2.1.2 Antibodies	27
2.1.3 Fly stocks.....	28
2.1.4 Microscopy	30
2.1.5 Software	32
2.2 Molecular biology methods.....	32
2.2.1 Isolation genomic DNA from the adult flies	32
2.2.2 Polymerase chain reaction (PCR).....	33
2.2.3 In-fusion cloning	35

TABLE OF CONTENTS

2.2.4 DNA sequencing	35
2.2.5 <i>In-vitro</i> transcription	35
2.3 Genetic methods.....	36
2.3.1 Generation of <i>xiantuan (xit)</i> genomic transgene fly	36
2.3.2 Generation of germline clones	37
2.3.3 UAS-GAL4 system.....	37
2.4 E-Cadherin RNAi treatment of <i>Drosophila</i> embryos	37
2.5 RNAi treatment and immunostaining of <i>Drosophila</i> cells.....	38
2.6 Fixation of <i>Drosophila</i> embryos	38
2.7 Immunostaining of <i>Drosophila</i> embryos	39
2.8 larval cuticles preparation.....	39
2.9 Western blot	40
2.10 Glycan cleavage with glycosidases.....	41
2.11 Ca ²⁺ uncaging.....	41
2.12 Live-imaging of <i>Drosophila</i> embryos	42
2.13 Laser ablation.....	43
2.14 Fluorescence recovery after photobleaching (FRAP).....	44
CHAPTER 3. The glucosyltransferase Xiantuan is required for germ-band extension and the function of E-Cadherin in <i>Drosophila</i>	45
3.1 <i>xiantuan (xit)</i> is required for gastrulation movements	45
3.2 <i>xit</i> encodes a glucosyl-transferase in the endoplasmic reticulum	45
3.3 <i>xit</i> is required for cell intercalation	49
3.4 <i>xit</i> is specifically required for efficient expression of E-Cadherin.....	53
3.5 <i>xit</i> is required for N-glycosylation of E-Cadherin	55
3.6 Adherens junctions in <i>xit</i> and E-Cadherin RNAi embryos	59
3.7 Developmental control of E-Cadherin mobility is <i>xit</i> dependent	60
3.8 N-Glycosylation of E-Cadherin is important for mechanical signal coupling in neighboring cells	66
3.8.1 Cell behaviors in <i>amnioserosa</i>	66

TABLE OF CONTENTS

3.8.2 Morphology of amnioserosa is affected in <i>xit</i> embryos	68
3.8.3 N-glycosylation of E-Cadherin is required for response of neighboring cells in amnioserosa	69
3.9 Summary	72
CHAPTER 4. Cell-cell coordination drives neighbor exchanges during epithelial tissue morphogenesis.....	74
4.1 Simultaneous contraction of cardinal cells induces junction extension.....	75
4.1.1 Simultaneous contraction of cardinal cells induces junction extension in wild type embryos	75
4.1.2 <i>xit</i> dependent cell-cell coordination	78
4.2 Temporal alignment of T1 transitions reveals long attempt phases and specific area dynamics in <i>xit</i> embryos	80
4.2.1 Diverse behaviors of cell quadruplets	82
4.2.2 Junction dynamics in cell quadruplets during T1	84
4.2.3 Cell area dynamics in cell quadruplets during T1	85
4.3 T1 specific coordinated area fluctuations between old and new neighbors.....	87
4.4 Time-resolved correlation analysis reveals 4x vertex specific	88
4.5 E-Cadherin is involved in coordination.....	90
CHAPTER 5. DISCUSSION.....	91
5.1 Role of N-Glycans in E-Cadherin distribution in <i>Drosophila</i> embryos.	91
5.2 N-glycosylation alters the immobilization of E-Cadherin clusters and E-Cadherin-based mechanotransduction in <i>Drosophila</i> embryos.	93
5.3 Coordinated cell behaviors are important for tissue extension.....	98
PART II. Optochemical control of cell contractility at single cell resolution in <i>Drosophila</i> embryos.....	101
CHAPTER 6. Optochemical control of cell contractility at single cell resolution in <i>Drosophila</i> embryos	103
6.1 Introduction	103

TABLE OF CONTENTS

6.2 Results	105
6.2.1 Uncaging induces rapid Ca²⁺ concentration increase in epithelial cells in <i>Drosophila</i> embryos.	105
6.2.2 Increasing in intracellular Ca²⁺ induces rapid and transient cell contraction	107
6.2.3 Role of Myosin II in Ca²⁺ induced cell contraction	110
6.3 Discussion	111
6.4 Materials and Methods	112
REFERENCES	113
APPENDIX	127
LIST OF FIGURES	141
LIST OF TABLES	145
LIST OF MOVIES	146
ABBREVIATIONS	147
LIST OF PUBLICATIONS	149
CURRICULUM VITAE	150

ABSTRACT

Cell rearrangement is one of the fundamental mechanisms underlying tissue morphogenesis. In epithelial tissues, cells rearrange without losing their tight neighbor interactions by junction remodeling according to a topological T1 transition, i. e. collapse of a junction followed by extension of a new junction in perpendicular orientation. The minimal functional unit are cell quadruplets with two old and two new neighbors. The driving force for junction remodeling is provided by acto-myosin contractility in old neighbors. By now it has been unclear whether non-autonomous mechanism is involved, which coordinate the activities of old and new neighbors.

In my doctoral research I employed *xit* mutant *Drosophila* embryos to study potential non-autonomous mechanism of coordination with cell quadruplets undergoing cell rearrangement. I characterized the phenotypes of *xit* mutants in detail, confirmed the assumed function of Xit as a glucosyl-transferase in the ER and identified E-Cadherin to be hypo-N-glycosylated in *xit* mutants. Hypo-N-glycosylated E-Cadherin is more mobile and shows altered clustering. Germ-band extension and cell intercalation are affected in *xit* embryos, similar to the phenotypes in E-Cadherin RNAi embryos. The T1 process, especially the new junction extension phase is delayed in *xit* mutant embryos. Large-scale data analysis of several hundred cell quadruplets passing through T1 processes revealed a T1 specific and *xit* and E-Cadherin dependent anti-correlation of area fluctuations between old and new neighbors, indicating a function of *xit* and E-Cadherin in coordination behavior of old and new neighbors (Collaboration with Dr. Lars Reichl and Prof. Fred Wolf).

To test whether the observed correlations are functionally relevant I developed an optochemical method by Ca^{2+} uncaging to induce rapid and transient cell contraction at single cell resolution. Inducing cell contraction in T1 cell quadruplets, I found that synchronous contractions of cardinal cells are sufficient for junction extension in wild

ABSTRACT

type but not in *xit* mutant embryos. Furthermore, induced cell contractions in new neighbors interfered with junction extension.

I propose a model that the hypo-N-glycosylation of E-Cadherin affects E-Cad-based mechanotransduction and cell-cell communications in *Drosophila* embryos. E-Cadherin *cis*-interaction could be affected by hypo-N-glycosylation, and E-Cadherin relative bigger cluster can be formed initially, but the increased myosin activity spits, instead of stabilize the cluster as in wild type, and furthermore affects E-Cadherin/F-actin interaction. The E-Cad-based mechanotransduction is affected consequently in *xit* embryos.

PART I

**Dynamics of cell contacts during cell intercalation
in epithelial tissue elongation of *Drosophila*
embryos**

CHAPTER 1. Introduction: Forces directing germ-band extension in *Drosophila* embryos

1.1 Germ-band extension

During animal morphogenesis, elongation of the tissues and the body axis is a recurrent feature. In *Drosophila* early embryo, the developmental mode switches from syncytial to cellular morphology at about two to three hours after fertilization in a process called cellularization. Following cellularization, gastrulation starts with mesoderm invagination (Leptin, 1995). A few minutes later, cell intercalation within the lateral epidermis leading to germ-band extension sets in. The entire process of germ-band extension lasts about 2.5 hours but most of the morphologically visible extension occurs within an initial 45 min rapid phase (Campos-Ortega and Hartenstein, 1997). The rapid phase takes place at embryonic stages 6 to 8 (Figure 1.1A). Germ-band extension is finished in stage 9. At the onset of gastrulation, the embryonic surface consists of a single layer of columnar epithelium with their apical surfaces facing outward (Campos-Ortega and Hartenstein, 1997). At stage 7, morphogenetic movements start to reflect the differential specification of the cells and tissues. The cephalic furrow at about 65% egg length is initiated by the shortening of a single row of cells at the boundary between head and embryonic trunk (germ-band) (Spencer et al., 2015). On the ventral side of the embryo, a stripe of cells with about 18 cells wide and 60 cells long, constituting the mesoderm, invaginates at the beginning of gastrulation ("Gastrulation in *Drosophila*: the formation of the ventral furrow and posterior midgut invaginations.," 1991a; Leptin and Grunewald, 1990). The germ-bands from the left and right side of the embryos will join at the ventral midline covering the invaginated mesoderm. The dorsal-most epidermis that does not participate in germ-band extension develops into the extra-embryonic amnionserosa (AS) (Leptin and Grunewald, 1990) (Figure 1.1B). By the end of stage 8, germ-band elongation has progressed so far as to bring the posterior tip of the germ band to about 60% egg length (Figure 1.1A).

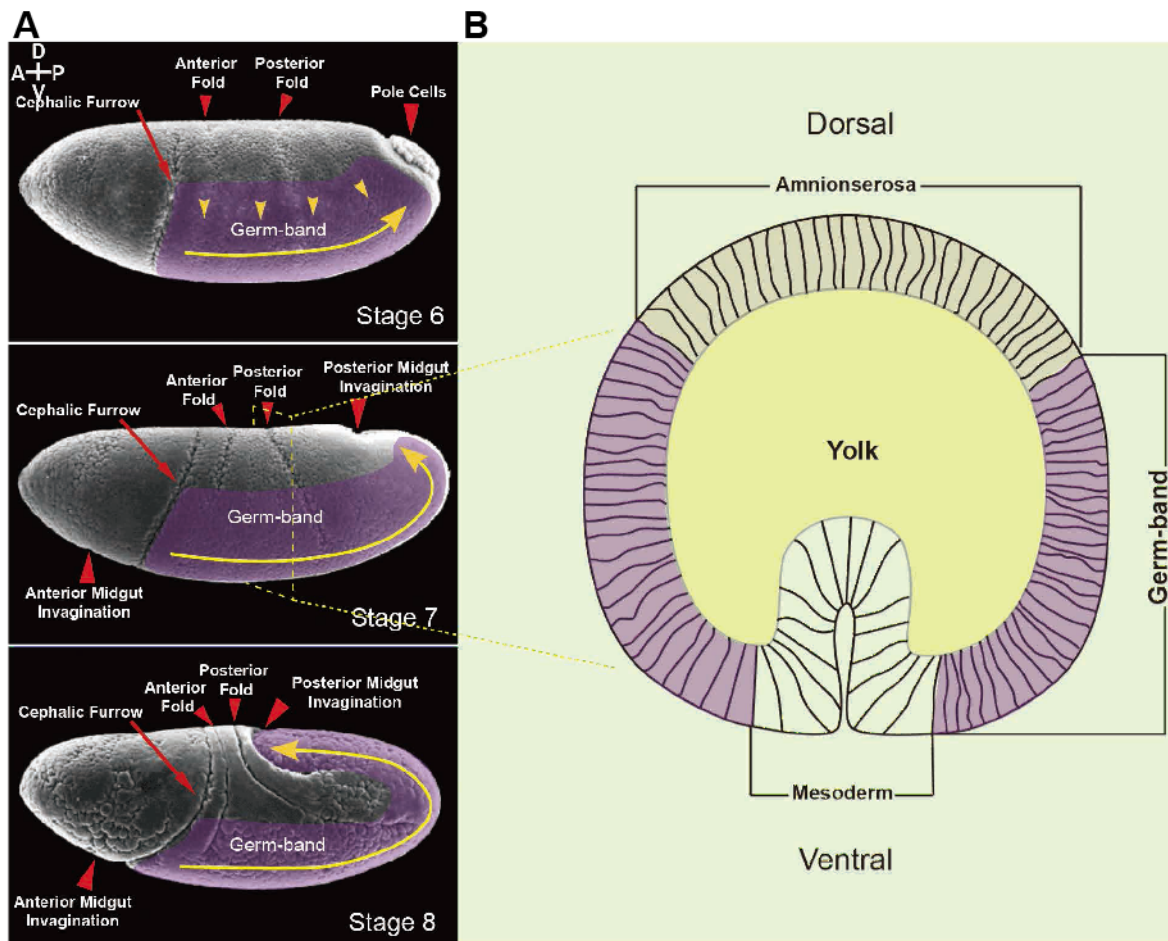


Figure 1.1 *Drosophila* embryonic germ-band extension.

(A) Scanning electron microscopy photomicrographs (from FlyBase (Santos et al., 2015)) showing lateral views of *Drosophila* embryos at stage 6, 7, and 8. The lateral epidermis undergoing convergence-extension is highlighted in light purple. Yellow arrows indicate the direction of extension. (B) Cross-section of a *Drosophila* embryo at stage 7.

As the overall shape and size of the embryo are fixed by the vitelline membrane, the germ-band extends by folding up itself. The posterior end of the germ-band makes a turn towards the dorsal side and subsequently moves in the anterior direction (Campos-Ortega and Hartenstein, 1997). During germ-band extension, the length of the germ-band increases more than two-fold along the anterior-posterior (A-P) axis. Simultaneously, the germ-band narrows along the dorsal-ventral (D-V) axis (Irvine and Wieschaus, 1994) (Figure 1.1A), which is the epithelial form of convergence and extension in embryonic morphogenesis (Keller, 2002). In the germ-band, this dramatic change is locally driven by cell intercalation (Irvine and Wieschaus, 1994). In addition,

the other morphogenetic movements of gastrulation such as invagination of the posterior mid-gut (Collinet et al., 2015; Lye et al., 2015), and possibly the cephalic furrow and dorsal folds contribute by extrinsic pulling forces on the tissue-scale level. This review will focus on the mechanisms of germ-band extension, with an emphasis on the mechanical coupling of tissues (extrinsic tensile forces) and the oriented cell rearrangements guided by the planar-cell polarity (local mechanical forces).

1.2 Mechanical coupling of tissues

The morphogenetic movements of *Drosophila* gastrulation include the germ-band extension, the invagination of mesoderm and endoderm (anterior and posterior midgut invagination), cephalic furrow invagination, and dorsal folds (Figure 1.1A). The key driving force of germ-band extension is polarized cell intercalation, which will be discussed in detail below. Autonomous polarized cell behaviors, however, seem not be sufficient to fully explain germ-band extension (Tepass, 2014). To achieve this, a systems approach considering mechanical interactions within groups of cells and with adjacent tissues is necessary. Such a systems approach has become feasible due to the recent advances in whole embryo imaging with high temporal and spatial resolution. Illustrative of rapid progress in this direction are two recent reports characterizing *Drosophila* gastrulation movements at the whole embryo scale by selective plane illumination microscopy (SPIM) (Lye et al., 2015; Rauzi et al., 2015).

Mesodermal invagination is the first morphogenetic movement during *Drosophila* gastrulation. It is initiated by apical cell contraction of the mesodermal precursor cells at the ventral side of the embryo (Leptin and Grunewald, 1990; Sweeton et al., 1991; Kam et al., 1991). Ventral furrow formation starts about 6 minutes after onset of gastrulation. After another 4–5 minutes, the mesoderm seals at the ventral mid-line (Rauzi et al., 2015). Mesoderm invagination, cephalic furrow formation, endoderm invagination and germ-band extension occur concomitantly. It is an issue of discussion and analysis, to

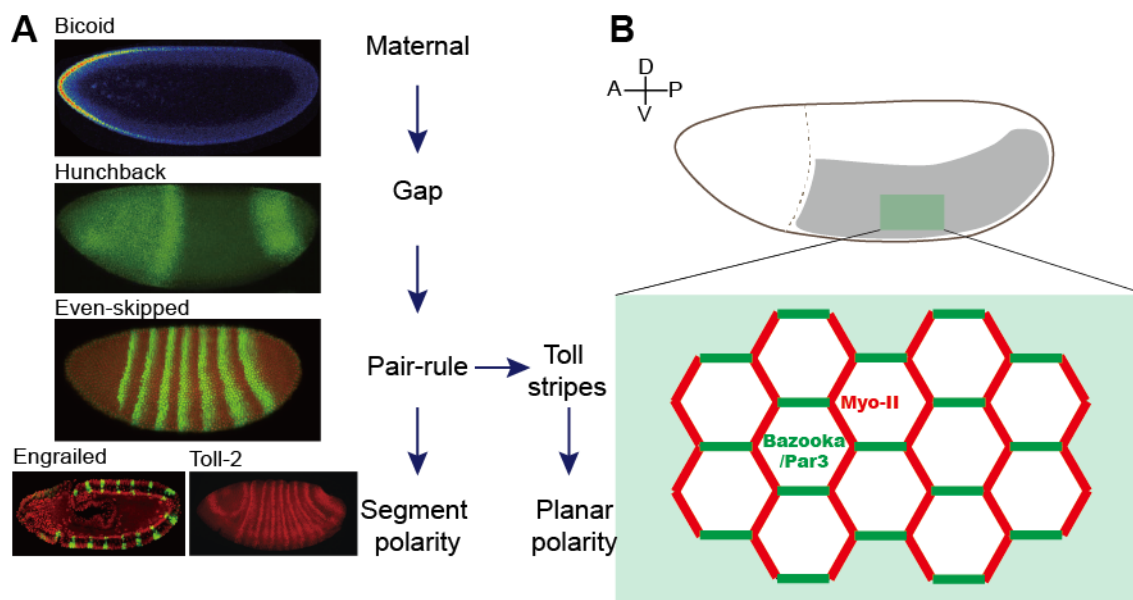


Figure 1.2 Anterior-posterior patterning system and polarized planar polarity.

(A) Anterior-posterior patterning of *Drosophila* embryo is controlled by a hierarchical genetic cascade, which includes coordinate genes for maternal determinants and zygotic gap, pair-rule, and segment polarity genes. Confocal images: Bicoid (Spirov et al., 2009), Hunchback (Perry et al., 2012), Eve, Toll-2 (Paré et al., 2014) and Engrailed. (B) Myosin II is specifically enriched at junctions with dorsal-ventral orientation and Bazooka/PAR-3 is enriched at junctions with anterior-posterior orientation conversely in the intercalating cells during germ-band extension.

which degree this coincidence reflects functional dependencies and interactions. It is, however, well known that germ-band extension is independent of mesoderm invagination since it still timely proceeds in the absence of mesoderm invagination (Irvine and Wieschaus, 1994). In wild type embryos, germ-band extension overlaps with mesoderm internalization for several minutes. Similarly, in *twist snail* double mutant embryos, in which there is no apical cell contraction and no invagination, the displacement of germ-band cells in the first few minutes proceeds as in wild type embryos (Rauzi et al., 2015). Thus, no obvious influence of the mesoderm movements on the germ-band extension has been observed. In contrast, in *twist* mutant embryos, which form a ventral groove that does not invaginate, the cell shape changes but not cell rearrangement in the lateral epidermis is reduced during germ-band extension. This reveals that tensile forces originating from the mesoderm anlage can in principle

influence the lateral epidermis (Butler et al., 2009). More subtle, additional contributions of the ventral furrow on the germ-band extension cannot be ruled out (Lye et al., 2015).

The morphologically visible germ-band extension is driven by cell intercalation and cell shape changes (Butler et al., 2009; Irvine and Wieschaus, 1994) (Figure 1.3). These two contributions can be separated and are genetically independently controlled. Some signs of germ-band extension can be observed in the absence of cell intercalation in mutants with impaired planar polarity, such as those affecting the gap gene *Krüppel* (Bertet et al., 2004; Butler et al., 2009), the pair-rule genes (Irvine and Wieschaus, 1994), and the polarity gene *Bazooka/Par3* (Blankenship et al., 2006a; Zallen and Wieschaus, 2004). In contrast, embryos lacking planar polarity, cephalic furrow, and endoderm invagination (embryos from *bicoid nanos torso-like* females) do not show any signs of germ-band extension (Irvine and Wieschaus, 1994; Zallen and Wieschaus, 2004). The dorsal-anterior movement of the posterior pole is blocked in embryos with no posterior midgut invagination (from the *torso* mutant females) (Irvine and Wieschaus, 1994; Schupbach and Wieschaus, 1986). Importantly, cell intercalation occurs in these embryos (Collinet et al., 2015). The later findings suggest that additional extrinsic forces originating from gastrulation movements may contribute to the germ-band extension. Recent studies have provided the first insights how extrinsic pulling forces originated from the posterior midgut (PMG) invagination can actively contribute to the germ-band extension in tissue scale by simulations and experiments (Collinet et al., 2015). By the end of mesoderm internalization, the posterior midgut has already begun to move dorsally preceding the onset of ectodermal cell intercalation (Rauzi et al., 2015), while germ-band extension has already started for several minutes. Tissue elongation is reduced markedly in embryos in which the anterior-posterior tissue displacement is blocked physically by attachment to the egg shell (Collinet et al., 2015).

During the first 15 minutes of germ-band extension, the lateral epidermal cells are stretched gradually towards the posterior tip of the embryos. This AP cell stretching is due to mechanical coupling with endoderm invagination (Figure 1.3B). Laser cutting

experiments revealed that the mechanical tension increases along the AP axis in wild type embryos during germ-band extension but not in embryos from *torso* females, which lack the posterior midgut (Collinet et al., 2015). This indicates that the posterior endoderm invagination generates an anisotropic mechanical tension in the germ-band. This view is supported by the observation of a myosin II flow towards the presumptive posterior endoderm in acellular embryos (Lye et al., 2015). The PMG generated anisotropic tension introduces a transient and graded AP cell stretching, which rapidly disappears after about 15 minutes of germ-band extension. Cell stretching is present in *eve* mutants (Butler et al., 2009), which have impaired planar polarity and lack cell intercalation. The transient nature of cell stretching suggests that cell intercalation relaxes this anisotropic mechanical tension. Furthermore, the orientation of newly forming junctions is more oblique in *torso* mutants compared to wild type, suggesting that the PMG generated anisotropic tension contributes to the orientation of new AP junctions (Collinet et al., 2015). In summary, a PMG generated anisotropic tension contributes to germ-band extension by initial anterior-posterior cell stretching and orienting junction growth.

The initial steps of cephalic furrow formation coincide with ventral furrow formation (Spencer et al., 2015). The cephalic furrow marks the boundary between the procephalon and the segmented germ-band (González-Reyes and Morata, 1991; A. Vincent et al., 1997) (Figure 1.1A). Cell shape changes at the anterior end of the germ-band may thus be affected by the forming cephalic furrow (Butler et al., 2009). However, the mechanics of the interaction and the functional relationship between cephalic furrow formation and germ-band extension have not yet been addressed.

The dorsal transverse folds are another morphogenetic movement in early gastrulation. These two folds depend on epithelial polarity and anterior–posterior patterning (Wang et al., 2012) (Figure 1.1A). Although the initial signs of the dorsal

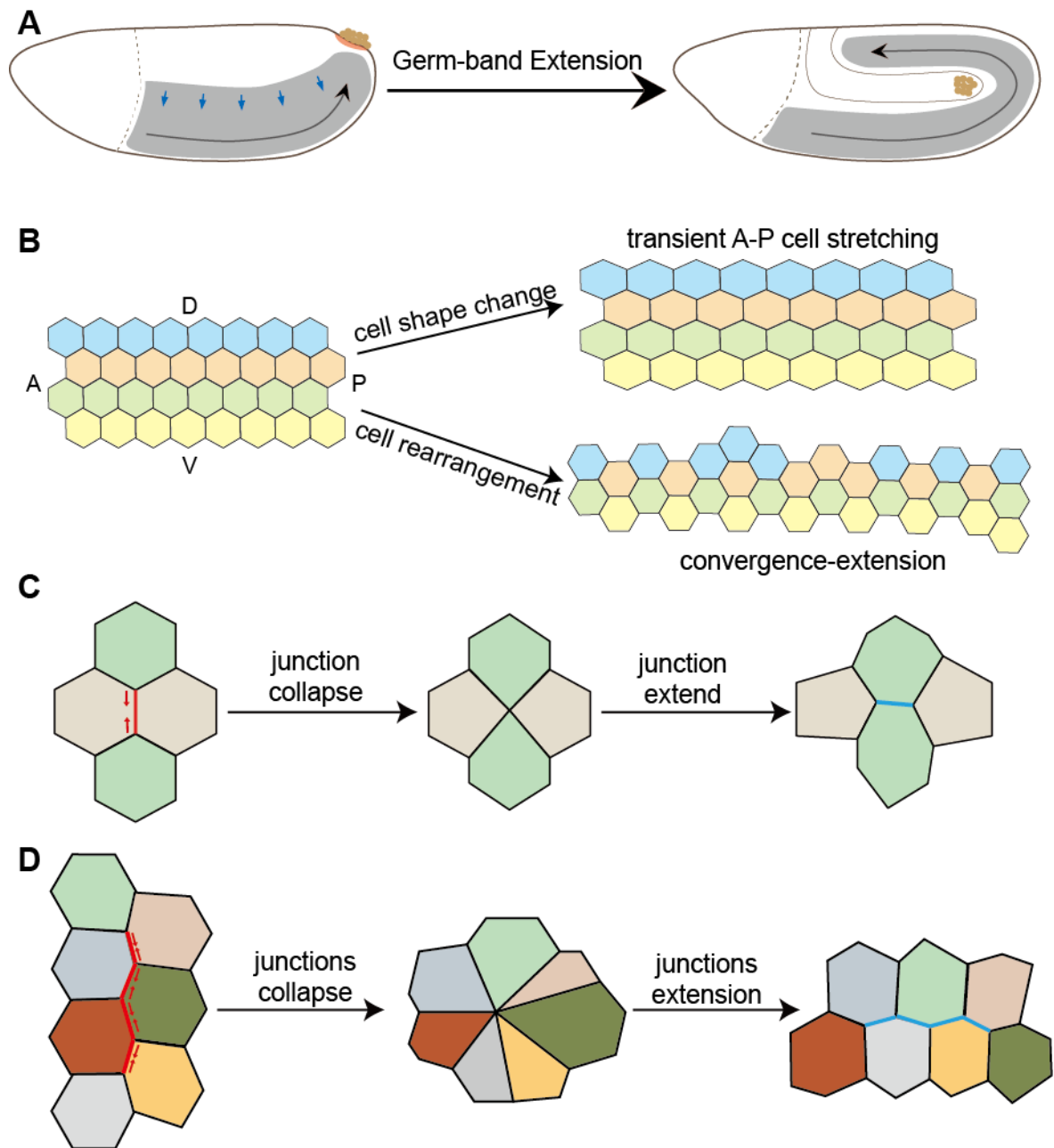


Figure 1.3 Germ-band extension is driven by cell intercalation.

(A) Convergence-extension of lateral epidermis during germ-band extension. (B) Forces directing the lateral epithelial tissue deformation during germ-band extension. The tensile force from posterior midgut invagination (PMI) induces the lateral epithelial cells stretching in A-P direction transiently and tissue convergence and extension are driven by cell intercalation. (C) The key to neighbor exchanges in germ band is junction dynamics according to a topological T1 transition. During T1 transitions, the collapse of a junction with dorsal-ventral orientation (vertical) (red) forms a 4x vertex and a new junction (blue) grows in perpendicular orientation subsequently. (D) Multiple junctions with dorsal-ventral orientation (vertical) (red) collapse to form the rosette and it is resolved by the extension of multiple new junctions (blue) in anterior-posterior orientation. Intrinsic forces are indicated by red arrows in C and D.

folds appear slightly earlier than the onset of germ-band extension, they do not seem to contribute to germ-band extension (Lye et al., 2015). The transformation of the amnioserosa (AS) from a columnar to a squamous epithelium proceeds concomitantly with later steps of germ-band extension. It is conceivable that the DV convergence of the extending germ-band mechanically pulls on the AS and promotes the flattening of the AS cells (Pope and Harris, 2008).

1.3 Anterior-posterior patterning system and polarized cell behaviors

Anterior-posterior (AP) patterning genes are necessary for *Drosophila* germ-band extension (Irvine and Wieschaus, 1994). The AP patterning cascade imposes a pattern of planar polarity on the tissue, which guides the directionality of cell intercalation. AP patterning of *Drosophila* embryo is controlled by a hierarchical genetic cascade, which includes coordinate genes for maternal determinants and zygotic gap, pair-rule and segment polarity genes (Nasiadka et al., 2002) (Figure 1.2A). Germ-band extension, cell intercalation, and directionality of cell behavior are disrupted in *bicoid nanos torso-like* mutants, which completely lack any anterior-posterior pattern (Blankenship et al., 2006a; Irvine and Wieschaus, 1994; Y. Zhang et al., 2014). The gap gene *Krüppel* (*Kr*) specifies thoracic and abdominal segments in the central region of germ-band (Gaul et al., 1987; Small et al., 1991). In *Kr* mutant embryos, germ-band extension and cell intercalation are impaired in the central region of the germ-band (Bertet et al., 2004; Butler et al., 2009; Irvine and Wieschaus, 1994). Similarly, the primary pair-rule genes *even-skipped* (*eve*), *runt* and *hairy* are required for polarization of the tissue and directional cell intercalation (Irvine and Wieschaus, 1994).

A link between patterning and planar tissue polarity was revealed by a recent study, that found members of the family of Toll receptor proteins mediating patterning and tissue polarity (Paré et al., 2014). Similar to *eve* and *runt*, members of the *Toll* family are expressed in stripes along the anterior–posterior body axis (Eldon et al., 1994; Kambris et al., 2002), *Toll-2* and *Toll-8* are expressed in non-overlapping stripes. The striped

pattern is lost in embryos depleted for *eve/runt* RNAi. Importantly, Toll-2, Toll-6, and Toll-8 cooperate to translate the striped pattern into planar polarity as indicated by polarized cell intercalation (Paré et al., 2014). A recent study revealed that this *Toll* subfamily is expressed in stripes during germ-band extension in seven diverse arthropods, and are also required for germ-band elongation in *Tribolium* and in *Parasteatoda* (Benton et al., 2016). These observations suggest that *Toll* family members have a conserved function in axis elongation beside their established function in immunity.

Epithelial planar cell polarity is a tissue-level phenomenon of coordinating two-dimensional cell behavior (Chae et al., 1999; Curtin et al., 2003). Polarized cell behaviors during germ-band extension include cell intercalation. The polarized cell rearrangements are associated with the localization, dynamics, and activity of non-muscle myosin II, which is a force-generating motor protein in the contractile actomyosin network. Myosin II and F-actin are specifically enriched at junctions with dorsal-ventral orientation or parallel to the dorsal-ventral axis (Bertet et al., 2004; Zallen and Wieschaus, 2004; Blankenship et al., 2006). Conversely, Bazooka(Baz)/PAR-3 and adherens junction proteins are enriched at junctions with anterior-posterior orientation (Bertet et al., 2004; de Matos Simões et al., 2010; Levayer and Lecuit, 2013; Levayer et al., 2011; Tamada et al., 2012; Tamada and Zallen, 2015; Zallen and Wieschaus, 2004) (Figure 1.2B). Evidence from biophysical experiments indicates that a mechanical feedback mechanism organizes contractility to generate multicellular myosin cables of dorsal-ventral orientation (Rauzi et al., 2008).

Toll-2, 6, 8 redundantly function to generate planar polarity in the lateral epidermis. Similar to *runt* and *eve* mutants (Zallen and Wieschaus, 2004), the anisotropic distribution of myosin II and Baz/Par-3 is impaired in *Toll-2,6,8* triple mutants (Paré et al., 2014). In wild type embryos, cells express Toll-2 (Figure 1.2A), Toll-6 and Toll-8 in stripes in different registers along the anterior-posterior axis. The combinations generate various interfaces between stripes with heterophilic interactions between the different Toll variants. Heterophilic interactions between Toll receptors, observed in cultured cells,

are predicted to activate myosin II at junctions of dorsal-ventral orientation (Paré et al., 2014). However, the cell intercalation and planar polarity phenotype of *Toll-2,6,8* triple mutants appear weaker than the *eve* phenotype, which may indicate that additional pathways control planar polarity in parallel to Toll signaling (Paré et al., 2014).

In many tissues, planar cell polarity (PCP) is controlled by the conserved Frizzled-dependent signaling pathway (Yang and Mlodzik, 2015), which controls oriented cell rearrangements, including convergent extension (Perrimon and Mahowald, 1987; Walck-Shannon and Hardin, 2014). Toll-dependent PCP constitutes an alternative pathway. It is a matter of current discussion whether Frizzled-dependent PCP is involved in the polarization of the lateral epidermis during gastrulation. Germ-band extension proceeds normally in the embryos lacking Frizzled and Frizzled2 receptors or Dishevelled (Zallen and Wieschaus, 2004). In contrast, a recent study reported that the Frizzled-dependent PCP pathway contributes to the anisotropic distribution of E-cadherin (E-Cad), myosin II, and Baz/PAR-3 in the germ-band at stage 8 (Warrington et al., 2013). Since the absence of *Toll-2,6,8* only weakens the anisotropic localization of myosin II and Baz/PAR-3, it is conceivable that Frizzled and Toll-dependent PCP may cooperate and redundantly function in generation and maintenance of polarized localization of E-Cad/myosin II/PAR-3 (Tepass, 2014).

The complementary polarized localization of myosin II versus Baz/PAR-3 and adherens junction proteins are necessary for polarized cell behaviors during tissue elongation (Figure 1.2B). The Rho signaling pathway is important for this polarization (de Matos Simões et al., 2010; Simões et al., 2014). Activated Rho1 at cell borders with dorsal-ventral orientation (vertical) plays several roles in polarized cell behaviors: (1) it initiates myosin II accumulation at the cell contacts with dorsal-ventral orientation via Rho-kinase (de Matos Simões et al., 2010; Simões et al., 2014), (2) it activates the formin Diaphanous (Dia), which decreases α -catenin accumulation at the cell contacts with dorsal-ventral orientation by initiating E-Cad endocytosis (Levayer et al., 2011), (3) it induces the Baz/PAR-3 protein dissociation from the junctions with dorsal-ventral

orientation, leading to lower levels than at the junctions with anterior-posterior orientation (horizontal) (de Matos Simões et al., 2010; Simões et al., 2014). The high levels of Baz/PAR-3 at the junctions with anterior-posterior orientation further stabilizes the adherens junction complexes and reinforce a polarized distribution of E-Cad (de Matos Simões et al., 2010; Levayer et al., 2011; Simões et al., 2014). Interestingly, Toll-2 can act and regulate myosin II by the Rho-GTPase pathway during salivary-gland morphogenesis (Kolesnikov and Beckendorf, 2007). A similar mechanism may link A-P patterning with planar polarity in the germ-band. Recent studies revealed that the Rho1-Rok pathway controls myosin II polarity by regulating myosin II regulatory light chain (RLC) phosphorylation (Kasza et al., 2014; Munjal et al., 2015). Quantitative live imaging and biophysical approaches revealed that both un-phosphorylatable RLC and phosphomimetic RLC reduce myosin planar polarity and mechanical anisotropy and consequently affect the directionality cell rearrangements during germ-band elongation (Kasza et al., 2014). Furthermore, spatial control over RLC phosphorylation–dephosphorylation cycles is required for myosin II anisotropy (Munjal et al., 2015). An asymmetrically localized actin- and Rho-kinase–binding protein, Shroom, enhances Rho-kinase and polarized junctional localization of myosin II (Simões et al., 2014). In addition, fluorescence recovery after photobleaching experiments showed that myosin II is stabilized at the cortex in regions of increased tension, and the dynamics of myosin II are regulated by tension in a positive feedback loop (Fernandez-Gonzalez et al., 2009). Live-imaging studies uncovered a flow of medial myosin II towards AP junctions that may generate the forces ultimately leading to junction constriction, which suggests that the dynamics of medial-cortical myosin II is involved in the myosin II polarized distribution (Levayer and Lecuit, 2013; Rauzi et al., 2010). Taken together, the Rho signaling pathway is required for the polarized localization of myosin II versus Baz/PAR-3 and adherens junction proteins, in addition, the mechanical feedback and medial myosin II flow are involved in the myosin II polarization.

Baz/PAR-3 is a multi-PDZ domain protein at the subapical region of epithelial cells. Bazooka recruits E-Cad into sub-apical spot junctions during cellularization. In this

manner, it is involved in establishing initial epithelial apical-basal polarity and adherens junction formation (Harris and Peifer, 2005; 2004; Morais-de-Sá et al., 2010). Coimmunoprecipitation showed the *in vivo* interaction between Baz and Armadillo (β -catenin in *Drosophila*) (Wei et al., 2005). During germ-band extension, Baz/PAR-3 preferentially accumulates at adherens junctions of anterior-posterior orientation (de Matos Simões et al., 2010) (Figure 1.2B). The polarized accumulation of Baz requires its C-terminal domain, which can be phosphorylated by Rho-kinase. It is assumed that phosphorylation of the Baz C-terminal domain inhibits its interaction with phosphoinositide membrane lipids and antagonizes its accumulation at junctions in dorsal-ventral orientation (de Matos Simões et al., 2010). In addition, the Abl tyrosine kinase contributes to the anisotropic distribution of β -catenin, which is slightly enriched at junctions of dorsal-ventral orientation. Abl enhances β -catenin turnover at the anterior-posterior cell junctions by phosphorylation of β -catenin on the tyrosine 667 (Tamada et al., 2012). In *abl* mutants, Baz polarization is reduced and rosette formation is impaired, which may be the reason for the defective germ-band extension (Tamada et al., 2012). Interestingly, mechanical forces can enhance the β -catenin phosphorylation in APC^{1638N/+} mouse colon (Whitehead et al., 2008), and laser ablation experiments show that the anterior-posterior cell borders are under high mechanical tension during rosette formation (Fernandez-Gonzalez et al., 2009). It is conceivable that high mechanical tension enhances β -catenin phosphorylation and turnover. Such a mechanical link to the distribution of junction proteins may constitute a feedback loop that enhances an anisotropic distribution.

1.4 Mechanisms of cell rearrangement

Directional cell rearrangement by the local neighbor exchange is the fundamental cellular event in germ-band extension (Figure 1.3). The epithelial cells ultimately interpose themselves between their neighbors. This decreases the width of the germ-band along the dorsal-ventral (DV) axis and increases its length along the anterior–posterior (AP) axis (Irvine and Wieschaus, 1994), constituting a convergence–extension

movement. In contrast to non-epithelial tissues, active cell movement relative to neighbors is not possible in the lateral epidermis as the epithelial cell-cell contact must not be weakened at any time during the intercalation process. The key to neighbor exchanges in epithelial tissue is junction remodeling, realizing topological T1 transitions (“Soap, cells and statistics—random patterns in two dimensions,” 2006). T1 transitions consist of two phases: (1) collapse of a junction with dorsal-ventral orientation (vertical) with fusion of two 3x vertices into a single 4x vertex, (2) expansion of a new junction with anterior-posterior orientation (horizontal) in perpendicular orientation by splitting of the 4x vertex into two 3x vertices (Figure 1.3C). In the lateral epidermis, the initial collapse concerns junctions of dorsal-ventral orientation (vertical) and new junctions expand in an anterior-posterior direction (horizontal) (Bertet et al., 2004).

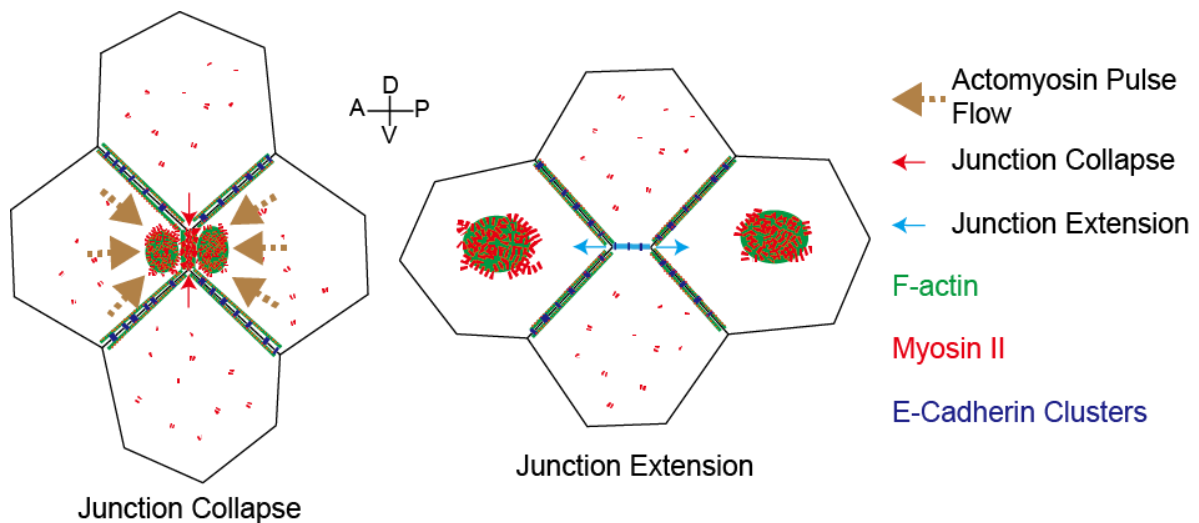


Figure 1.4 Actomyosin dynamics within the cell quadruplets during the T1 transition.

In addition to junctional myosin, pulsed cortical actomyosin clusters flow towards a vertical junction, where constricting forces are generated during junction collapse. The cortical actomyosin network generates forces (red arrows) in the old neighbors, which lead the cell contraction to promote the new junction extension (indicated by light blue arrows).

During the past decade several studies started to elucidate the mechanics of junction collapse, identifying a central role for localization, dynamics and activity of nonmuscle myosin II and the junction associated actomyosin network (Bertet et al., 2004; Fernandez-Gonzalez et al., 2009; Rauzi et al., 2010; Zallen and Wieschaus, 2004). Myosin II is a motor protein that hydrolyzes ATP to move along actin filaments. Inactive

myosin II is a hexameric complex, consisting of two heavy chains, two essential light chains (ELC) and two regulatory light chains (RLC) (Hartman and Spudich, 2012). *In vitro* studies reveal that the assembly of myo II mini-filaments and their movement along actin filaments is promoted by the phosphorylation of the myosin II RLC (encoded by *spaghetti squash* in *Drosophila*) at S21 and T20 (Jordan and Karess, 1997; Sellers et al., 1985; H. Suzuki et al., 1978; Winter et al., 2001). During germ-band extension, RLC is phosphorylated by Rho-kinase (de Matos Simões et al., 2010), which itself is activated by the Rho1-Rok pathway and GPRC signaling (Kerridge et al., 2016).

During T1 transitions myosin II is enriched at apical adherens junctions of cell contacts of dorsal-ventral orientation (Figure 1.2B, Figure 1.4). Activated myosin II generates the force for junction collapse. Laser ablation of junctions and actomyosin filaments revealed that the junctions in dorsal-ventral orientation are in general under higher tension than junctions in anterior-posterior orientation (Fernandez-Gonzalez et al., 2009; Rauzi et al., 2008). In addition to adherens junctions, myosin II is also enriched in the apical cortex of the cells (cortical-medial myosin II). The polarized flow of cortical actomyosin clusters towards junctions promotes junction collapse (Rauzi et al., 2010) (Figure 1.4). Thus, the force for junction collapse is generated by contracting actomyosin at adherens junctions but also involves the flow of cortical actomyosin clusters towards the collapsing junctions. Rauzi et al. used live-imaging to examine in two pools of myosin II in intercalating cells: the cortical-medial and the junctional pool. Both medial and junctional myosin II display pulsed dynamics. Junctional myosin II intensity overall increases gradually as vertical junctions constrict. During the constricting however they find successive steps of shrinkage and arrest. Medial myosin II anisotropic flow contributes to the increase of junctional myosin (Rauzi et al., 2010). In a given cell, the flow of myosin II was observed towards both junctions of dorsal-ventral orientation with a change in direction with a period of 60–180 s. This flow correlates with fluctuations of E-Cad intensity at the junctions (Levayer and Lecuit, 2013). These E-Cad asymmetries are transient and alternate between the two junctions in dorsal-ventral orientation. The E-Cad fluctuations are due to clathrin-mediated endocytosis and amplified by the

actomyosin flow (Levayer and Lecuit, 2013). Similarly, during *Drosophila* embryonic wound repair, polarized vesicle trafficking of E-Cad directs actomyosin remodeling (M. V. Hunter et al., 2015). Position- and direction-selective laser ablation showed that cortical flow generates anisotropies in cortical tension in *C. elegans* zygote, in which the constitutive mechanical properties of the cortex are largely isotropic (Mayer et al., 2010).

Two recent studies started to investigate the mechanics of new junction formation during the extension phase of a T1 transition (Collinet et al., 2015; Yu and Fernandez-Gonzalez, 2016). More than the collapse phase, the extension phase coincides with the period of morphologically visible tissue elongation. Formation and extension of the new junctions apparently require pulsed contractions of cortical-medial actomyosin clusters (Figure 1.4) and Rho-kinase in the old neighbors (Collinet et al., 2015; Yu and Fernandez-Gonzalez, 2016). Laser ablation experiments showed that newly forming horizontal cell junctions are under higher tension during T1 transitions than the stationary junctions with anterior-posterior orientation (Yu and Fernandez-Gonzalez, 2016). Ectopic tension triggered by wounds introduced by UV-laser in the dorsal and ventral cell at the 4x vertex stage could initiate junction growth along the dorsal-ventral direction in wild type embryos during germ-band extension (Yu and Fernandez-Gonzalez, 2016).

Based on live-imaging, it has been proposed that new junctions during the extension phase undergo cycles of elongation and shorting. Quantification of selected cases supports the notion that pulses in junction length correlate with fluctuations of the cross-sectional area in the old neighbors (Yu and Fernandez-Gonzalez, 2016). The area fluctuations are assumed to be caused by pulsed contractions of the cortical-medial actomyosin network (Fernandez-Gonzalez and Zallen, 2011; Sawyer et al., 2011). The actomyosin network pulses coincide with cell shape change leading to cell elongation in A/P axis as well (Fernandez-Gonzalez and Zallen, 2011; Sawyer et al., 2011). Blocking contractile activity by Y-27632 or Cytochalasin D injection leads to an impaired extension phase (Yu and Fernandez-Gonzalez, 2016). Since the inhibitors were applied globally,

it is not clear, in which cells contractility is necessary. Likely, contractility is required in A and P cells, as these show the correlated area changes. But contractility seems also to be important in the D and V cells. Junction extension fails, when the cortical-medial actomyosin network is damaged by UV laser dissection specifically in the D and V cells (Yu and Fernandez-Gonzalez, 2016). These observations suggest that tension or contractility in the D or V cells is necessary for the extension phase. A conceivable interpretation is provided by an *in vitro* study that revealed that high tension on the actin filaments enhances the binding between actin filaments and the minimal cadherin-catenin complex (Buckley et al., 2014). In cultured cells, a mechanical tugging force in two adjacent cells is sufficient to trigger the growth of the adherens junction (Liu et al., 2010). In a pair of suspended culture cells, the contraction of the actomyosin network is necessary for maintaining the size of the adherens junctions and the immobilization of E-Cad (Engl et al., 2014). Taken together, tension or cell contraction contributes to junction growth. For the case of a T1 transition, it remains open how the actomyosin network contributes to the extension phase. It is likely that actomyosin in the DV cells serves a different function than in the AP cells, where contractility controls area changes.

Cell intercalation through rosettes involving up to 8–10 cells presents a more complex version of cell intercalation than a plain T1 transition (Figure 1.3D). Rosettes are observed during germ-band extension, especially at stage 8 (Blankenship et al., 2006a; Lye and Sanson, 2011; Vichas and Zallen, 2011; Walck-Shannon and Hardin, 2014). Similar to the cell quadruplets engaged in a T1 transition, multiple junctions collapse simultaneously along the dorsal-ventral axis and multiple 3x vertices fuse to a rosette structure. Subsequently, a rosette resolves by the formation of multiple new junctions along the anterior-posterior axis (Figure 1.3D). Similar to generic T1 transitions, the collapse of multiple dorsal-ventral cell junctions into a rosette requires polarized F-actin and myosin II cable at the shrinking junctions, which depend on the activity of polarized Rho-kinase (Blankenship et al., 2006a; de Matos Simões et al., 2010; Fernandez-Gonzalez et al., 2009). However, *abl* mutant embryos, in which β -catenin turnover is reduced at the anterior-posterior cell borders, shows defects of vertical

junction shrinkage during rosette formation but not for T1 transitions (Tamada et al., 2012). This suggests specific regulatory mechanisms for the rosette formation compared with T1 transition. E-Cad, F-actin and Bazooka localize in a spatially and temporally regulated manner to newly forming junctions during rosette resolution (Blankenship et al., 2006a). However, the detailed mechanisms remain unclear.

1.5 Junctional E-cadherin during germ-band extension

Within adherens junctions, homotypic interactions between E-Cad molecules link epithelial cells and are thus a central player in epithelial tissue morphogenesis. As in many cell types, E-Cad molecules do not distribute uniformly at the adherens junction, but form clusters in *Drosophila* epithelial cells during germ-band extension (Cavey et al., 2008). Superresolution images showed that E-Cad molecules form clusters in separated membranes by E-Cad *cis*-interaction in *Drosophila* embryos by photoactivated localization microscopy (PALM), forth more, the molecules density analysis suggested that 25% in average of E-Cad molecules in clusters are in *cis*-interaction at adherens junction in *Drosophila* embryos (Truong Quang et al., 2013). E-Cad clusters are linked to the actin cytoskeleton via β -catenin and α -catenin, which binds F-actin as well as F-actin binding proteins, such as vinculin (Takeichi, 2014). During germ-band extension, the molecular machinery of adherens junctions is remodeled in conjunction with junction dynamics. E-Cad complexes are thought to orient the actomyosin flow direction (Levayer and Lecuit, 2013). It is unclear, however, to which degree E-Cad remodeling plays an instructive role. Recent studies revealed that E-Cad does not act as a driving force during the contact extension phase but rather stabilizes new cell contacts once they are formed (Collinet et al., 2015). In addition to stabilization of cell-cell contacts, E-Cad based adherens junctions transmit the forces between the neighboring cells during tissue remodeling (Hoffman and Yap, 2015). Potentially, E-Cad may have roles in new junction formation during T1 transitions, in addition to stabilizing the cell contacts. Cell intercalation is specifically delayed during the new junction formation phase in mutants with hypo-N-glycosylated E-Cad but without obvious epithelial defects (Y. Zhang et al.,

2014). Furthermore, at the onset of germ-band extension, anisotropic tension along the A-P body axis leads to an A-P stretching of the lateral epidermal cells with a gradual increase towards the posterior tip of the embryos. Cell stretching is reduced when cell intercalation occurs, whereas the anisotropic tension is still detected (Collinet et al., 2015; Lye et al., 2015). It needs to be investigated if or how adherens junctions and E-Cad are involved in the force transmission and coordination on a tissue wide scale.

1.6 Oriented cell divisions in germ-band extension

Oriented cell division is a mechanism involved in patterning and shaping a tissue during development (Nicholas D Poulson, 2012). Several studies have assessed the contribution of cell rearrangements for germ-band extension (Bertet et al., 2004; Irvine and Wieschaus, 1994; Zallen and Wieschaus, 2004). These observations were focused on the anterior part of germ-band, where no cell divisions occur during the rapid phase of germ-band extension (Foe, 1989). One study has highlighted a potential role of oriented cell divisions in the region next to the posterior mid-gut invagination (mitotic domain 4). Based on the observation that the cell divisions were oriented towards the invaginating endoderm along the axis of elongation, it was proposed that oriented cell divisions contribute to germ-band extension both in the rapid phase and the slow phase (da Silva and J. P. Vincent, 2007). The rapid phase of germ-band extension occurs at the initial 45 min, the tip of the germ-band extends to 60% EL (embryo length), and the germ-band continues to extend until the tip reaches to 75% EL at the slow phase in the following 100 min (Campos-Ortega and Hartenstein, 1997). Oriented cell division in the posterior germ-band would drive the rapid phase of axis elongation, while cell intercalation occurs mainly in the anterior portion of the germ-band. The extent of axis elongation is reduced in mutants without zygotic cell divisions. The mechanism that leads to oriented divisions in mitotic domain 4 remains unclear. The divisions might be oriented by a planar cell polarity pathway or the mechanics of the extending tissue and force generated by endoderm invagination. There is currently no evidence for the first model. The frizzled-dependent PCP pathway is not required for oriented cell divisions in

the posterior region (da Silva and J. P. Vincent, 2007). The alternative model is more likely, since the invaginating posterior endoderm produces tensile stress in the germ-band at the posterior end of the embryo (Lye et al., 2015). It is conceivable that the mitotic spindles of dividing cells orient guided by anisotropic tissue tension similar to tension-oriented cell divisions during zebrafish epiboly (Campinho et al., 2013).

1.7 Calcium signaling in germ-band extension

Calcium is involved in many cellular processes, including cytoskeletal dynamics and cell shape changes. Global perturbation of intracellular calcium impairs egg chamber elongation in *Drosophila* oogenesis, for example (He et al., 2010). Similarly, an increase in intracellular free calcium concentration by UV uncaging of caged compounds induces cell shape change in the amnioserosa of *Drosophila* embryos (G. L. Hunter et al., 2014). It is unclear how calcium is linked to cell behavior and contractility. A potential mechanism is provided by calmodulin complexes that activate the myosin light chain kinase and consequently myosin II (Kitazawa et al., 1991). Employing live-imaging of calcium-sensitive fluorescent probes, the dynamics of calcium ions can be investigated *in vivo*. Live-imaging of the calcium probe G-CaMP3-GFP revealed that wounds cause an increase of intracellular calcium in the *Drosophila* pupa (Antunes et al., 2013). A wave of high calcium levels was observed toward the wound center during wound healing (Antunes et al., 2013). During germ-band extension spontaneous calcium spikes were observed both in individual cells and in groups of cells (Markova et al., 2015). The frequency of calcium spikes increases during the fast phase of germ-band extension. However, no correlation with T1 processes and stereotypic cell and junction dynamics was observed. It remains to be investigated, whether and how the prominent calcium spikes or less obvious changes in calcium concentration contribute to cell and junction dynamics during germ-band extension.

1.8 Mathematical models of germ-band extension

The individual T1 transitions of cell quadruplets are the basic units of a complex morphological process involving many hundreds of cells. Although the T1 transitions have been treated as deterministic processes, it is obvious from observation on tissue level that a stochastic component is involved and that tissue behavior cannot be predicted from the individual T1 process. It is not possible to predict the timing and positions of T1 processes within the tissue. They proceed in an apparently random pattern. What is missing is a link between the stereotypic behaviors of cell quadruplets with morphogenesis on tissue level? Theoretical models have been developed to describe the process of germ-band extension and relationship of the factors. According to one model, the collapse of junctions during T1 transition, as well as the more complex variant of rosettes, is due to anisotropic tension between the collapsing and neighboring junctions, which leads as a necessary consequence to the resolution of the 4x vertex by a new junction (Rauzi et al., 2008). In a more recent research, the authors proposed an integral model that couples the polarity of signaling proteins (Shroom, Rho-kinase, myosin etc.) and mechanical forces, which agrees with the experimental data (Lan et al., 2015).

1.9 Concluding remarks

The anterior-posterior patterning system establishes in the lateral epidermis a system of planar cell polarity, which directs junctional, and cytoskeletal dynamics and cell rearrangement. The directional cell behavior is due to anisotropic actomyosin contractility and the distribution of cortical proteins, generating tensile stresses. In this review, we have summarized the literature on how these factors contribute to germ-band extension and discuss open questions in our current understanding of this process.

The finding that Toll-family proteins are involved in polarization of the tissue, has started to open the black box of the molecular links between the transcriptional machinery of the anterior-posterior patterning system and the cell biology of

mechanically active cell behavior (Paré et al., 2014). Some evidence supports a role of the classical Frizzled-based PCP pathway in cell polarity in the germ-band (Warrington et al., 2013). However, whether the Toll- and Frizzled-based PCP pathways cooperate in generating the planar polarity of germ-band cells remains to be explored (Tepass, 2014). Besides the planar polarity, the epithelial cells have an elaborated apical-basal polarity. All studies, so far relied on observations of cross-sectional areas and actomyosin distributions at the apical and the subapical level defined by the adherens junctions. The significant third dimension of the epithelium has been neglected, so far. Important factors such as volume conservation and a potential contribution of the basal epithelial compartment need to be considered in future studies.

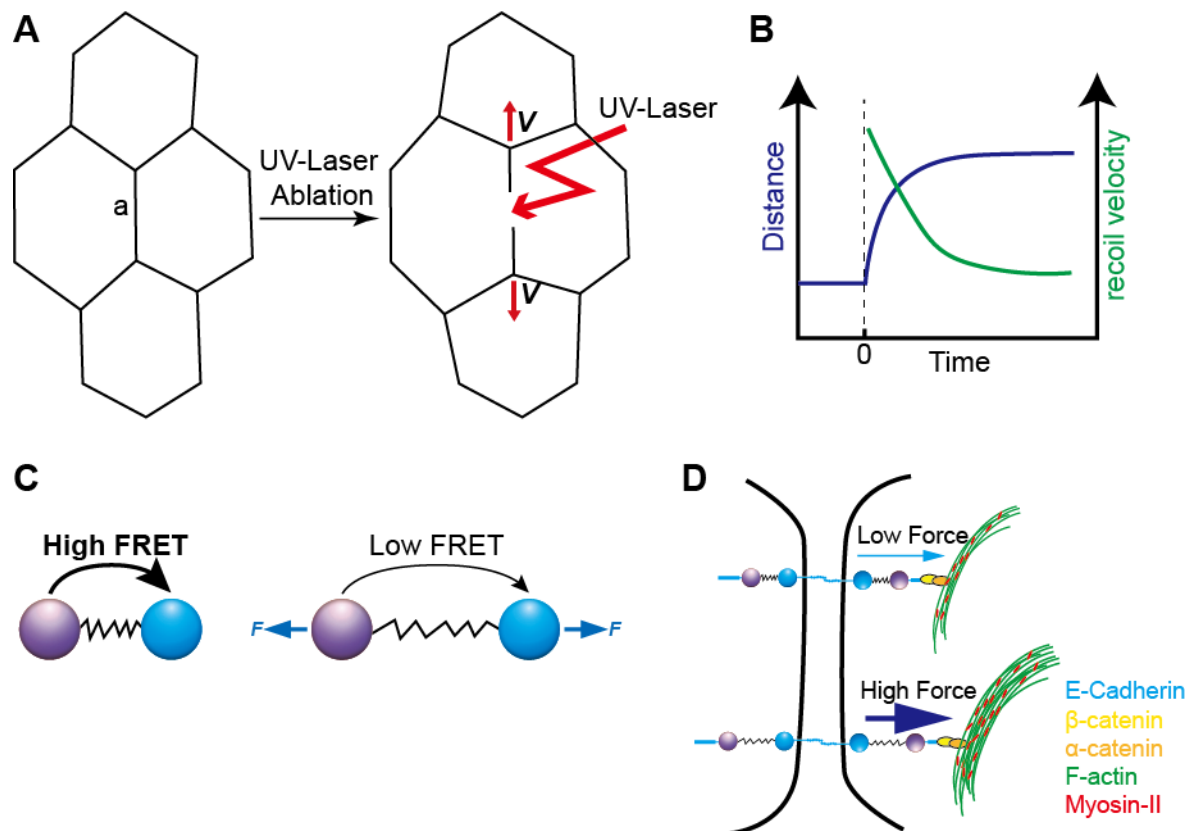


Figure 1.5 Methods for mechanical forces measurement *in vivo*.

(A) UV-laser ablation. The 3x vertices are under forces within a cell quadruplet. The ablation of a cell junction releases the tension and leads the system out of equilibrium. Immediately after laser ablation, the two 3x vertices move far away with a velocity (the direction of movement is indicated by red arrows). (B) The recoil velocity is proportional to the degree of initial tension under the ablated cell junction, although it does not provide an absolute measurement of the tension. The recoil velocity decays over time, which is due to the viscoelastic

properties of cells. (C) FRET-based tension sensor modules with elastic linker elements that extend in response to force (F , indicated by blue arrows) (Cost et al., 2015). (D) FRET-based E-Cad tension sensor (Cai et al., 2014).

So far, most studies focused on autonomous processes controlling cell intercalation. Given the advances in whole-embryo imaging (Tomer et al., 2012), it will soon be possible to relate the speed and timing of T1 processes to the position within the lateral epidermis and to the position relative to other T1 processes. Furthermore, better imaging combined with automated segmentation and computational analysis will generate data sets that are large and suitable for sophisticated statistical analysis. Automated segmentation and selection of cells according to computer-defined rules will remove any subjective bias introduced by the person conducting the analysis. The stochastic nature of cell behavior and associated T1 processes has not been investigated, so far. It will be important to include stochastic components in the analysis and modeling using the variance in addition to the mean behavior as an informative parameter. Such approaches will reveal non-autonomous and coordination mechanisms of cell behavior. It is obvious from time-lapse recordings that the cells of the lateral epidermis undergo T1 transitions within a certain time frame but importantly not simultaneously. Processes and (mechano-) signaling pathways that coordinate the individual T1 processes within the tissue need to be identified.

The role of mechanical forces and tensile stress at the cellular as well as tissue level has been addressed in several studies (Figure 1.3B, Figure 1.4). As the assays rely on invasive manipulations, such as laser cutting (Figure 1.5 A, B), inference methods for forces such as video force microscopy (Brodland et al., 2010) or non-invasive probes such as FRET based force sensors (Grashoff et al., 2010) need to be further developed (Figure 1.5 C). It is not clear how the forces are transmitted from cell to cell, but the E-Cad based adherens junctions are prime candidates (Hoffman and Yap, 2015). Equally important as E-Cad itself are the associated proteins, which link the transmembrane complexes to the cytoskeleton and importantly may be involved in sensing the local forces by force dependent conformation change (Cai et al., 2014)

(Figure 1.5 D). Identification of physiological forces sensors will be important because they are keys to understand the dynamic response of cells to the behavior of their neighbors.

1.10 Aim of the work

The aim of this work was to investigate the driving force of new cell junction formation in T1 process during *Drosophila* germ-band extension. (1) Why is the germ-band extension affected in *xit* mutants? How does the hypo-N-glycosylation affect the functions of E-Cad? (2) Whether the local cell contractions in A and P cells are sufficient to drive the DV cell junction formation in T1 process?

CHAPTER 2. Materials and Methods

2.1 Materials

2.1.1 Oligonucleotides used in the study

All oligonucleotides used in this study were ordered from Eurofins Genomics.

Table 2.1 Oligonucleotides used in the study.

Oligo No.	Sequence 5'→ 3'	Description
DK01	CGGGAATTGGGAATTCCGAACTGGATGT ACTGCC	Forward primer for InFusion cloning of <i>xiantuan(xit)</i> into pAttB with EcoR I
DK02	CCTCGAGCCGCGGCCGCACCTTAGACGC CGGTGGTG	Reverse primer for InFusion cloning of <i>xit</i> into pAttB with Not I
DK03	AGGATGGCAGTACATCCAG	<i>xit</i> sequence primer
DK04	CCATCTTTATGGGCGTCACT	<i>xit</i> sequence primer
DK05	TGGGGCCTACTATCTGTACG	<i>xit</i> sequence primer
DK06	TTGGATTTCACTGGAAGTAG	<i>xit</i> sequence primer
DK07	GACACCAAAGTGGCCATG	<i>xit</i> sequence primer
YZ20	CACAATCGACAATCGCATTC	<i>xit</i> sequence primer
YZ21	CATACTGCTCCTGAGCATC	<i>xit</i> sequence primer
YZ22	GAAGGAATCCTACTAACAGG	<i>xit</i> sequence primer
YZ23	TCCGATCGGCACAATGGAC	<i>xit</i> sequence primer
dsRNA oligoes containing the T7 promoter sequence at the 5' (shown in <i>italics</i>) (The oligoes are shown in pairs, as used for the respective gene.)		
YZ90	<i>TAATACGACTCACTATAGGGCTCGAGCTG</i> TGACCGCCG	<i>shotgun</i>
YZ91	<i>TAATACGACTCACTATAGGGGGTTCCAT</i> CGTTCTGGTGAATC	<i>shotgun</i>

CHAPTER 2

DK35	<i>TAATACGACTCACTATAGGGCTCGAGCTG</i> TGACCGCCG	<i>even skipped</i>
DK36	<i>TAATACGACTCACTATAGGGTTTGTACAA</i> TCTTTGGGG	<i>even skipped</i>
YZ96	<i>TAATACGACTCACTATAGGGTCTAGTGTA</i> TGTGCTCGGCG	<i>xit</i>
YZ97	<i>TAATACGACTCACTATAGGGTGTACCTTC</i> AAAACCTCCGGC	<i>xit</i>
YZ98	<i>TAATACGACTCACTATAGGGACGGATCTA</i> GTGTATGTGCTCG	<i>xit</i>
YZ99	<i>TAATACGACTCACTATAGGGAAAGAGCT</i> TCACCAAATGGG	<i>xit</i>

2.1.2 Antibodies

Table 2.2 Primary antibodies used in the study.

Antibody	Raised in	Dilution and working concentration		Source
		Staining	Western	
α -Catenin (DCAT-1)	Rat	1:2000	1:2000	Hybridoma bank (Oda et al., 1993)
α -Tubulin	Mouse	-	1:50000 (0.7 μ g/ml)	Hybridoma bank B512
Armadillo	Mouse	1:50 (1 μ g/ml)	-	Hybridoma bank (Riggleman et al., 1990)
Armadillo	Rabbit	-	1:1000	A. Mueller / Kassel
Bazooka	Rabbit	1:1000	-	A. Wodarz / Cologne (Wodarz et al., 1999)
Diaphanous	Guinea pig	-	1:5000	(Großhans et al., 2005)
Dlg	Mouse	1:100 (0.4 μ g/ml)	-	Hybridoma bank (Parnas et al., 2001)
E-Cadherin (DCAD1)	Rat	-	1:100	T. Uemura (Oda et al., 1993)

CHAPTER 2

E-Cadherin (DCAD2)	Rat	1:50 (7 µg/ml)	-	Hybridoma bank (Oda et al., 1993)
Engrailed	Mouse	1:10 (4.7 µg/ml)	-	Hybridoma bank (Patel et al., 1989)
Even-skipped	Guinea pig	1:1000	-	(Sung et al., 2013)
Slam	Rabbit	1:5000		J. Grosshans
Xit	Guinea pig	1:2000	-	Y. Zhang J. Grosshans lab

Secondary Alexa-conjugated antibodies were purchased from Life Technologies (Carlsbad, USA) and used at a final concentration of 1:500 (4 µg/ml). DNA staining was performed with DAPI (Sigma-Aldrich, St. Louis, USA) at a working concentration of 0.2 mg/ml. GFP-Booster-Atto488 was purchased from Chromotek (Martinsried, Germany) and used at a final concentration of 2 µg/ml. Secondary antibodies for western blots, IRDye-800CW and IRDye-680, were purchased from LI-COR Biotechnology (Bad Homburg, Germany) and used at a dilution of 1:20000 (0.05 µg/ml).

2.1.3 Fly stocks

Table 2.3 Fly stocks used in the study.

Name	Genotype	Source
117-GFP	w; GFP-resille; +/+; +/+	(Blankenship et al., 2006b)
<i>dia</i> , <i>mat67</i>	w; <i>dia</i> [SY5] <i>Frt</i> [2L] {neo}, <i>tub</i> -Gal4-VP16[67] {w+}; +/+; +/+	J. Grosshans
<i>Dia</i> SY5, E-Cad-GFP(k-in)	w; <i>dia</i> [SY5] <i>Frt</i> [2L] {neoR} DE-Cadherin-GFP[k-in] / <i>CyO</i> ; +/+; +/+	J. Grosshans
E-Cad-GFP (K-in)	w; DE-Cadherin-GFP[k-in]; +/+; +/+	(Huang et al., 2009)

CHAPTER 2

Mat 67, 15	w; tub-Gal4-VP16{w+} [67]; tub-Gal4-VP16{w+} [15]; +/+	St. Johnston / Cambridge
E-Cad-GFP, Sqh-mCherry	w; ubi-DE-Cadherin-GFP {w+}; sqhp-Sqh-mCherry {w+}; +/+	(Martin et al., 2009; Oda and Tsukita, 2001)
<i>gny</i> ^[f04215]	w; gny [f04215] FRT Frt2L [40A] / Cyo; +/+; +/+	(Shaik et al., 2011)
L285	w; P [w+, FRT] G13 shg(2IH) bw (1) sp (1) / Cyo; +/+; +/+	S. Luschign / Münster
L286	w; P [w+, FRT] G13 shg(1=IG29) bw (1) sp (1) / Cyo, ftz-lacZ; +/+; +/+	S. Luschign / Münster
OrR	+/+	-
Ovo 2L	y w hs-Flp [122]; ovoD Frt2L [40A] / Cyo, hs-hid {w+}; +/+; +/+	S. Luschign / Münster
Ovo 2R	y w hs-Flp [122]; ovoD Frt2R [G13] / Cyo, hs-hid {w+}; +/+; +/+	S. Luschign / Münster
Ovo18	ovo[D2] v [24] FrtX [9-2] {w+} / C (1) D X, y, w, f; +/+; +/+; +/+	J. Grosshans
Ovo18; mat67	ovo[D2] v [24] FrtX [9-2] {w+} / C (1) DX, y, w, f; tub-Gal4-VP16[67] {w+} / Cyo; +/+; +/+	J. Grosshans
PhiX86Fb	P{ry[+t7.2]=hsp70-flp} 1, y[1] w[*]; +/+; M{3xP3-RFP.attP}ZH-86Fb; M{vas-int.B}ZH-102D; +/+	Bloom. 23648 (Bischof et al., 2007)
E-cad-mCherry	w; UASp-ECad-Cherry {w+} / CyO; +/+; +/+	T. Kanasaki / J. Grosshans lab
GFP-Spider	w; GFP95-1 (GFP-Spider) {w+}; +/+; +/+	(Blankenship et al., 2006b)
GCaMP6m	w [1118]; +/+; UASp-GCaMP6-myr; +/+	(Chen et al., 2013)
<i>wol</i> ^[2]	w; wol ^[2] FRT Frt2L [40A] / Cyo; +/+; +/+	(Haecker et al., 2008)

<i>wol,gny</i>	w; wol ^[2] Alg 6 ^[P] FRT Frt2L [40A] / Cyo, Kr-GFP {w+}; +/+; +/+	S. Luschnig / Münster
<i>xit</i>	w xit[X-330] f Frt [9-2, 18E] Flp122{ry+} /FM7c, y w[a] sn B; +/+; +/+; +/+	A screen of germline clones (Vogt et al., 2006)
<i>xit</i> ; E-Cad- mCherry	w xit[X-330] f Frt [9-2, 18E] Flp122{ry+} /FM7c, y w[a] sn B; UASp-ECad-Cherry {w+} / CyO; +/+; +/+	Y. Zhang / J. Grosshans lab

Table 2.4 Fly stocks generated in the study.

Name	Genotype
4XGFP	w; GFP-Resille (117GFP) {w+}; GFP95-1(GFP-Spider) {w+}; +/+
<i>xit</i> ; 4XGFP	w xit[X-330] f Frt [9-2, 18E] Flp122{ry+} /FM7c; GFP-Resille (117GFP); Spider-GFP; +/+
Ovo; 117GFP	ovo[D2] v [24] FrtX [9-2] {w+} / C (1) DX, y, w, f; GFP-Resille (117GFP); +/+; +/+
<i>xit</i> ; E-Cad-GFP	w xit[X-330] f Frt [9-2, 18E] Flp122{ry+} /FM7c; DE-cadherin-GFP[k-in]; +/+; +/+
Ovo18; E-Cad-GFP	ovo[D2] v [24] FrtX [9-2] {w+} / C (1) DX, y, w, f; DE-cadherin-GFP[k-in]; +/+; +/+
<i>xit</i> rescue	w xit [X330] f Frt [9-2, 18E] Flp122{ry+}; +/+; xit[att86Fab] {w+} ; +/+

2.1.4 Microscopy

Spinning Disk microscope: Zeiss Observer.Z1, CSU-X1 (Carl Zeiss, Jena, Germany, 2009)

Cameras: AxioCam MRm
AxioCam ICc1
emCCD evolve 512

Optics: Epifluorescence, DIC

Lasers: 488nm (20mW, OPSP)
561nm (20mW, DPSS)

Objectives:	A. Plan (10x, NA 0.25) Plan-Apochromat (25x, NA 0.5, multi-immersion, DIC) Plan-Neofluar (40x, NA 1.3, oil, DIC) LCIPlan-Neofluar (63x, NA 1.3, multi-immersion, DIC) Plan-Apochromat (100x, NA 1.4, oil)
Laser ablation system:	UGA-42 (Rapp OptoElectronic, Wedel, Germany)
Lasers:	DPSSL-355/14: 355 nm pulsed YAG laser, 14 mW average power, 70 μ J per pulse, Up to 200Hz
Filter:	TB355/405/473
Confocal microscope	Zeiss AxioObserver.Z1 (Carl Zeiss, Jena, Germany, 2011)
LSM780:	
Detection:	PMT GASP cooled PMT
Lasers:	Diodelaser (405nm, 30mW) Argonlaser (458nm, 488nm, 514nm, 25mW) DPSS-Laser (561nm, 20mW) HeNe-Laser (633nm, 5mW)
Objectives:	EC Plan-Neofluar (10x, NA 0.3) LCI Plan-Neofluar (25x, NA 0.8, multi-immersion, DIC) C-Apochromat (40x, NA 1.2, water) Plan-Apochromat (63x, NA 1.4, oil) LCI Plan-Neofluar (63x, NA 1.3, multi-immersion)

Microinjection microscopes:

Leica MZ125	(Leica, Wetzlar, Germany)
Microinjection microscope	(Carl Zeiss, Jena, Germany)
Micromanipulator	(Eppendorf, Wesseling-Berzdorf, Germany)
Manual Micromanipulator	(Märzhäuser Wetzlar, Wetzlar, Germany)

Stereomicroscopes:

Zeiss Stemi 2000	(Carl Zeiss, Jena, Germany)
------------------	-----------------------------

2.1.5 Software

Zen 2012	(Carl Zeiss, Jena, Germany)
Image J	(NIH, Bethesda, USA)
Fiji	(Schindelin et al., 2012)
REO-SysCon-Zen	(Rapp OptoElectronic, Wedel, Germany)
Illustrator CS6	(Adobe, San Jose, USA)
Photoshop CS6	(Adobe, San Jose, USA)
Office 2011	(Microsoft, Redmond, USA)

2.2 Molecular biology methods

All the standard molecular cloning procedures were carried out as described in the manufacturer's protocol or in "Molecular Cloning: A Laboratory Manual" (Sambrook and Russell, 2001) unless otherwise stated.

2.2.1 Isolation genomic DNA from the adult flies

About 200 flies were anesthetized on the ice. The anesthetized flies were transferred to a mortar with liquid nitrogen and grinded with a pistle to a homogenous powder. The powder was transferred to a cooled Dounce homogenizer containing 5 ml of homogenization buffer (10 mM Tris/HCl [pH7.5], 60 mM NaCl, 10 mM EDTA), and

was grinded with a few strokes of the pestle to release cells and nuclei from the flies. The homogenate was transferred to a 15 ml centrifuge tube and was centrifuged to remove debris at 1000 rpm for 1 min. The supernatant was transferred to a new centrifuge tube and was centrifuged for 5 min at 8000 rpm. The supernatant was discarded and the pellet was resuspended in 0.5 ml homogenization buffer. The suspension was transferred to a 2 ml tube, and proteinase K (10mg/ml) was added to a final concentration of 100µg/ml and mixed. 50 µl of 10% SDS was added and mixed by swirling and rocking. The sample was incubated at 37°C for 45 to 60 min.

0.5 ml phenol/chloroform was added and the tube was placed on a horizontal shaker for 5 min and then spun 3 min in the microfuge at 14,000 rpm. The upper part was transferred into a new Eppendorf tube. This step was repeated with 0.5 ml phenol-chloroform-IAA (50:49:1) instead of phenol/chloroform to remove protein further more. After centrifuge, the upper part was transferred to a new Eppendorf tube. 0.5 ml chloroform was added and mixed well. After centrifuge as before, the upper phase was transferred to a new Eppendorf tube. 3 M NaCl was added to the sample to a final concentration of 200 mM and mixed well. Two volumes of 100% ethanol were added into the tube and mixed by gentle swirling. The DNA appeared at the interface as a clump. After a white thread-like precipitate formed, the DNA was transferred by a glass hook to the tube with 80% ethanol. The precipitate was washed with 80% ethanol and then 100% ethanol. The sample was centrifuged for 5 min at 14,000 rpm and the ethanol was removed. The DNA was air-dried under the hood around 20 min to remove ethanol completely and dissolved in 500 µl TE buffer. The concentration was measured by Nano-drop.

2.2.2 Polymerase chain reaction (PCR)

The PCR was carried out using Taq or Pfu DNA polymerases which were generated in the lab. The following reagents were mixed for the standard PCR:

50-200 ng

plasmid or genomic DNA,

0.5 μ M	forward and reverse primers,
50 μ M	dNTP (each),
10X PCR buffer	(depending on the polymerase),
1-2 units (per 50 μ l of reaction)	Taq or Pfu polymerase.

The PCR was done using the following conditions for cloning:

Step 1 (Initial denaturation):	95°C	- 2 min
Step 2 (Denaturation):	95°C	- 30 sec
Step 3 (Annealing):	50-60°C	- 1 min
(depending on the annealing temperatures of the primers)		
Step 4 (Elongation):	72°C (Taq)	- 1 min/Kb to be amplified
Step 5 (Repetition of cycles):	Steps 2 to 4	- 30 cycles
Step 6 (Final elongation):	72°C (Taq)	- 10 min

The PCR was done using the following conditions for the DNA templates of in-vitro transcription:

Step 1 (Initial denaturation):	95°C	- 2 min
Step 2 (Denaturation):	95°C	- 30 sec
Step 3 (Annealing):	50-60°C	- 1 min

(depending on the annealing temperatures of the primers without the T7 promoter sequence)

Step 4 (Elongation):	72°C (Taq)	- 1 min/Kb to be amplified
Step 5 (Repetition of cycles):	Steps 2 to 4	- 5 cycles

Step 6 (Denaturation):	95°C	- 30 sec
Step 7 (Annealing):	60-70°C	- 1 min
(depending on the annealing temperatures of the whole primers)		
Step 8 (Elongation):	72°C (Taq)	- 1 min/Kb to be amplified
Step 9 (Repetition of cycles):	Steps 6 to 8	- 30 cycles
Step 10 (Final elongation):	72°C (Taq)	- 10 min

2.2.3 In-fusion cloning

In-fusion cloning was carried out according to the manufacturer's instructions.

2.2.4 DNA sequencing

DNA sequencing was carried out with the sequencing facility at the Department of Developmental Biochemistry, GZMB, University of Goettingen, or Seq-Lab, Goettingen.

2.2.5 *In-vitro* transcription

Double-stranded RNA (dsRNA) for RNAi was carried out by *in-vitro* transcription of a PCR generated template containing the T7 promoter sequence on both ends. After gel extraction, the DNA templates were eluted in nuclease-free water with a final concentration 0.5 µg/µl.

dsRNA synthesis was performed using the following reagents in 50 µl final volume in nuclease-free water:

4 µl (2 µg)	DNA templates
5 µl	10X Transcription Buffer (for T7 pol) Roche/Fermentas
3.75 µl	100 mM CTP

3.75 μ l 100 mM ATP

3.75 μ l 100 mM UTP

3.75 μ l 100 mM GTP

with a final concentration of 7.5 mM NTPs

1.25 μ l RNAase inhibitor (final concentration 1U/ μ l) Roche

2.5 μ l Pyrophosphatase

2.0 μ l RNA pol

20.25 μ l nuclease-free water

The reaction was incubated at 37°C for 4 hours. 1 μ l RNA polymerase was added to the reaction and mixed well. The reaction was incubated at 37°C for another 2 hours. 3 μ l DNaseI was added into the reaction and the reaction was incubated for 15 min at 37°C to remove the DNA templates completely. Nuclease-free water was added into the reaction to 100 μ l. 100 μ l phenol-chloroform-IAA (25:24:1) was added to the same tube. The sample was mixed well and centrifuged for 5 min at 14,000 rpm. The upper phase (~100 μ l) was transferred to a new tube and 100 μ l chloroform was added, mixed well and centrifuged for 5 min at 14,000 rpm. The upper phase (~100 μ l) was transferred to a new tube, 10 μ l 3M NaAc (dissolved in nuclease-free water) and 2.5 fold 100% Ethanol were added into the sample, and mixed well. The sample was incubated at -20°C overnight or -80°C for 1 hour to precipitate the dsRNA. The sample was centrifuged 30 min on 4°C at 14,000 rpm. The pellet was washed with cold 70% ethanol and air-dried. The pellet was dissolved in 20 μ l nuclease-free water. The dsRNA for injection was stored with 2 μ l aliquot at -80°C.

2.3 Genetic methods

2.3.1 Generation of *xiantuan (xit)* genomic transgene fly

For the *xit* genomic transgene, DNA of the *xit* locus (nt 6713852..6717073, annotation according to FlyBase, which contains 1 kb of upstream and 200 bp of

downstream of the gene region) was amplified by PCR and cloned into the EcoRI-NotI sites of pattB vector by in-fusion cloning (Bischof et al., 2007). The embryos of attP-zh86Fb/nos- ϕ -zh102D were used for injection and the *xit* genomic transgene was inserted into the 86F region (ZH102D) by phiC31 mediated transgenesis.

2.3.2 Generation of germline clones

The germline clones were created following the instruction by Chou and Perrimon (Chou and Perrimon, 1992) with minor modifications. The heat shock for inducing flippase was performed at 37°C for 60 min per day for two days (24-48 hour and 48-72 hour) after hatching.

2.3.3 UAS-GAL4 system

The UAS-GAL4 system is used to ectopically overexpress the gene of interest in a time and tissue specific manner (Brand and Perrimon, 1993). A yeast transcription factor GAL4 that binds to an upstream activating sequence (UAS), thereby activates the target gene expression. In UAS reporter flies the target gene is placed under the control of UAS. A GAL4 driver line contains the GAL4 gene under the control of a promoter or enhancer of a gene with a known expression pattern. The target genes are expressed by crossing with GAL4 driver lines.

2.4 E-Cadherin RNAi treatment of *Drosophila* embryos

0-30 min embryos were collected and dechorionated, dried in a desiccation chamber for ~8 min, covered with halocarbon oil and injected dorsally with dsRNA ($c = 3.5 \mu\text{g}/\mu\text{l}$). After injection, the embryos were aged in a wet chamber for 2 hours at 25°C. After that, imaging was carried out. For immunostaining and western blot, embryos were injected posteriorly with dsRNA ($c = 6.7 \mu\text{g}/\mu\text{l}$) and aged for 2.5 hours at 25°C in a wet chamber.

2.5 RNAi treatment and immunostaining of *Drosophila* cells

Drosophila (S2) cells were seeded on 0.1% Poly-L-lysine coated glass coverslips. RNAi treatment was performed as previously described (Worby et al., 2001). After 3 days of RNAi treatment, the cells were collected for immunostaining. The medium was removed from the cells, and the cells were washed with PBS for a few seconds twice. They were fixed with 3.7% Formaldehyde in PBS for 20 minutes, permeabilized with 0.5% TritonX-100 in PBS for 5 min, blocked with 5% BSA in 0.1% PBST for 60 minutes; the cell sample was ready for immunostaining. The cell sample was incubated with primary antibody in 1% BSA in PBS for 2 hours at room temperature. The sample was washed with PBT 3 times gently and incubated with secondary antibody for 1.5 hours at room temperature. The sample was washed with PBT 3 times gently and incubated with DAPI for 5 minutes. The sample was washed with PBT 2 times gently and mounted with Aquapolymount (Polyscience). The sample was polymerized for overnight at 4 °C.

2.6 Fixation of *Drosophila* embryos

2.5-5 hours (25°C) or 3.5-6 hours (22°C) embryos were collected, dechorionated in 50% Klorix bleach for 90 seconds. The embryos were transferred into a scintillation vial with 4% formaldehyde in PBS and heptane, fixed for 20 min with constant shaking. Formaldehyde was removed and embryos were washed with PBS for 3 times. The vitelline membrane was removed by shaking in heptane and methanol. For phalloidin staining, embryos were fixed with 8% formaldehyde for 40 min. The vitelline membrane was removed manually. For Arm, Baz, En, and Eve staining, embryos were fixed in 0.4% NaCl, 0.03% Triton X-100 by heating treatment and the vitelline membrane was removed by shaking in heptane and methanol. Embryos after injection were washed into a scintillation vial by heptane and fixed with 8% formaldehyde for 40 min, removed the vitelline membrane manually. For the images of AS cells, 0-2 hour embryos were collected at 25°C, aged for 15 hours at 22°C to yield populations of dorsal closure staged embryos and fixed as before.

For the imaging of GFP without staining, embryos were fixed with 8% formaldehyde for 40 min. The vitelline membrane was removed manually. The embryos were mounted in Aquapolymount (Polyscience).

2.7 Immunostaining of *Drosophila* embryos

The embryos stored in methanol were rinsed 3 times and washed for 15 min in PBT. Blocking was carried out for 1 hour in 1 ml of 5% BSA in PBT. The primary antibodies were added in the respective dilutions in 0.5% BSA in PBT and embryos were incubated at room temperature for 2 hours or at 4°C overnight with constant rotation. Embryos were then rinsed 3 times in PBT and given four 15 min washes. Appropriate secondary antibodies, GFP-booster or phalloidin were added in PBT and incubated for 1.5 hours at room temperature. Embryos were again rinsed 3 times in PBT and given three 15 min washes. Embryos were stained with DAPI for 5 min, rinsed thrice with PBT, washed for 15 min with PBT and were mounted in Aquapolymount (Polyscience).

For E-cadherin staining, embryos were blocking in with 5% (w/v) milk powder in PBT for 1 hour at room temperature. The primary antibody was dilutions in 0.5% BSA in PBT and embryos were incubated at room temperature for 2 hours (not any longer). The following steps were same with others.

Fluorescent images were recorded with a confocal microscope (Zeiss LSM780) with a Zeiss X63, N.A. 1.3, and water-immersion objective. Images were processed with ImageJ/Fiji and Photoshop (Adobe).

2.8 larval cuticles preparation

An overnight egg laying collection was taken and aged for another 24 hours to allow completion of embryonic development. The embryos were transferred into a net where they were washed, dechorionated and washed with water. Dechorionated embryos were transferred with a fine brush to a drop of the mixture of Hoyer's medium (Hoyer, 1882) and lactic acid on a clean slide. The embryos were pushed into the medium and covered

with a clean cover slide and incubated for overnight at 65°C. A piece of metal was added to press the specimen. Images were taken with dark field optic or phase contrast.

2.9 Western blot

3-6 hours (25°C) or 3-7 hours (22°C) embryos were collected and dechorionated. The dechorionated embryos were transferred into an Eppendorf tube. The weight of the embryos was determined (~1mg =100 embryos). A number of embryos was counted manually when the embryos were too less. The embryos were snap-frozen with liquid nitrogen. 1X Lämmlli buffer was added and the embryos were homogenized. The sample was then heated to 95°C or 65°C (for E-cadherin) for 10 min and centrifuged at 14,000 rpm for 10 min. The embryos were either loaded immediately on an SDS-gel for a western blot or stored in -20°C for future use. For the embryos after injected, the embryos were washed from cover slips with heptane into a scintillation vial. Embryos were washed by heptane and PBS for several times respectively and transferred into an Eppendorf tube. The embryos were counted manually and homogenized with 1X Lämmlli buffer.

20 embryos were loaded on an SDS-PAGE gel (6% for E-cadherin Western blot, 8% for other proteins Western blot). The gel was run at 13 mA constant current for the stacking gel and 16 mA constant current for the separating gel. The proteins from the gel were transferred onto a nitrocellulose membrane either using a semi-dry transfer for 1 hour (Westerns for Arm and alpha-catenin) or wet transfer for overnight (Westerns for E-cadherin). The membrane was then blocked in 5% (w/v) milk powder in PBT for 1 hour and incubated with primary antibody 2 hours at room temperature. The membrane was rinsed 3 times in PBT and given four 15 minute-PBT washes. The blot was incubated with fluorescently labeled secondary antibodies (LI-COR, 1:20000, and 0.05 mg/ml) for 1.5 hours at room temperature. Then it was again rinsed 3 times in PBT and given four 15 minute-PBT washes, after which the bands were recorded with an 'Odyssey CLx Imaging System' (LI-COR) at 16-bit color depth. Western blots for Arm

and alpha-Catenin were developed by chemiluminescence with peroxidase linked to the secondary antibody. For all the E-cadherin Westerns, the membranes were stripped by stripping buffer (50 mM Tris/HCl pH [6.7], 2% SDS, 0.5% beta-mercaptoethanol) for 45 min at 50°C and redeveloped with Diaphanous (Dia) primary antibody that served as a loading control. For quantification, integrated signals of E-Cadherin were normalized by corresponding Dia signals.

2.10 Glycan cleavage with glycosidases

The embryos were collected as mentioned in 2.9. Dechorionated embryos were lysed in lysis buffer (50 mM Hepes-NaOH pH [7.5], 150 mM NaCl, 1% Triton X-100, 10% (v/v) glycerol, 1.5 mM MgCl₂, 2 mM EGTA, 1mM phenylmethylsulfonyl fluoride, 10 mg/ml aprotinin) for 10 minutes on ice with a concentration around 9 embryos in 1 µl lysis buffer. The embryos lysis was centrifuged for 15 minutes at 14,000 rpm at 4°C. Following centrifugation 9 µl of the supernatant were denatured with 1 µl of 10X denaturing buffer (5% SDS, 0.4 M DTT) for 10 minutes at 60°C. After addition of 2 µl 10X reaction buffer (50mM Na-phosphate pH [7.5]) 2 µl NP40 (10%), 2 µl N-glycosidase F (New England Biolabs, (T H Plummer and Tarentino, 1991)) and water to 20 µl, N-glycans were cleaved for 3 hours at 37°C. High mannose N-glycans were cleaved by endoglycosidase H (New England Biolabs, (Maley et al., 1989)) treatment for 1 hour at 37°C. 10X reaction buffer was 0.5 M Na-citrate pH [5.5]. No NP40 was added to the reaction mix with endoglycosidase H. 20 µl 2X Lämmli buffer was added into the reaction and mixed well. The sample was heated to 65°C for 10 minutes for Western blot or stored in -20°C.

2.11 Ca²⁺ uncaging

Loaded NP-EGTA, AM (2mM, Invitrogen) were prepared in 1X injection solution (180 mM NaCl, 10 mM HEPES, 5 mM KCl, 1 mM MgCl₂, pH 7.2) (G. L. Hunter et al., 2014). Embryos (2-2.5 hours at 25°C) were collected for injection. Embryos were incubated at 25°C in dark about 10-20 min prior to uncaging. Ca²⁺ was released by a 355 nm pulsed YAG laser (DPSL-355/14, Rapp OptoElectronic) illumination under the

'Click and Fire' Mode, while a movie was recorded on a spinning disc microscope (Zeiss, X100 oil, N1.4). The intensity of the uncaging laser was adjusted so that no morphological changes were induced in 1X injection solution injected embryos. The laser was exposed 1500 milliseconds (around 300 pulses) per cell with 2.5% laser power (around 0.5 mJ/cell). For the images in Figure 4.3, after UV-laser illumination, the image stacks with 0.5 μm z-interval were recording by a spinning disc microscope (Zeiss, x100 oil, N 1.4) with an emCCD camera (Photometrics, Evolve 512).

The start point of the cell contraction after uncaging is depended on the size of illumination of UV-laser which can be adjusted by the number of spot-radius on the platform of 'REO-SysCon-Zen' (Rapp OptoElectronic). The onset of target cell contraction was controlled by adjusting the spot radius. For example, a target cell with a 6 μm diameter shows the obvious contraction in 1 minute after uncaging when the spot radius is 4. However, the target cell shows the obvious contraction in 3 minutes after uncaging when the spot radius is 1 (Figure 2.1).

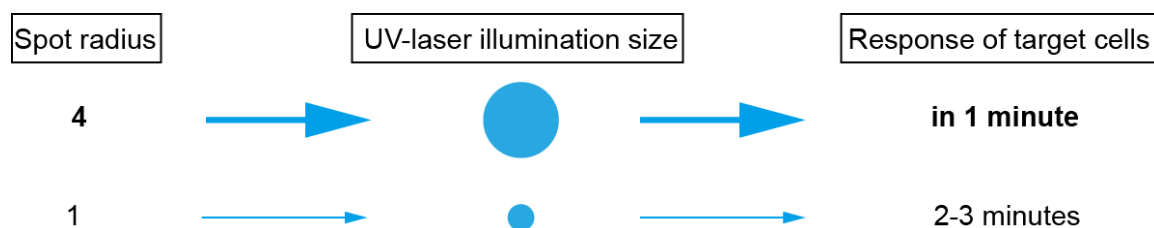


Figure 2.1 Schema of the response of target cells for different size of UV-laser illumination.

The UV-laser illumination size could be adjusted by spot radius value to control the response of target cells.

The image stacks were processed with ImageJ/Fiji. (Z-projected) Time-lapse images were segmented with Tissue Analyzer (Aigouy et al., 2016), cell area measurements were carried out with ImageJ. The fluorescence intensity was measured with ImageJ manually.

2.12 Live-imaging of *Drosophila* embryos

Dechorionated embryos were aligned on an agar block, glued on to a coverslip and covered with halocarbon oil. Time-lapse image stacks (3 z-stacks with 1 μm interval) of

E-cadherin-GFP were recorded with a confocal microscope (Zeiss LSM780) with a Zeiss X63, N.A. 1.3, and water-immersion objective every 10 seconds. Image stacks were z-projected with the 'max-intensity' mode with ImageJ/Fiji and processed with Photoshop (Adobe). All other fluorescent live-images were taken at the spinning disc microscope (Zeiss) with a Zeiss X63, N.A. 1.3, and water-immersion objective every 5 seconds at a single plane. Images were processed with ImageJ/Fiji, segmented with Ilastik /EDGE (Gelbart et al., 2012; Sommer et al., 2011) and the cell area measurements were carried out with EDGE (Gelbart et al., 2012).

2.13 Laser ablation

The embryos of E-Cadherin-GFP and germ line clone of *xit*; E-Cadherin-GFP were collected for 2 hours with apple juice agar plates at 25°C, and aged for 15 hours at 22°C to yield populations of dorsal closure staged embryos, and dechorionated. The embryos were aligned on agar block and transferred to a cover slide and dried in a desiccation chamber for 2 min, covered with halocarbon oil. The UV laser (DPSL355/14, 355 nm, 70 µJ/pulse, Rapp Optoelectronic) was introduced from the epi-port of the microscope and was controlled by an independent scanning head (Rapp Optoelectronic). An ablation was carried out at the plane of adherence junction with the 10% of laser power, and the exposure time was 200 milliseconds (around 40 pulses) during recording mode on an inverted spinning disc microscope (Zeiss, x40 oil, N 1.3) with a CCD camera (Zeiss). After cutting, the images were recorded by a spinning disc microscope (Zeiss, x40 oil, N 1.3) with an emCCD camera (Photometrics, Evolve 512). The emCCD camera allowed that the image stacks were recorded every 10 seconds per frame. Imaging was started in 1 min after the ablation was done. The image stacks were processed with ImageJ/Fiji. Z-projected time-lapse images were segmented with Ilastik /EDGE and the cell area measurements were carried out with EDGE.

The laser ablation system is independent of imaging microscope, so an ablation was performed during imaging on an inverted spinning disc microscope. Laser ablation

experiments for the recoil velocity measurement was carried out at the plane of adherence junction while the images were recorded every 0.5 sec by spinning disc microscope (Zeiss, X100 oil, N1.4). Imaging was started around 1 minute prior to the ablation and finished around 2 minutes after the ablation. To measure the recoil velocity after the laser ablation, the distances of two nodes from target junctions were measured manually. Initial recoil velocity was measured using the first and second frame after cutting.

2.14 Fluorescence recovery after photobleaching (FRAP)

The FRAP experiment was carried out at the plane of adherence junction, while the images were recorded with a confocal microscope (Zeiss LSM780) with a Zeiss X63, N.A. 1.3, and water-immersion objective. Bleaching of E-Cadherin GFP was carried out in a single distinct E-cadherin GFP cluster using 100% laser power and 30 iterations at a scan speed of 5. After bleaching, the images were recorded for another 2 minutes with 2 seconds per frame. The bleaching region was tracked and the fluorescence intensity was measured in Fiji/Image J manually. The fluorescence intensity at each time point was normalized as follows:

$$\text{Normalized intensity: } I = (I_t - I_{min}) / (I_{max} - I_{min})$$

Where I_t is the intensity at time t , I_{min} is the intensity immediately post-bleach and I_{max} is the intensity pre-bleach.

CHAPTER 3. The glucosyltransferase Xiantuan is required for germ-band extension and the function of E-Cadherin in *Drosophila*

Parts of this section was conducted in collaboration with Dr. Yujun Zhang and built on her work. The analysis of AS cell oscillations in 3.8 was performed by Dr. Lars Reichl (Max Planck Institute for Dynamics and Self-organization).

3.1 *xiantuan* (*xit*) is required for gastrulation movements

xiantuan (*xit*) was previously identified in a collection of X-linked germline clone mutations with early embryonic phenotypes (Vogt et al., 2006). Embryos from females with germline clones of *xit*, called *xit* embryos in the following, develop normally until gastrulation. Morphogenetic movements were affected in *xit* embryos during gastrulation. All *xit* embryos, germ-band extension was incomplete, the cephalic furrow was not visible, and ventral furrow formation was affected (Figure 3.1) (Y. Zhang et al., 2014). This indicates that *xit* thereby has maternal functions at gastrulation of embryos. With incomplete germ-band extension, *xit* embryos developed further and passed through germ-band retraction and abnormal dorsal closure and formed abnormal cuticles, presumably due to the zygotic expressing of *xit*. All *xit* embryos failed to hatch. Using the cuticle as a criterion, two classes could be identified: (1) no/little cuticle, (2) while with segmentation defects (Figure 3.7C).

3.2 *xit* encodes a glucosyl-transferase in the endoplasmic reticulum

The mapping and sequencing of *xit* were carried out by Dr. Yunjun Zhang (Y. Zhang et al., 2014). Sequencing of the genomic region revealed a single point mutation in *xit* (CG4542) that leads to a premature stop codon at codon 403 (Figure 3.2). To prove that the mutation of the *xit* gene was responsible for the observed phenotypes, I generated a genomic rescue construct (Figure 3.2), which rescued the germline clone phenotype

and lethality completely (Figure 3.5). *xit* encodes a homolog of the *ALG8* gene in *Saccharomyces cerevisiae* (Stagljar et al., 1994a). *ALG8* catalyses the final steps in the biosynthesis of the N-glycan precursor together with *ALG5* and *ALG6* (Figure 3.3). *ALG8* transfers the second out of three glucose residues onto the dolichol glycan as the second but last step before the transfer of the mature glycan to asparagine residues of nascent polypeptide chains by oligosaccharyl transferase (*OST*) (Figure 3.3).

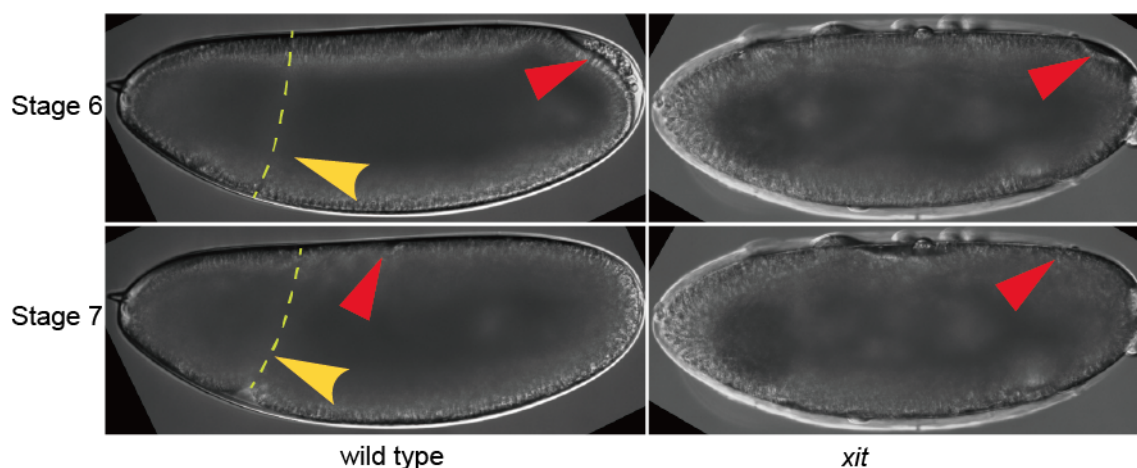


Figure 3.1 *xit* is required for germ-band extension.

Wide-field images from time-lapse recording at indicated stages and genotypes. *xit* indicates embryos from females with *xit* germline clones. Cephalic furrow is highlighted by yellow dash curve and indicated by yellow arrowheads in the images from wild type embryos. Red arrowheads indicate the position of the posterior midgut invagination.

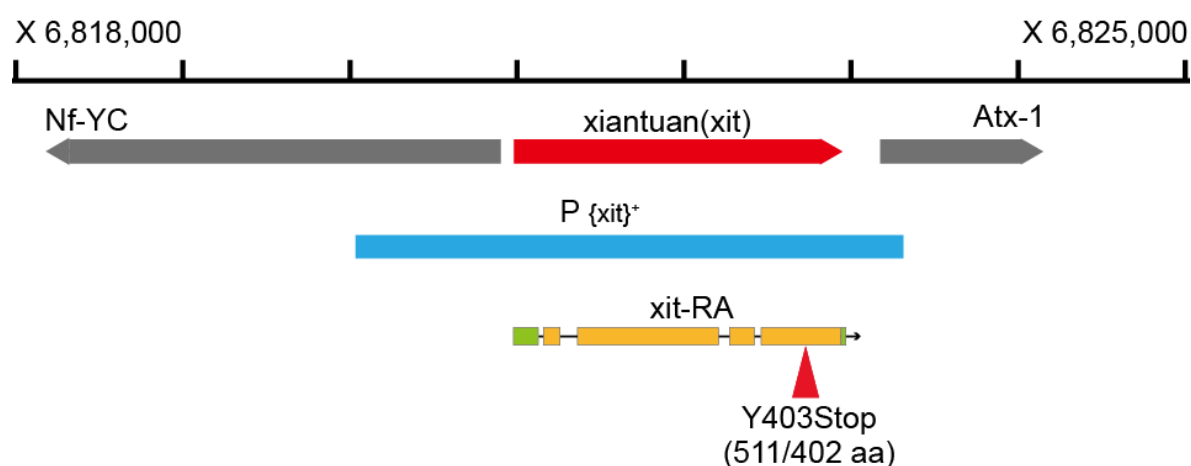


Figure 3.2 Schematic representation of genomic rescue of *xit* mutants.

Genomic region X: 6,818,000 to X: 6,825,000 are indicated. Genomic region of *xiantuan* (*xit*) is marked in red and neighboring genes are marked in grey. The genomic rescue construct $P \{xit\}^+$ covers the whole region of *xit* extending 1kb to upstream and 0.2 kb to downstream respectively (marked in blue). The transcript of *xit* is

shown in bottom, introns in black lines, exons in yellow boxes, and UTR in green boxes. The position of mutated codon is indicated with red arrowhead.

wol and *gny* have been reported previously as mutations in the *Drosophila* homologs of *ALG5* and *ALG6* in *Saccharomyces cerevisiae* respectively (Haecker et al., 2008; Shaik et al., 2011). Mutations in *wol* lead to posterior segmentation phenotypes, impaired mesoderm invagination and germ-band elongation at gastrulation (Haecker et al., 2008). By analysis the morphology, I found that the phenotypes of *wol*, *gny* and *wol gny* double mutants are comparable with the germ-band extension phenotype of *xit*, which thereby suggests that *wol* and *gny* have a comparable function (Figure 3.5, 3.7A, 3.9). Furthermore, as the *gny wol* double mutant phenotype is similar to *wol* and *gny* single mutant phenotypes (Figure 3.5, 3.7A), these genes have non-redundant functions in a single pathway in *Drosophila*. This is consistent with the genetics of *ALG5,6* and *8* in *Saccharomyces cerevisiae* (Figure 3.3).

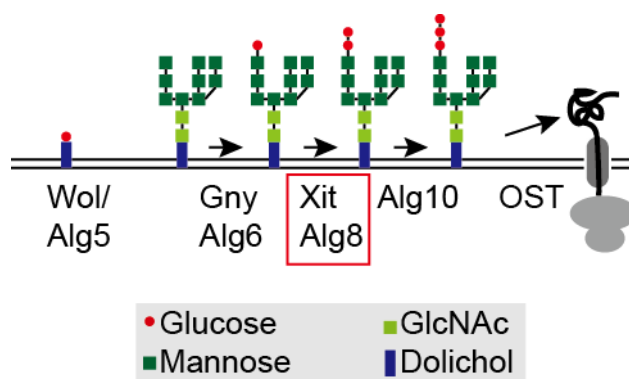


Figure 3.3 *xit* encodes a glucosyltransferase.

Scheme of the final steps in biosynthesis of the N-glycan precursor and transfer to nascent proteins in the endoplasmic reticulum. Wol provides activated glucose residues, Gny, Xit and Alg10 transfer glucose residues to the N-glycan precursor. OST transfers the mature N-glycan to nascent polypeptide chains. GlcNAc glucosamin-N-acetat. OST oligosaccharyl transferase.

An antibody against recombinant *xit* protein was generated by Dr. Yunjun Zhang. To assess whether the antibody is specific for *xit* protein staining. I stained cultured S2 cells, which were treated or not treated with *xit* specific RNAi (Figure 3.4 A). Perinuclear staining was obviously reduced by *xit* RNAi treatment. This is consistent with the assumed ER localization of Xit. Staining of fixed embryos, which was carried out by Dr.

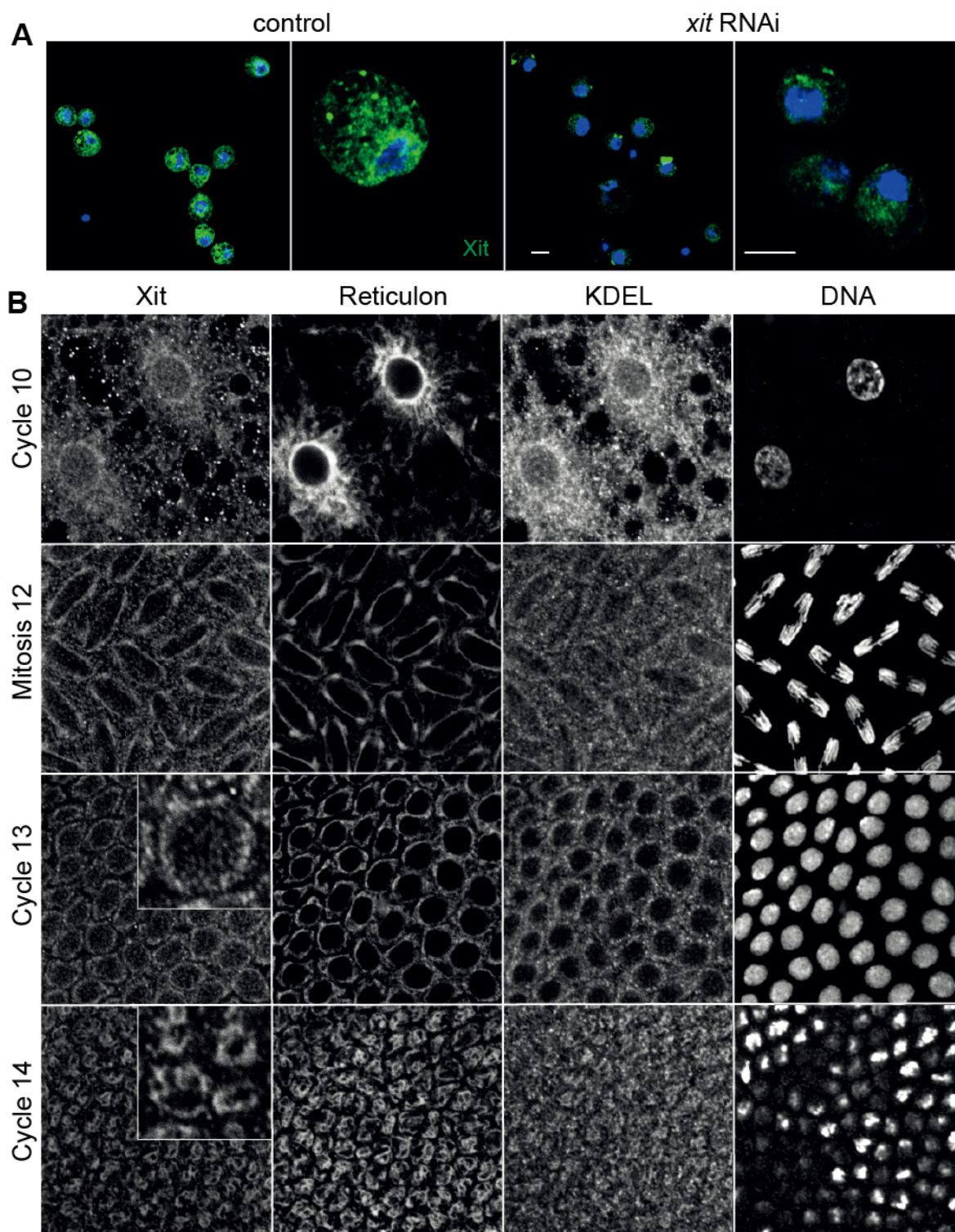


Figure 3.4 Xit colocalises with KDEL and reticulon.

(A) Cultured cells (S2R+) treated with *xit* RNAi for three days, were fixed and stained with Xit anti-serum (green) and DAPI for DNA (blue). Scale bars, 5 μ m. (B) Fixed wild type embryos stained for Xit, the ER markers reticulon and KDEL and DNA. Insets are at 3x higher magnification. Staging of the embryos as indicated by morphology and nuclear density. The embryo staining was carried out by Dr. Yujun Zhang.

Yujun Zhang, shows that the pattern of Xit staining largely overlaps with the patterns of ER proteins reticulon (Wakefield and Tear, 2006) and KDEL receptor (Figure 3.4 B). Altogether, these data are consistent with the assumed function of Xit in the ER.

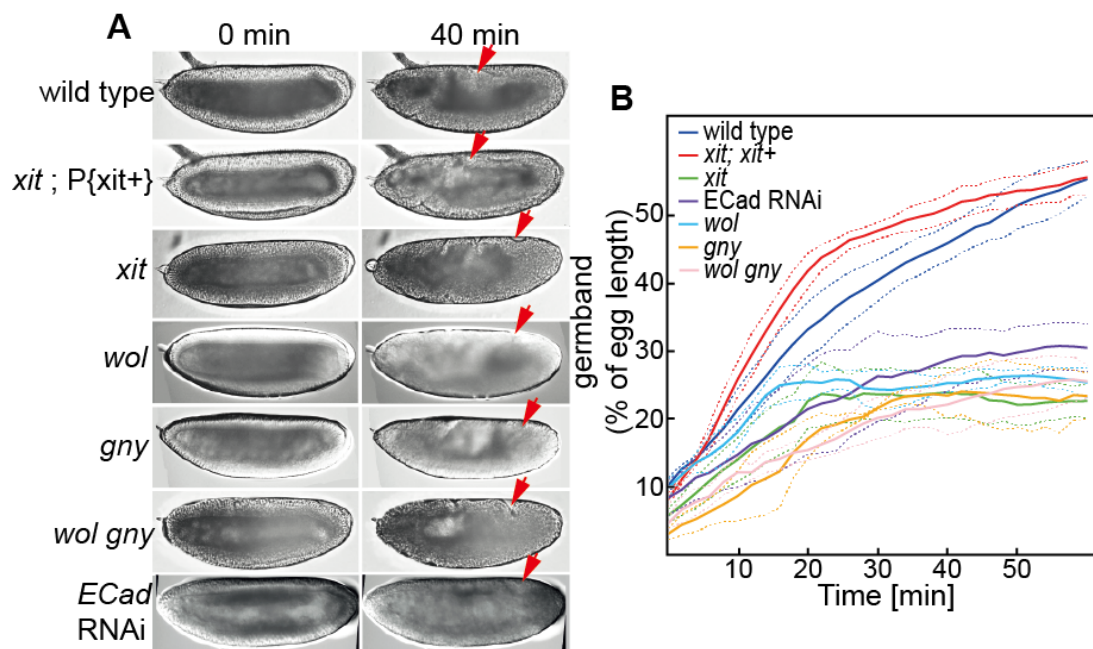


Figure 3.5 Xit and E-Cadherin are required for germ-band extension.

(A) Images from time-lapse recordings with wide-field optics at the onset of germ-band extension (0 min, stage 6) and after germ-band extension (40 min, stage 8/9). The genotype of females or germline clones is indicated. *xit*; P{*xit+*} are embryos from females with homozygous *xit* mutation on X chromosome and a *xit* genomic rescue transgene on the third chromosome. Arrows in red mark the extent of germ-band extension. (B) The time course for the distance between the position of the posterior midgut invagination and the posterior pole of the egg indicates the extent of germ-band extension. The distance was normalized with total egg length. Dashed lines indicate confidence intervals of the standard error of the mean. N = 5 (wild type, *xit*; P{*xit+*}), 4 (E-Cad RNAi, *wol*, *gny*, *xit*), 3 (*wol gny*) embryos.

3.3 *xit* is required for cell intercalation

Germ-band extension is largely based on polarised cell intercalation (Irvine and Wieschaus, 1994). I next focused on the germ-band extension phenotype of *xit*. I measured how far the germ-band extended over time by the time lapse recording with DIC optics (Figure 3.5). In wild type embryos, the posterior end of the germ-band extended to 50% of the embryo's length within 30 minutes. In contrast, the germ-band failed to extend much beyond the posterior pole in *xit* embryos. This defect is due to

impaired cell intercalation, as new cell junction formation is incomplete and delayed during the T1 process (Figure 3.6), which was characterized by Dr. Yunjun Zhang (Y. Zhang et al., 2014).

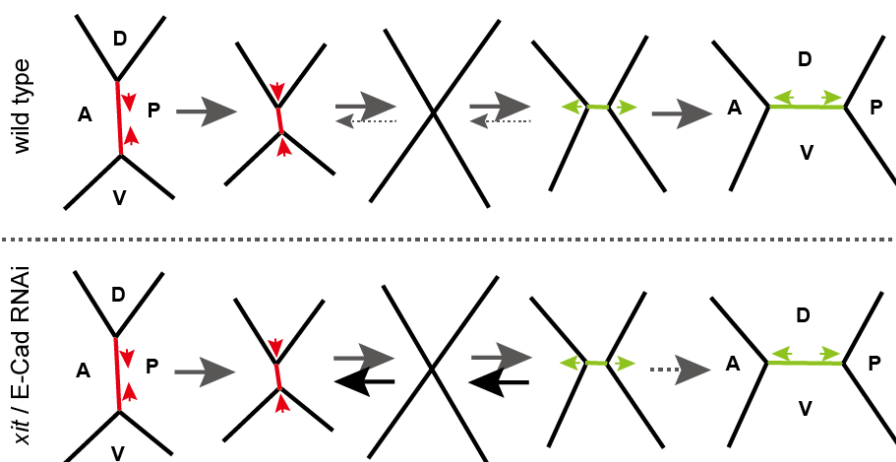


Figure 3.6 *Xit* and E-Cadherin are required for new junction formation during T1 transitions.

The key to neighbor exchanges in germ band is junction dynamics according to a topological T1 transitions. During T1 transitions, collapse of a junction with dorsal-ventral orientation (vertical) (red) forms a 4x vertex and a new junction (green) grows in perpendicular orientation subsequently. The new junction formation is blocked in the embryos which are from *xit* germline clone females or injected with E-Cad dsRNA. A, P, D and V indicate anterior, posterior, dorsal and ventral respectively.

As the anterior-posterior (AP) patterning genes are necessary for *Drosophila* germ-band extension (Figure 1.2) (Irvine and Wieschaus, 1994), I stained embryos with Even skipped and Engrailed to investigate the embryonic AP polarity of *xit* mutants. Seven stripes of Eve expression were observed both in wild type and *xit* mutant embryos at the onset of gastrulation (Figure 3.7A). In some *xit* embryos, the staining of posterior stripes was weaker. Similarly, a normal number of the stripes of Engrailed expression were observed in later *xit* embryos (stage 9, Figure 3.7B). The morphology of *xit* embryos is already abnormal at this stage, which did not allow me to analyse the expression pattern in detail. Differences in expression levels or/and timing of expression of Engrailed cannot be excluded completely. Consistent with the normal expression pattern of Eve, at least in early gastrulation, I observed indications of anterior-posterior segmentation in larval cuticles, as marked by ventral denticle belts (Figure 3.7C). As the pattern of denticle

belts is not normal, *xit* may affect later aspects during embryonic development, such as maintenance of anterior-posterior segmentation downstream of Eve.

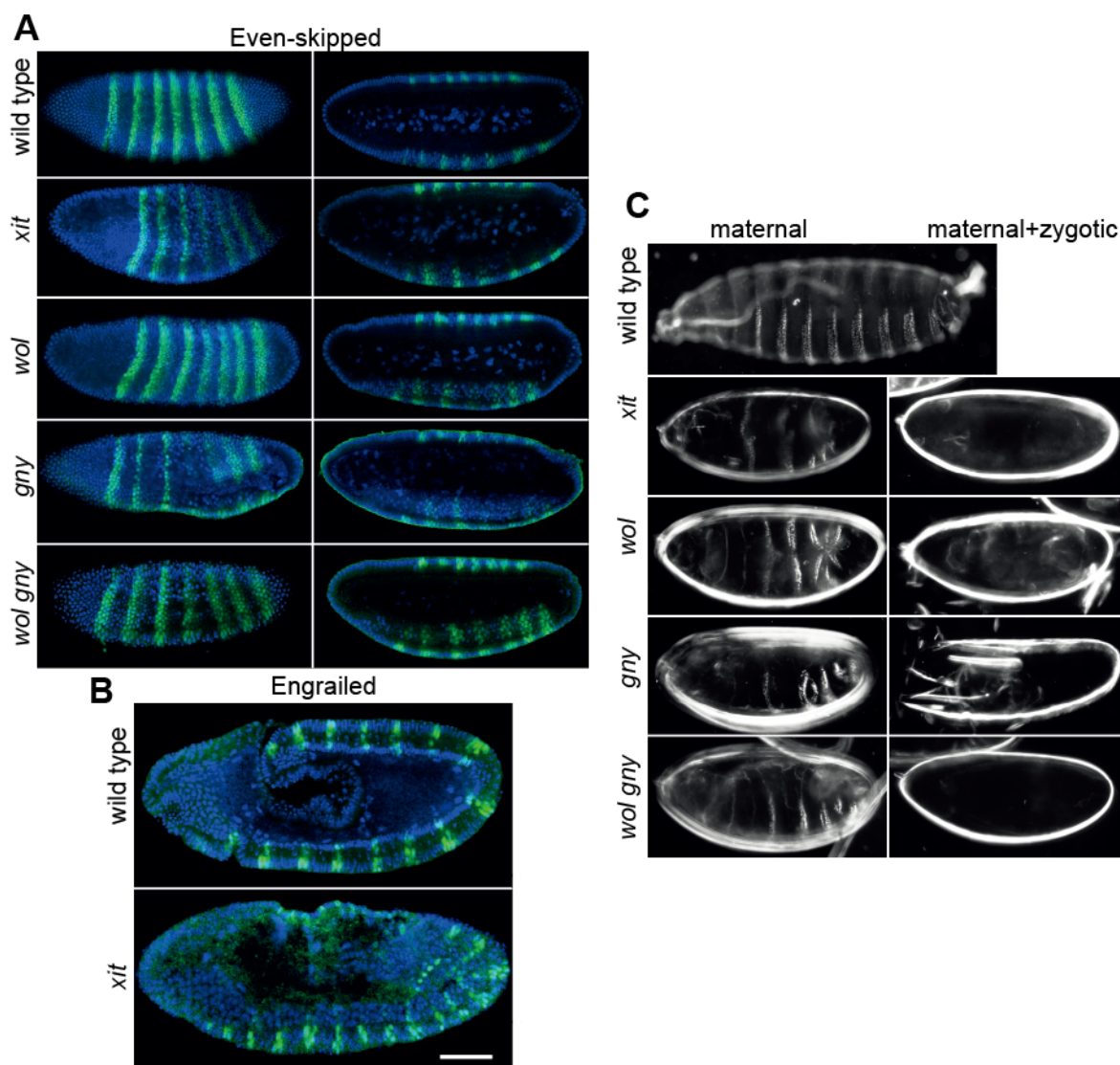


Figure 3.7 Embryonic polarities in *xit* mutants.

(A) Images of fixed wild type embryos and embryos from germline clones with indicated genotype that were stained for Even-skipped (green) and DNA (blue). (B) Images from fixed wild type embryos and *xit* germline clones which were stained for Engrailed (green,) and DNA (blue). Scale bar, 50 μ m. (C) Images of larval cuticles from females with indicated genotype of germline clones. Based on two clearly distinguishable phenotypes and an equal distribution, the cuticles were assigned as with (right pane) and without (left pane) zygotic rescue.

The striped pattern of *eve* expression is transformed into planar cell polarity. Planar cell polarity in the lateral epidermis is expressed by anisotropic distribution of Myo II at DV junctions and Baz at AP junctions (Figure 1.2B). Dr. Yujun Zhang applied the staining

of Baz/PAR-3 and F-actin in fixed embryos to check the planar cell polarity in *xit* embryos. A comparison of staining patterns of Baz/PAR-3 and F-actin did not reveal any obvious differences in wild type and *xit* embryos (Y. Zhang et al., 2014). Altogether, the data show that *xit* does not affect the embryonic AP polarity and planar cell polarity. Importantly, *wol* and *gny* embryos display the comparable germ-band extension phenotype, the Eve expression pattern at the onset of gastrulating embryos and the pattern of denticle belts in the larval cuticles (Figure 3.7), which is consistent with their functions in the same pathway (Figure 3.3). Thus, the data suggest that *xit* and its downstream targets participate at the machinery, which may directly affect the cell behaviours.

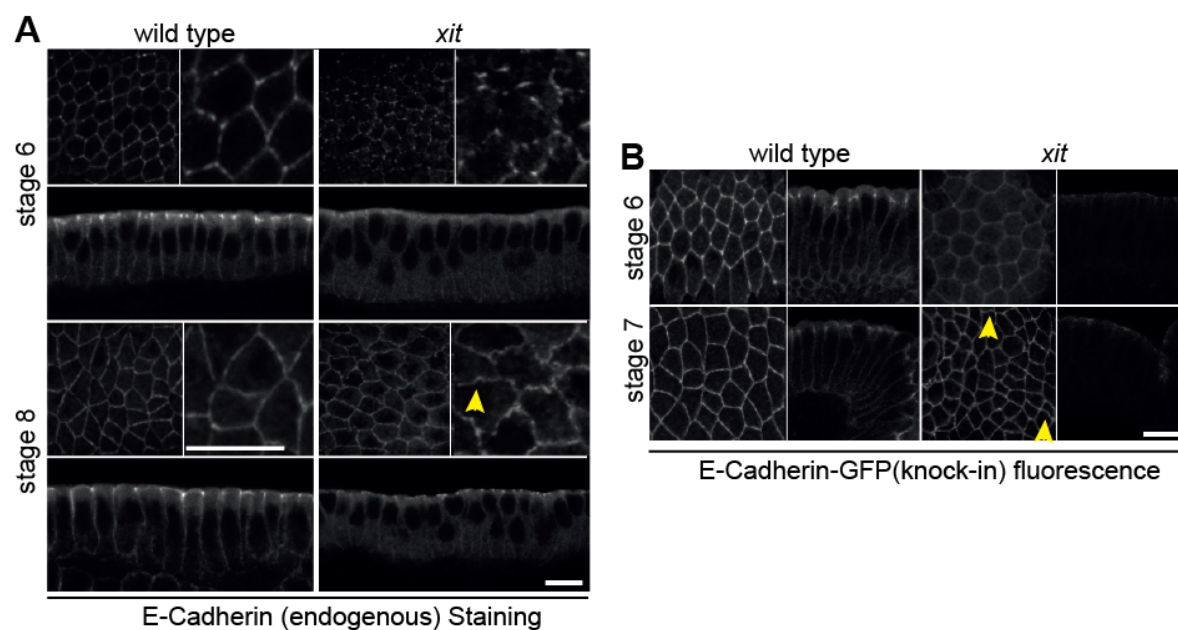


Figure 3.8 Xit is required for E-Cadherin distribution.

(A) Fixed embryos (wild type or from *xit* germline clones) were stained for E-Cadherin. Stages are indicated. Images in the plane of junctions are shown in low and high magnification. Arrows in yellow point to bulged junctions. Antibody staining of wild type and mutant embryos were performed in separate tubes. (B) Fixed embryos of E-Cad-GFP (knock-in) fluorescence in wild type embryos and embryos from *xit* germline clones. Scale bars, 10 μ m

3.4 *xit* is specifically required for efficient expression of E-Cadherin

E-Cad is a glycoprotein which is modified by N-glycosylation in the ER. E-Cad is required for cell intercalation during germ-band extension as the core protein of adherens junctions in the epidermis (Figure 3.5A) (Levayer et al., 2011; Levayer and Lecuit, 2013; Rauzi et al., 2010). Evidence from mammalian cells shows that the modification of N-linked glycans on E-Cad is required for its functions (Pinho et al., 2011). Several glycosyltransferases are involved in the remodelling of *N*-glycans on E-Cad (Pinho et al., 2011).

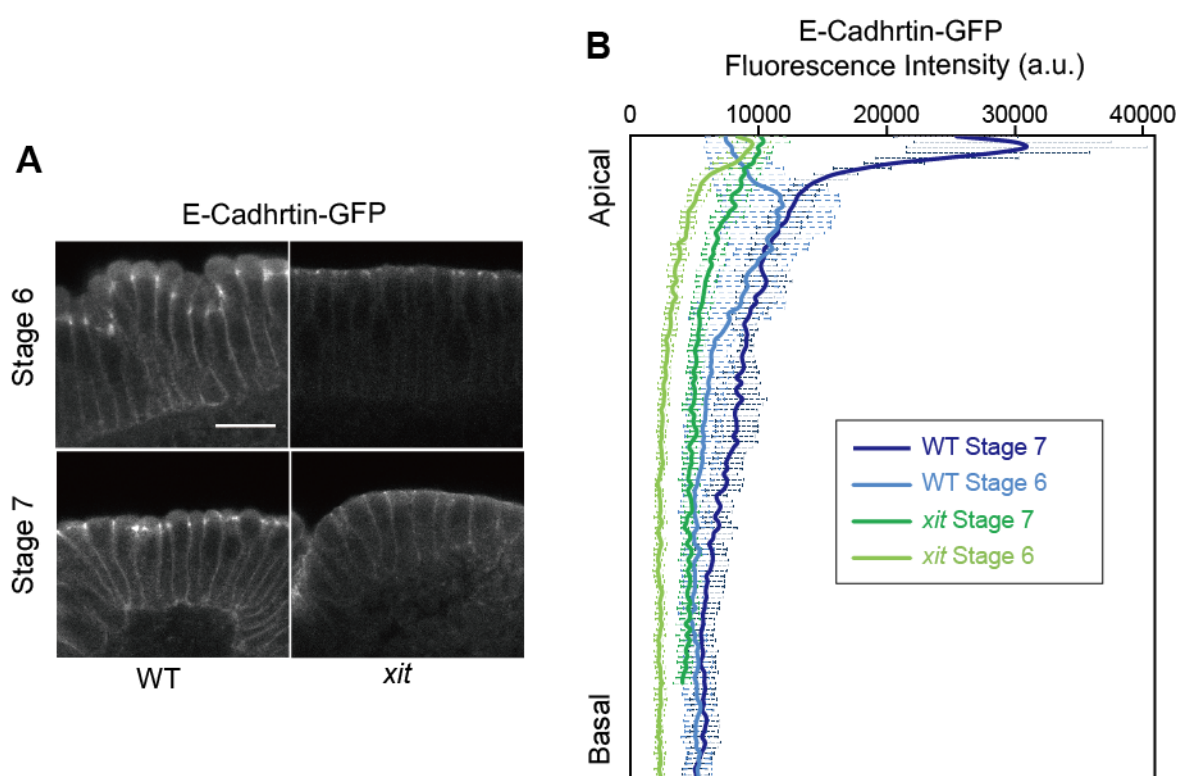


Figure 3.9 Xit is required for the polarized secretion of E-Cadherin.

(A) Images of embryos from E-cadherin-GFP (knock-in) and *xit*; E-Cadherin-GFP (knock-in) germline clones with indicated stages that were stained by GFP Booster 488. Scale bar, 10 μ m. (B) Mean of E-Cad-GFP Fluorescence intensity that was measured along the cell junction. The genotypes and stages are indicated. Error bars indicate standard deviation; N (cell junctions) = 11 (wild type stage 6), 14 (*xit* stage 6), 10 (wild type stage 7), 10 (*xit* stage 7).

Considering that *xit* is involved in protein glycosylation in the ER, I focused on E-Cad as a candidate target of *xit*. I first stained fixed embryos with an antibody against E-Cad (Figure 3.8A). I found that E-Cad was clearly reduced at the adherens junctions in

xit embryos, especially from the lateral view. Yet, the cell outlines were normal and no sign of a loss in epithelial organisation was observed. It suggests that the adhesive function of E-Cad seems not to be affected dramatically in *xit* embryos. The reduction of E-Cad was most obvious in the bright spots at adherens junctions, while the weak uniform fluorescence was comparable in wild type and mutants. In high magnification images, cell borders at adherens junctions appear as straight lines in wild type embryos, whereas I observed curved and uneven cell junctions in *xit* embryos especially during gastrulation (Figure 3.8, arrows in yellow). In addition to wild type embryos, I analysed E-Cad-GFP knock-in flies, in which the GFP sequence was knocked into the E-Cad endogenous gene locus and fused to the C-terminus of endogenous E-Cad (Huang et al., 2009). The homozygous E-Cad-GFP line is kept as a stock, and E-Cad expressing is comparable with wild type (Huang et al., 2009). Consistent with the staining results, E-Cad-GFP fluorescence was reduced in *xit* embryos (Figure 3.8B). Similar to E-Cad staining, I detected uneven junctions in *xit* embryos by E-Cad-GFP fluorescence (Figure 3.8B, arrow in yellow). Furthermore, the apical-basal polar distribution of E-Cad-GFP is affected in *xit* embryos especially during gastrulation (Figure 3.9). In wild type embryos, E-Cad-GFP is enriched at the sub-apical region at stage 6. The enrichments of E-Cad-GFP were observed at apical region in stage 7 embryos. In contrast, the weakened E-Cad-GFP enrichments were observed at apical region both in stage 6 and stage 7 *xit* embryos.

To overcome the reduced E-Cad levels at junctions in *xit* mutants, I overexpressed E-Cad-Cherry both in wild type and *xit* embryos. I did not observe a suppression of the phenotype in *xit* embryos with E-Cad-Cherry expressed by a maternal Gal4 driver. Staining of embryos with overexpressed E-Cad-Cherry showed increased cytoplasmic and ectopic signal apically to the nuclei in wild type embryos (Figure 3.10, stage 6, arrow in yellow). This may be due to E-Cad accumulating at the recycling endosome. In *xit* embryos, both features were less prominent. In addition, no prominent accumulation at the apical junctions was observed in *xit* embryos at the onset of gastrulation but a rather uniform distribution along the lateral membrane. At later stages of gastrulation, severe

morphological defects were observed in both wild type and *xit* embryos (Figure 3.10, stage 8/9).

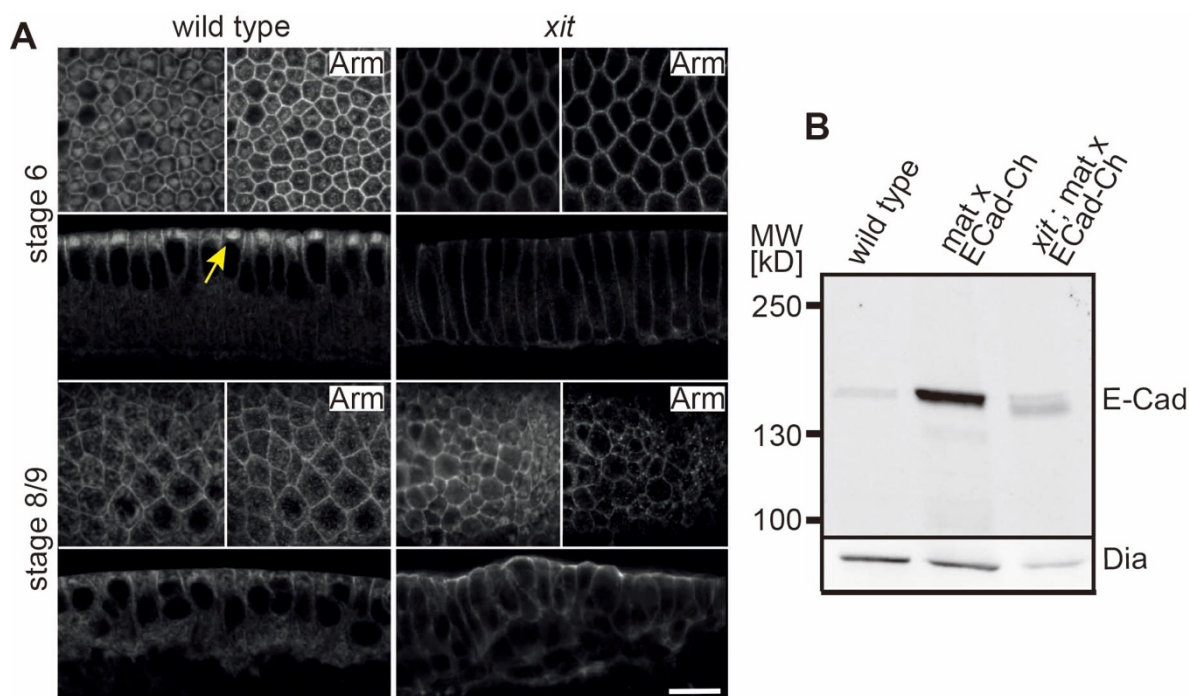


Figure 3.10 Overexpression of E-Cadherin in embryos.

(A) E-Cad-Cherry was overexpressed with a maternal GAL4 driver in wild type embryos and embryos from *xit* germline clones. Fixed embryos were stained for E-Cadherin and Arm. The arrow in yellow points to E-Cadherin accumulation apical to the nuclei. Antibody staining of wild type and mutant embryos was performed in separate tubes. Scale bar, 10 μ m. (B) Western blots of total lysates with E-Cadherin antibody. Genotypes as indicated. Loading was controlled by western blot with Diaphanous (Dia) antibody by reprobings stripped filters.

3.5 *xit* is required for N-glycosylation of E-Cadherin

The three terminal glucose residues are necessary for recognition by OST to transfer the mature glycan to nascent proteins (Aebi et al., 2010). Furthermore, it is presumed that the terminal glucose residues are important for the nascent glycoprotein folding during ER quality control (Aebi et al., 2010). Immediately following N-glycosylation, the three glucose residues are removed. It is presumed that this serves as a timer allowing protein folding. Proteins with one glucose residue left are subject to ER quality controls. Based on this model, the amount of E-Cad protein should be reduced in *xit* mutants. In addition to ER quality control, an incomplete N-glycosylation may affect the E-Cad distribution and functions in the plasma membrane. To address these questions, I analyzed total E-Cad protein levels by western blot analysis of total

embryonic extracts (Figure 3.11A). The integrated western blot signal of E-Cad was normalized with that of Diaphanous (Dia) while assuming that the cytoplasmic protein Dia would not be affected by *xit*. From multiple western blot experiments, comparable amounts of E-Cad were detected in wild type and *xit* mutant extracts (Table 3.1). Importantly, I got the similar results with *wol*, *gny* and *wol gny* double mutant embryos (Table 3.1). These data show that *xit*, *wol* and *gny* are not required for E-Cad protein expression and that absence or reduced number of the glucose residues on N-glycans does not lead to E-Cad degradation as part of the ER quality control mechanism. These results are consistent with the function of N-Glycan in the mammalian E-Cad. It was reported that only N-Glycan at Asn 633, which is 1 in 4 N-glycosylation sites, are essential for E-Cad folding, trafficking and its proper expression (Zhou et al., 2008).

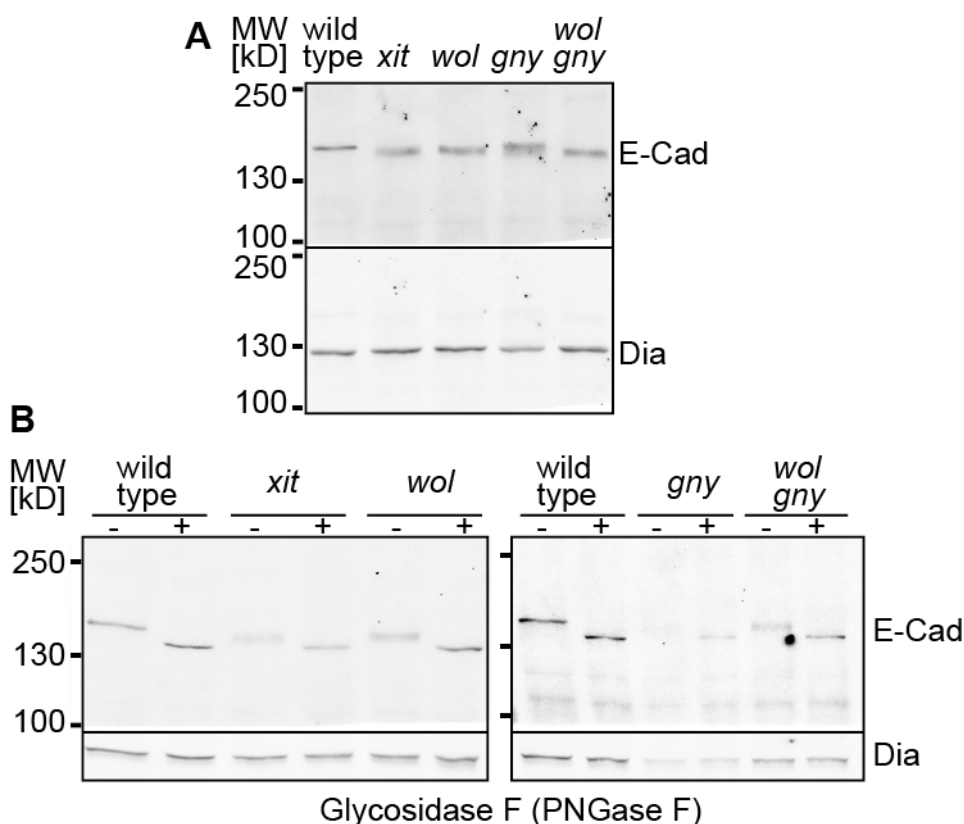


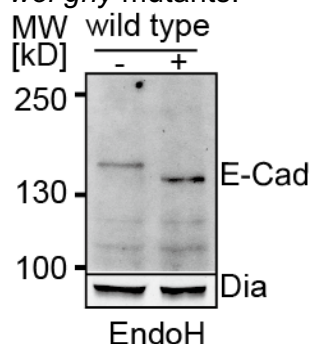
Figure 3.11 E-Cadherin is Hypo-N-glycosylated in *xit* mutants.

(A) Western blots of total lysates with E-Cadherin antibody. Genotypes as indicated. Loading was controlled by western blot with Diaphanous (Dia) antibody by reprobing stripped filters. (B) Embryonic lysates were treated with buffer (-) or glycosidase F (+).

Table 3.1 E-Cadherin protein levels in total embryonic extracts.

Genotype	Normalised expression (\pm S.E.M)	no. of western blots
wild type	1	-
<i>xit</i>	0.99 \pm 0.05	5
<i>wol</i>	1.03 \pm 0.09	5
<i>gny</i>	1.3	2
<i>wol gny</i>	0.93 \pm 0.04	3
wild type	0.28	1
mat x ECadCherry	1	3
<i>xit</i> ; mat x ECadCherry	0.83 \pm 0.02	3

The western blots revealed a band shift to a lower apparent molecular weight of E-Cad in *xit* as well as *wol*, *gny* and *wol gny* embryos (Figure 3.11A). This band shift is due to incomplete glycosylation as treatment of the extracts with glycosidase F (PNGase), which cleaves the amide bond between asparagine side chain and GlucNAc (T H Plummer and Tarentino, 1991), shifted wild type and mutant bands to a similar apparent molecular weight (Figure 3.11B). Interestingly, the bands were more diffuse in mutants than wild type extracts. They were as sharp as in wild type after treatment with PNGase. An explanation for the diffuse band is that multiple forms of E-Cad with more or less N-glycans are present. Altogether, the results suggest that E-Cad is hypo-N-glycosylated in *xit*, *wol*, *gny* and *wol gny* mutants.

**Figure 3.12 Western blots of total lysates treated by Endo H with E-Cadherin antibody.**

Embryonic lysates were treated with buffer (-) or Endo H (+). Loading was controlled by western blot with Diaphanous (Dia) antibody by reprobng stripped filters.

Following N-glycosylation in the ER, proteins within the secretory pathway are subjected to further modifications in the Golgi. For example, one such modification is mannosyl-trimming of the N-glycans in vertebrates. Endoglycosidase H (EndoH)

cleaves N-glycans with high mannose content (Maley 1989), thus allowing to distinguish protein pools before (EndoH sensitive) and after Golgi passage (EndoH resistant). However, treatment of wild type extracts resulted in a complete shift of the E-Cad band (Figure 3.12), similar to the shift from Glycosidase F treatment, indicating a high mannose content and absence of Golgi modification. This result is consistent with the literature, as mannosyl-trimming is not typical for *Drosophila*, where a high abundance of high mannose N-glycans are commonly observed (Aoki et al., 2007; Hagen et al., 2009; Katoh and Tiemeyer, 2013).

Overexpressed E-Cad-Cherry showed the same migration speed in SDS-PAGE as endogenous E-Cad in wild type embryos, indicating that N-glycosylation is complete (Figure 3.10B). As the endogenous E-Cad, overexpressed E-Cad in *xit* embryos migrated with a slightly higher speed in SDS-PAGE (Figure 3.10B), indicating that N-glycosylation of overexpressed E-Cad is not complete, and the function of overexpressed E-Cad was affected in *xit* embryos. These data suggest that glycan transfer to E-Cad is not rate-limiting for E-Cad expression.

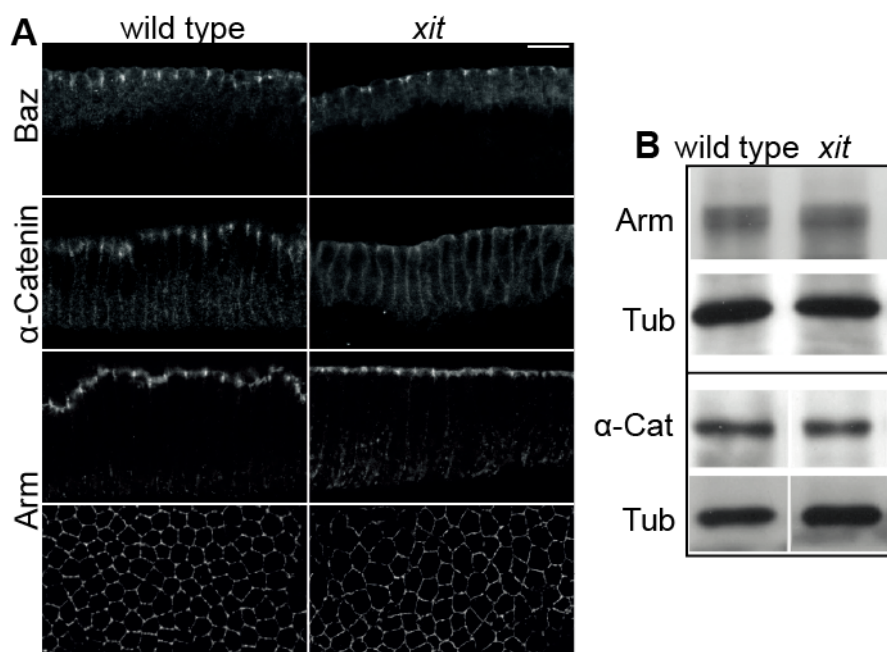


Figure 3.13 Adherens junctions are not obviously affected in *xit* mutants.

(A) Images of fixed wild type and *xit* mutants stained for α -Catenin, Armadillo (Arm) and Bazooka (Baz) in a cross section. Scale bars, 10 μ m. (B) Western blots of embryonic extracts from wild type and *xit* embryos for Armadillo, α -Catenin, and β -Tubulin (as loading control).

3.6 Adherens junctions in *xit* and E-Cadherin RNAi embryos

As E-Cad is the core component of adherens junctions, by forming extracellular *trans*-interactions and intracellular cadherin-catenin complex with α -Catenin and Arm. I would expect that the E-Cad dispersed localization and reduced subapical levels would affect adherens junctions formation and lead to defective epithelial tissue morphology. However, staining of α -Catenin and Arm in fixed wild type and *xit* embryos did not show any obvious differences at gastrulation stage (Figure 3.13A). Furthermore, the protein amount of α -Catenin and Arm were comparable in wild type and *xit* in western blot of embryo extracts (Figure 3.13B). In addition, accumulation of Baz, that specifies the sub-apical region and is required for formation of adherens junctions (Harris and Peifer, 2004; Müller and Wieschaus, 1996), was comparable in wild type and *xit* embryos. The normal expression levels and distribution of α -Catenin and Arm in *xit* embryos are consistent with the observed epithelial morphology of *xit* embryos. The epithelial character was maintained in *xit* at least until stage 9.

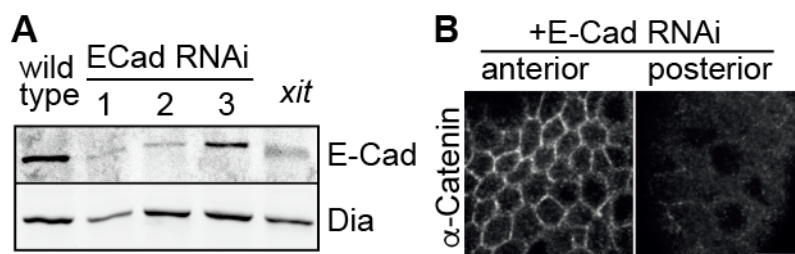


Figure 3.14 E-Cadherin protein level is reduced by RNAi treatment.

(A) Western blots of total lysates with E-Cadherin antibody. Embryos were injected with E-Cadherin dsRNA (three independent experiments). Loading was controlled by western blot with Diaphanous (Dia) antibody by reprobing stripped filters. (B) Images from the anterior and posterior part of an embryo which was injected with E-Cad dsRNA from the posterior pole and stained for α -Catenin. Note that staining is reduced at the site of injection. Scale bars, 10 μ m.

It was reported previously that E-Cad is required for germ-band extension and cell intercalation, as demonstrated by depletion of E-Cad by RNAi (Levayer et al., 2011; Levayer and Lecuit, 2013; Rauzi et al., 2010). In my results, germ-band extension and cell intercalation phenotype induced by RNAi mediated depletion of E-Cad and *xit*

mutation are comparable. In both cases, the germ-band only extended to 30% of embryonic length after 30 minutes of the onset of germ-band extension and did not extend further in the following 30 minutes (Figure 3.5). Western blot of total embryo extracts showed that E-Cad protein amount is clearly reduced in multiple experiments (Figure 3.14A). Although most embryos injected with E-Cad RNAi maintained an epithelial character, a strong reduction of α -Catenin staining at junctions was observed following E-Cad RNAi injection at the posterior injection site (Figure 3.14B).

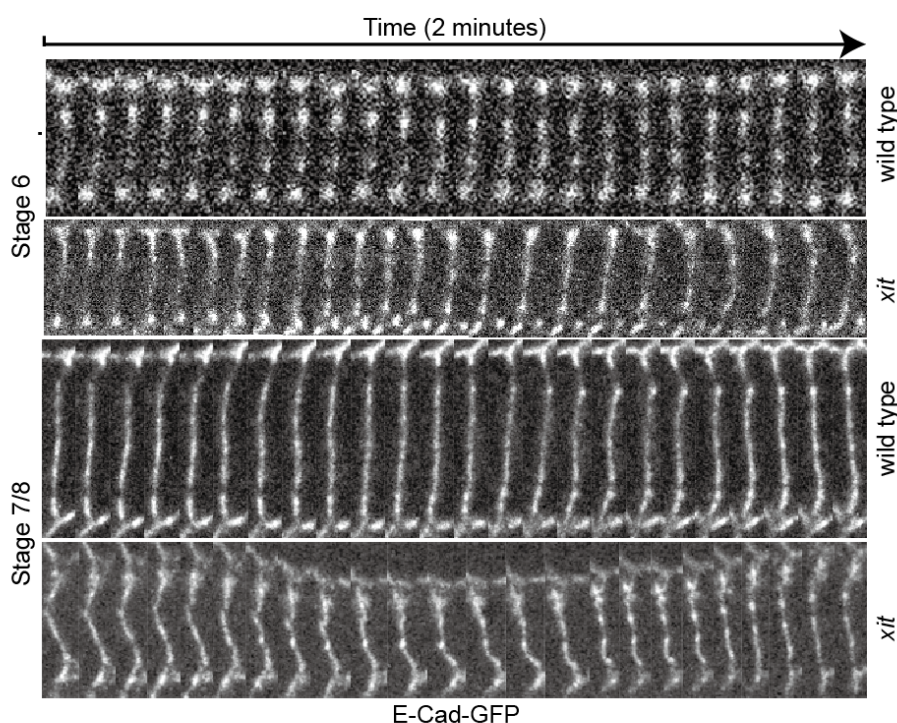


Figure 3.15 Dynamics of E-Cadherin are affected in *xit* mutants.

Kymograph of the E-Cad distribution along a single cell border from time lapse movies with wild type and *xit* embryos expressing E-Cad-GFP. Stages are indicated.

3.7 Developmental control of E-Cadherin mobility is *xit* dependent

It has been reported that N-glycosylation of E-Cad is required for the stability of adherens junctions (Liwosz et al., 2006; Zhao et al., 2008). E-Cad forms the cluster structures at adherens junctions and clustered E-Cad is showing higher stability than un-clustered uniformly distributed E-Cad (Cavey et al., 2008; Truong Quang et al., 2013). I checked the dynamics of E-Cad clusters by live imaging with E-Cad-GFP. Kymographs

from time lapse images showed that the E-Cad clusters were more unstable in *xit* embryos, especially at the later stage of gastrulation (Figure 3.15).

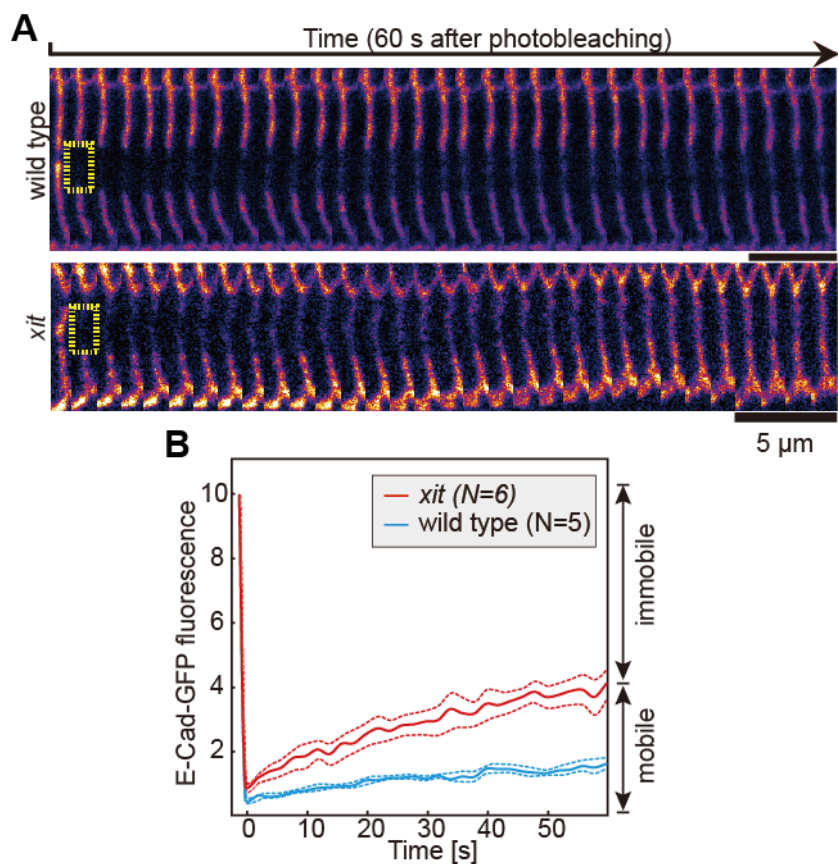


Figure 3.16 E-Cadherin clusters are more mobile in *xit* mutants.

(A) Typical kymograph of E-Cad recovery after photo bleaching in stage 7 wild type and *xit* embryos expressing E-Cad-GFP. Yellow boxes indicate the bleaching regions. (B) Mean of E-Cad-GFP fluorescence recovery after photo bleaching. The initial E-Cad-GFP fluorescence is normalized to 10. Dashed lines indicate confidence intervals of the standard error of the mean.

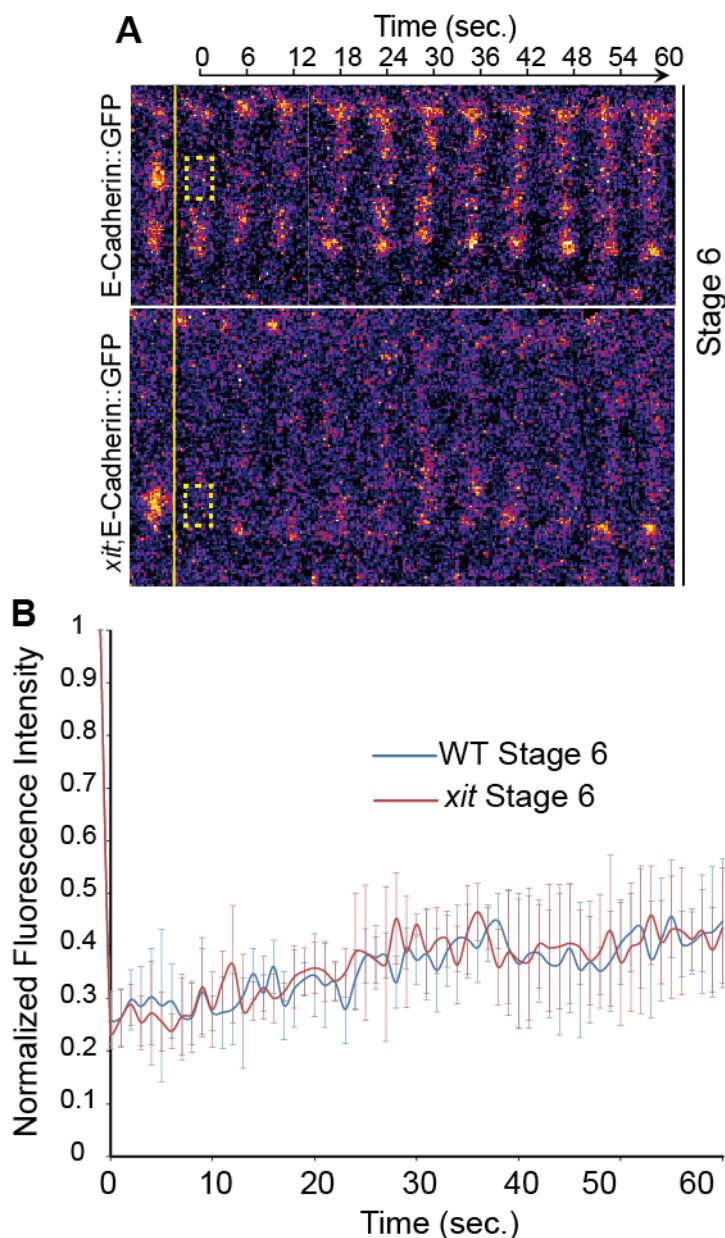


Figure 3.17 E-Cadherin clusters mobility is normal at the early stage in *xit* mutants.

(A) Typical kymograph of E-Cad recovery after photo bleaching in stage 6 wild type and *xit* embryos expressing E-Cad-GFP. Yellow boxes indicate the bleaching regions. (B) Mean of E-Cad-GFP fluorescence recovery after photo bleaching. The initial E-Cad-GFP fluorescence is normalized to 1. Error bars indicate confidence intervals of the standard error of the mean.

As the uniform E-Cad-GFP fluorescence was not much different in wild type and *xit* fixed embryos (Figure 3.8). I characterized the dynamics of E-Cad clusters at adherens junctions of lateral epidermal cells using the knock-in E-Cad-GFP in wild type and *xit* embryos. I analyzed its molecular dynamics using fluorescent recovery after

photobleaching (FRAP). By performing FRAP in visible clusters (bright spots), I found that E-Cad-GFP dynamics were different in gastrulating (stage 7/8) wild type and *xit* embryos (Figure 3.16). The representative kymographs and fluorescence recovery curves showed that fluorescence recovery was obviously faster in *xit* than in wild type embryos. The mobile fraction was significantly higher in *xit* (34.3%) than in wild type (11.5%) embryos (Figure 3.18). Interestingly, both fluorescent recovery and mobile fraction are comparable in wild type and *xit* embryos at stage 6 (onset of gastrulation) (Figure 3.17, 3.18).

The FRAP experiments showed that the mobile fraction of E-Cad clusters at the later stage (11.5%) reduced significantly compared with early stage (25.7%) in wild type embryos during gastrulation (Figure 3.18). It suggests a developmental control of E-Cad clusters mobility at the embryo lateral epidermal cells during gastrulation.

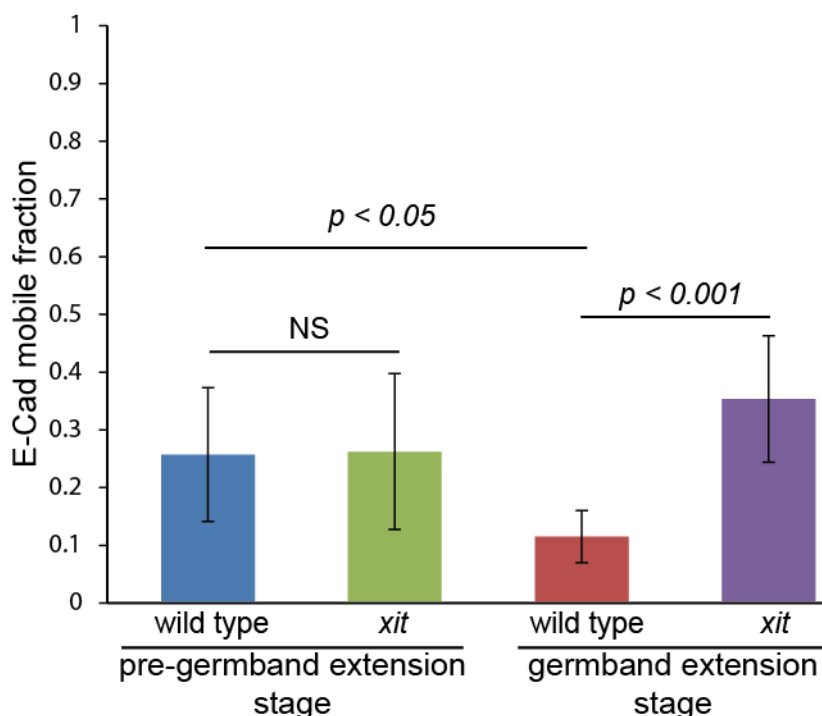


Figure 3.18 Developmental control of E-Cadherin clusters mobility.

Histograms show the mean of E-Cad-GFP mobile fraction. Pre germ-band extension stage, stage 5b/6. Germ-band extension stage, stage 7. The genotypes are indicated. Error bars indicate confidence intervals of the standard error of the mean. $N = 4$ (wild type stage 5b/6), 5 (wild type stage 7), 3 (*xit* stage 5b/6) and 6 (*xit* stage 7). The P values are calculated from paired Student's t -tests.

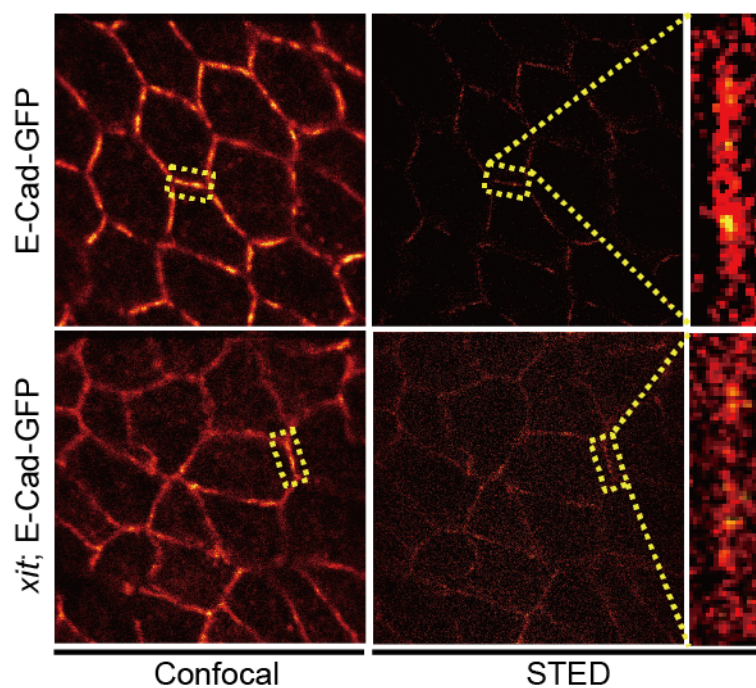


Figure 3.19 E-Cadherin cluster size is reduced in *xit* mutants.

STED images from fixed stage 7 embryos expressing E-Cad-GFP from wild type and *xit*. High magnification shows E-Cad-GFP distribution along one cell border.

The developmental control of E-Cad clusters mobility was not observed in *xit* embryos, in which E-Cad was hypo-N-glycosylated (Figure 3.18). It has been reported that the clustered E-Cad is showing higher stability than un-clustered uniformly distributed E-Cad both in *Drosophila* embryos and mammalian cells (Cavey et al., 2008; Engl et al., 2014). It suggests that E-Cad immobilization may be correlated with its cluster size somehow. Using the stimulated emission depletion (STED) microscopy, E-Cad distribution showed obvious differences in *xit* embryos (Figure 3.19). The bright spots of E-Cad-GFP in *xit* embryos were smaller than in wild type embryos at stage 7/8, consistent with the reduced E-Cad immobilization in *xit* embryos at the same stage (Figure 3.16). For the developmental control of E-Cad clusters mobility, local E-Cad recruitment may be affected in *xit* embryos during gastrulation, alternatively, since E-Cad is hypo-N-glycosylated in *xit* embryos, E-Cad *cis*-interaction may be affected, the contraction of actin-myosin networks may split the E-Cad clusters and affect E-Cad/F-actin interaction consequently.

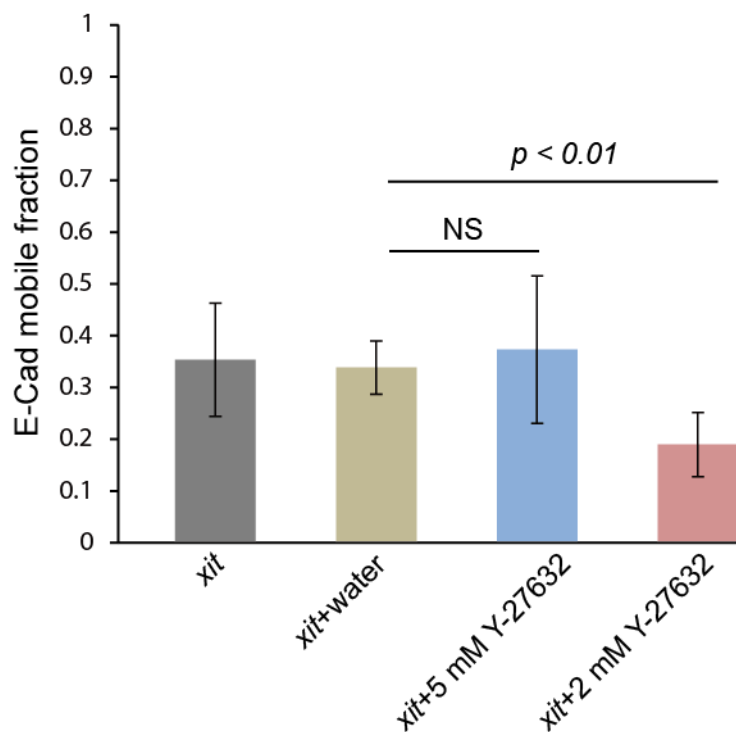


Figure 3.20 E-Cadherin clusters mobility is increased by Myosin-II in *xit* mutant.

Histograms show the mean of E-Cad-GFP mobile fraction at stage 7. The genotypes and treatments are indicated. Error bars indicate confidence intervals of the standard error of the mean. $N = 6$ (*xit*), 5 (*xit* + water), 4 (*xit* + 5 mM Y27632) and 5 (*xit* + 5 mM Y27632). The P values are calculated from paired Student's t -tests.

I next inhibited the actin-myosin contractility via Y-27632 injection in *xit* embryos and applied FRAP for E-Cad-GFP at the later stage of gastrulation (stage 7/8). The phenotype was partially rescued by inhibition of actin-myosin contractility (Figure 3.20). The GFP fluorescent recovery and mobile fraction were comparable in no-injected, water injected, and 5 mM Y-27632 injected *xit* embryos. Interestingly, when the Y-27632 concentration was decreased to 2 mM, E-Cad-GFP fluorescence recovery was slower than water injected *xit* embryos, and E-Cad-GFP mobile fraction reduced to 19.0% from 33.8% (water-injection).

In summary, these data suggest a *xit*-dependent developmental control of E-Cad clusters mobility during gastrulation. Actin-myosin contractility may support E-Cad local recruitment and immobilization during gastrulation, whereas it may suppress E-Cad local recruitment and/or affect E-Cad immobilization in the case of hypo-N-glycosylated E-Cad.

3.8 N-Glycosylation of E-Cadherin is important for mechanical signal coupling in neighboring cells

By the *trans*-interaction of E-Cad molecules, E-Cad generates mechanical stability of cell-cell contacts via cell adhesion and adhesion tension. Furthermore, the cytoplasmic domain of E-Cad interacts with the F-actin cytoskeleton via α and β -catenin and such interactions play very important roles for mechanical signal coupling in neighboring cells (Maître and Heisenberg, 2013). I next investigated whether the N-glycosylation modification of E-Cad is required for its mechanotransduction function using the amnioserosa tissue.

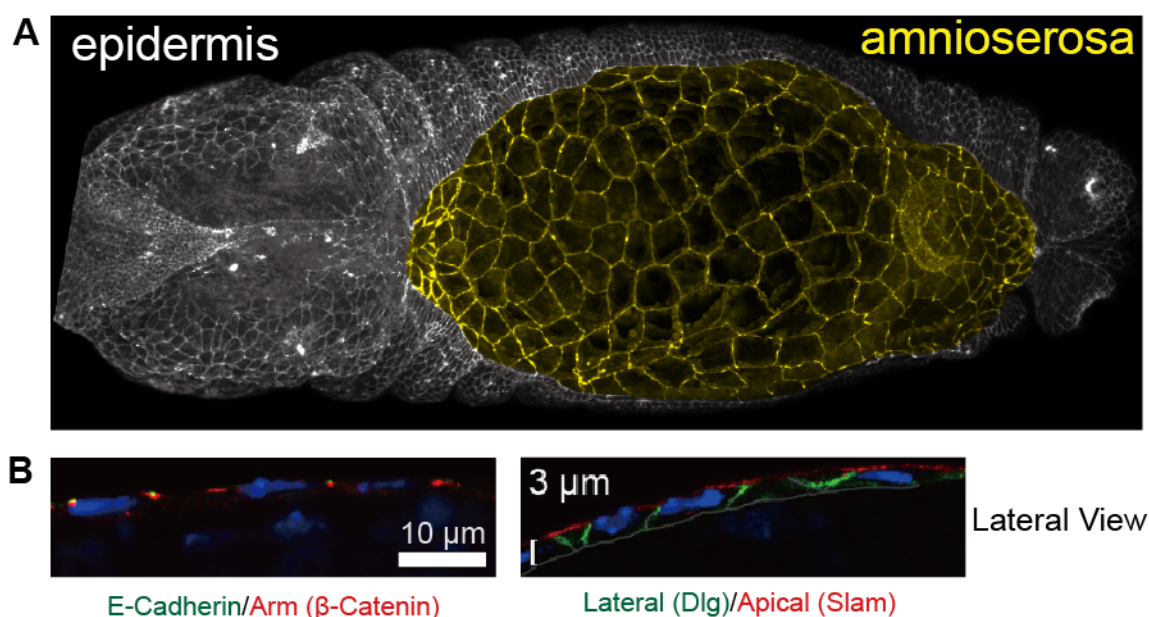


Figure 3.21 Cell morphology in Amnioserosa in *Drosophila* embryos.

(A) The squamous epithelium of the extra-embryonic amnioserosa closes the dorsal gap between the lateral epidermis on the left and right side of the embryo. Projected image from fixed E-Cad-GFP embryos stained by GFP-booster 488. Amnioserosa is highlighted in yellow. (B) Lateral cross sections of AS cells from fixed E-Cad-GFP embryos, which were stained for E-Cad-GFP, β -Catenin, Slam, and Dlg. Scale bars, 10 μ m.

3.8.1 Cell behaviors in amnioserosa

Following the germ-band retraction, the dorsal surface of the embryo is occupied by the amnioserosa (AS) (stage 14-15) (Figure 3.21A). Different than the lateral epidermis, the AS is a typical squamous epithelium of about 200 large and flat cells with

more than 15 μm diameters of cell surface and 3 μm apical-base length (Figure 3.21B). The whole epidermis then moves towards dorsal and left and right sides fuse and close along med line, a process called 'dorsal closure' (Harden, 2002) (Figure 3.22A). The AS tissue reduces its surface area, in those individual cells which contract, and are extruded from the epithelial sheet and finally undergo apoptosis (Mulyil et al., 2011; Toyama et al., 2008).

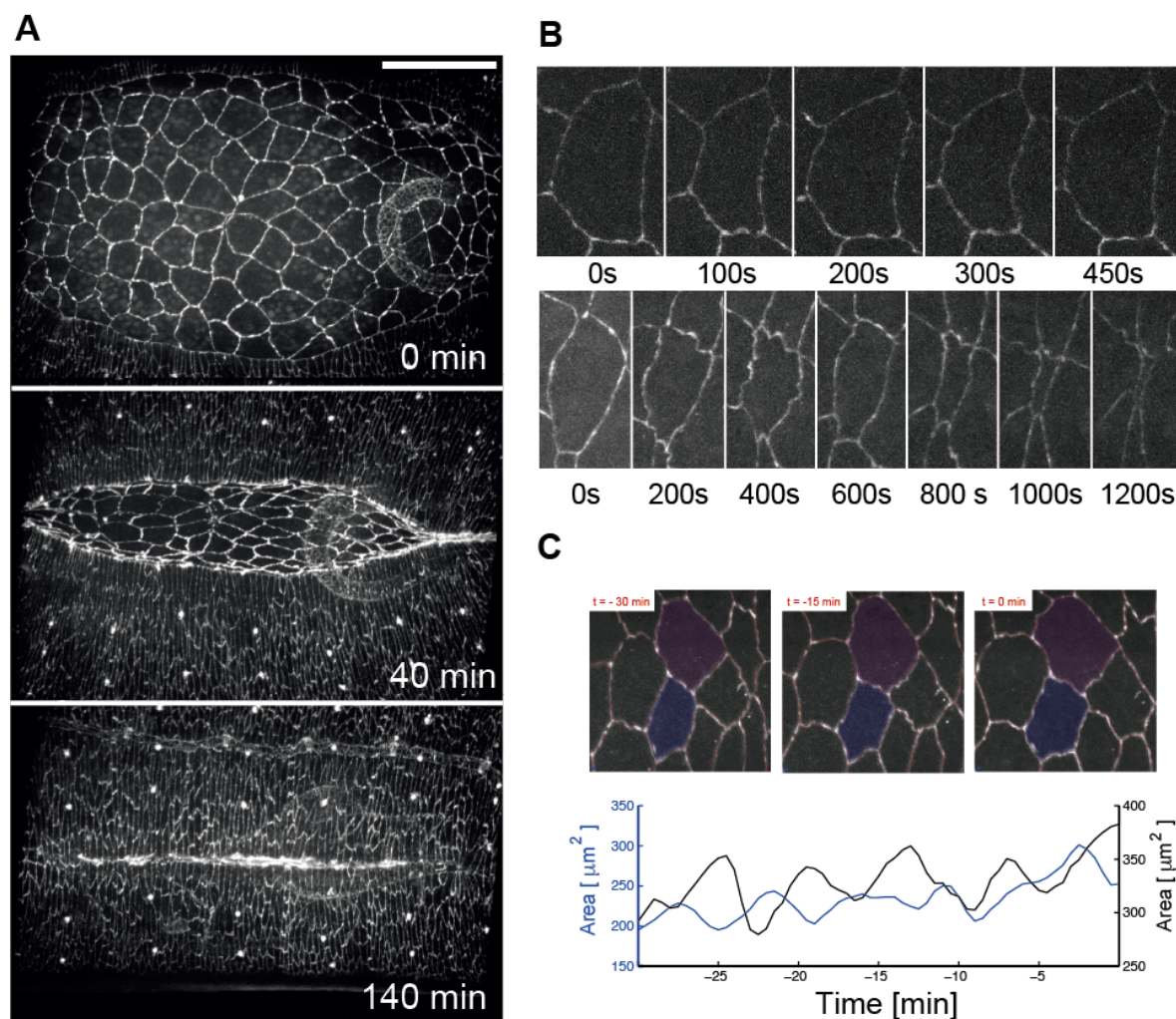


Figure 3.22 Oscillatory dynamics are correlative between neighboring cells in amnioserosa.

(A) During stage 15, the amnioserosa continuously decreases to allow fusion of epidermis along the dorsal midline. Scale bar, 50 μm . (B) Oscillation of surface area of an amnioserosa cell and constriction of an amnioserosa cell (top pane). Constriction of an amnioserosa cell (bottom pane). (C) Cell pair used in the characterization of coordinated cellular contractions at times -30 min, -15 min and 0 min prior to the onset of dorsal closure. The area measurements indicate anti-correlated area fluctuations of neighboring cells. Embryos expressed E-Cad-GFP from an endogenous promoter.

It has been reported that the AS cells undergo striking apical cell surface fluctuations before and during dorsal closure, which are required for the dorsal closure completion (Solon et al., 2009) (Figure 3.22B). Initial analysis of examples of cell fluctuations in neighboring cells suggested that the oscillations may be coordinated (Solon et al., 2009). In our analysis of cell fluctuations, we obtained the consistent results (Figure 3.22C) (collaboration with Dr. Lars Reichl).

3.8.2 Morphology of amnioserosa is affected in *xit* embryos

In later developmental stages I observed two classes of *xit* embryos. The first class passed through germ-band retraction and abnormal dorsal closure and formed cuticles. The second class was morphologically abnormal and did not form cuticles. Consistent with the results from larval cuticles (Figure 3.7C), a fraction of embryos developed through dorsal closure, in which the zygotic *xit* is assumed expressed. However, the morphology of amnioserosa was affected in these embryos (Figure 3.23A). The interface between epidermis and amnioserosa was disrupted in *xit* mutants losing its straightness. Similar with the phenotype of epidermis at gastrulation stage, I observed a larger amount of the high winding cell borders in AS (Figure 3.23A). Consistently, the kymographs from time lapse images showed that E-Cad clusters were more unstable in *xit* embryos in the AS (Figure 3.23B). I observed striking differences of cell surface size and distribution pattern. In wild type embryo, AS cells near to the interface with epidermis are smaller than the AS cells at the middle region normally. AS cells distributed homogeneously with comparable cell surface size in the middle region of AS. Whereas, I did not observe the comparable cell apical size and cell distribution pattern in *xit* embryos. I furthermore observed a difference in F-actin organization (Figure 3.23C). In wild type embryos, F-actin labels the cell-cell junctions and accumulates in clusters that are most likely associated with the apical plasma membrane. In *xit* embryos, overall staining appeared stronger and more foci within cells were observed.

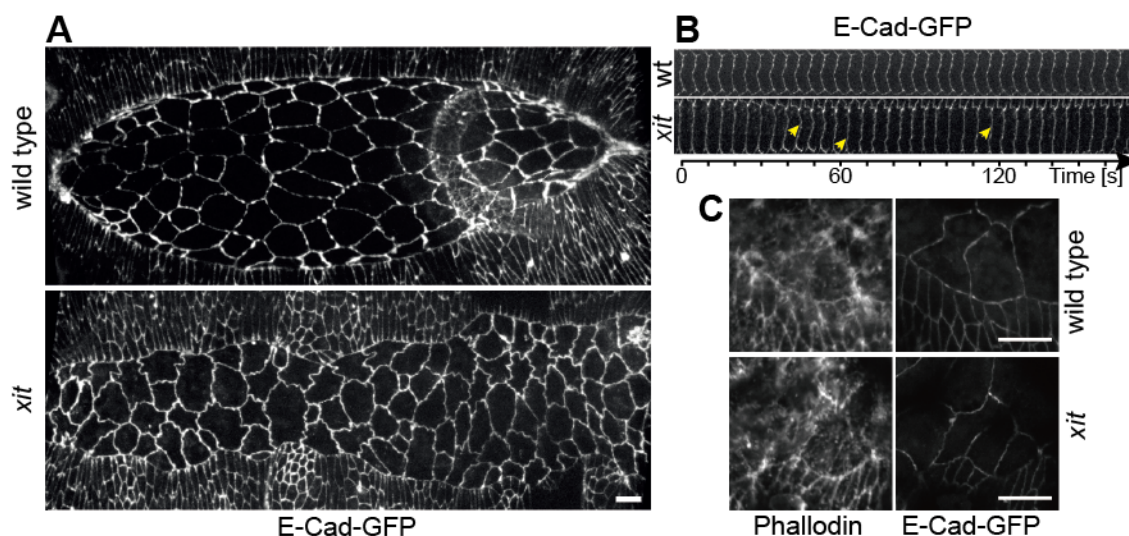


Figure 3.23 Morphology of amnioserosa in wild type and *xit* embryos.

(A) Morphology of the amnioserosa in wild type and *xit* embryos expressing E-Cad-GFP. (B) Kymograph of the E-Cad distribution along a single cell border of AS cells from time lapse movies with wild type and *xit* embryos expressing E-Cad-GFP. (C) F-actin was stained by phalloidin in fixed wild type and *xit* embryos. The genotypes are indicated. Scale bars, 10 μm .

3.8.3 N-glycosylation of E-Cadherin is required for response of neighboring cells in amnioserosa

I next applied individual junctions cutting with a pulsed UV laser to probe the mechanical properties of the AS tissue (Figure 3.24). As reported previously (Solon et al., 2009), oscillations in immediate neighbors were blocked for at least 5 min after cutting. In contrast, oscillations in immediate neighboring cells proceeded in *xit* embryos (Figure 3.24B). This qualitative observation suggests that oscillations in *xit* mutants are less dependent on the mechanical integrity of the tissue than in wild type embryos. Quantification of area fluctuations showed the area variance of immediate neighbors ($50 \mu\text{m}^4$) decreased dramatically compared to no-cut embryos ($250 \mu\text{m}^4$) in wild type. In contrast, the decrease of area variance is much weaker in *xit* embryos, from $200 \mu\text{m}^4$ (immediate neighbors) to $150 \mu\text{m}^4$ (no-cut) (collaboration with Dr. Lars Reichl). Altogether, the data suggest that N-Glycosylation of E-Cad is important for mechanical signal coupling in neighboring cells.

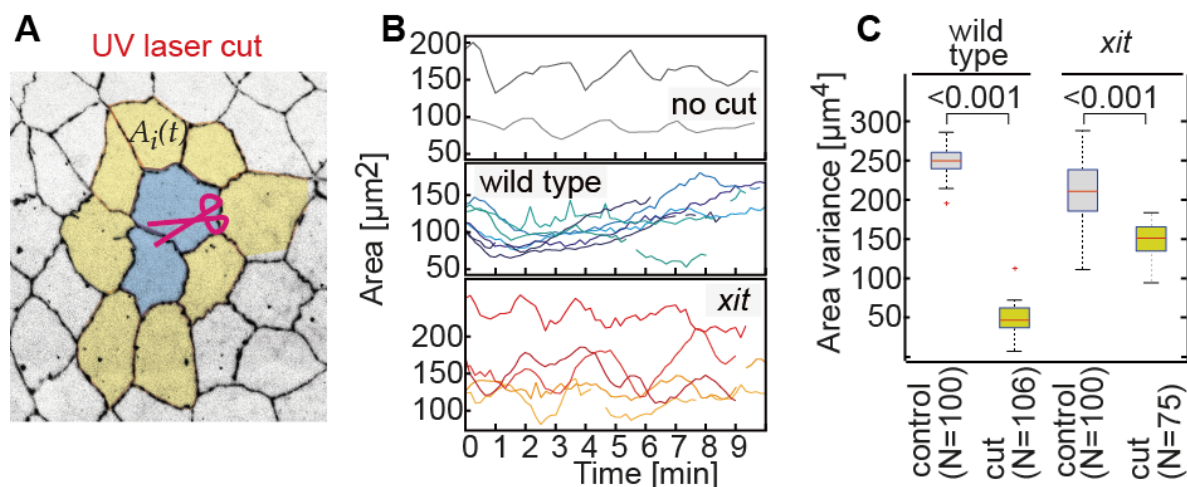


Figure 3.24 Response of neighboring cells depends on *xit* in amnioserosa.

(A) Scheme for junction cuts in the amnioserosa, which is characterized by robust cell oscillations. Cell borders were labeled with E-Cad-GFP. (B) Single neighboring cell area tracking in no-cut, wild type, and *xit* embryos. (C) Boxplots show the area variance of control (no-cut) and cut (neighboring cells of cut, yellow in (A)) in wild type and *xit* embryos. Red horizontal line, mean. Box, second and third quartiles. Black horizontal line with whisker, confidence interval. The P values are calculated from paired Student's t -tests.

3.8.4 Hypo-N-Glycosylation of E-Cadherin reduces the coupling between E-Cadherin and cytoskeleton

I next applied the UV-laser ablation for individual junctions of AS cells in wild type and *xit* embryos and analyzed the recoil velocity by the displacement of two 3x vertices (Figure 1.5). Using the displacement between the first and second frames after laser ablation, I calculated the initial recoil velocity (Figure 3.25A). I observed increased initial recoil velocity in *xit* embryos (Figure 3.25B). The increased initial recoil velocity suggests two potential mechanisms, (1) the junctions were under high tension, (2) the resistance originated from friction between junctions and the F-actin cytoskeleton was subdued (Weitkunat et al., 2014). In general, increased tension is supposed to straighten cell borders (Nowotarski and Peifer, 2014). As the cell borders were winding, it suggests that cell borders are under lower tension in *xit* embryos. So, the increased initial recoil velocity could be contributed by the subdued friction-like resistance, which depends on the interaction of E-Cad with F-actin cytoskeleton in the case of AS cells. The data may

be explained by an affected E-Cad/F-actin interaction in *xit* embryos, in which E-Cad is hypo-N-glycosylated.

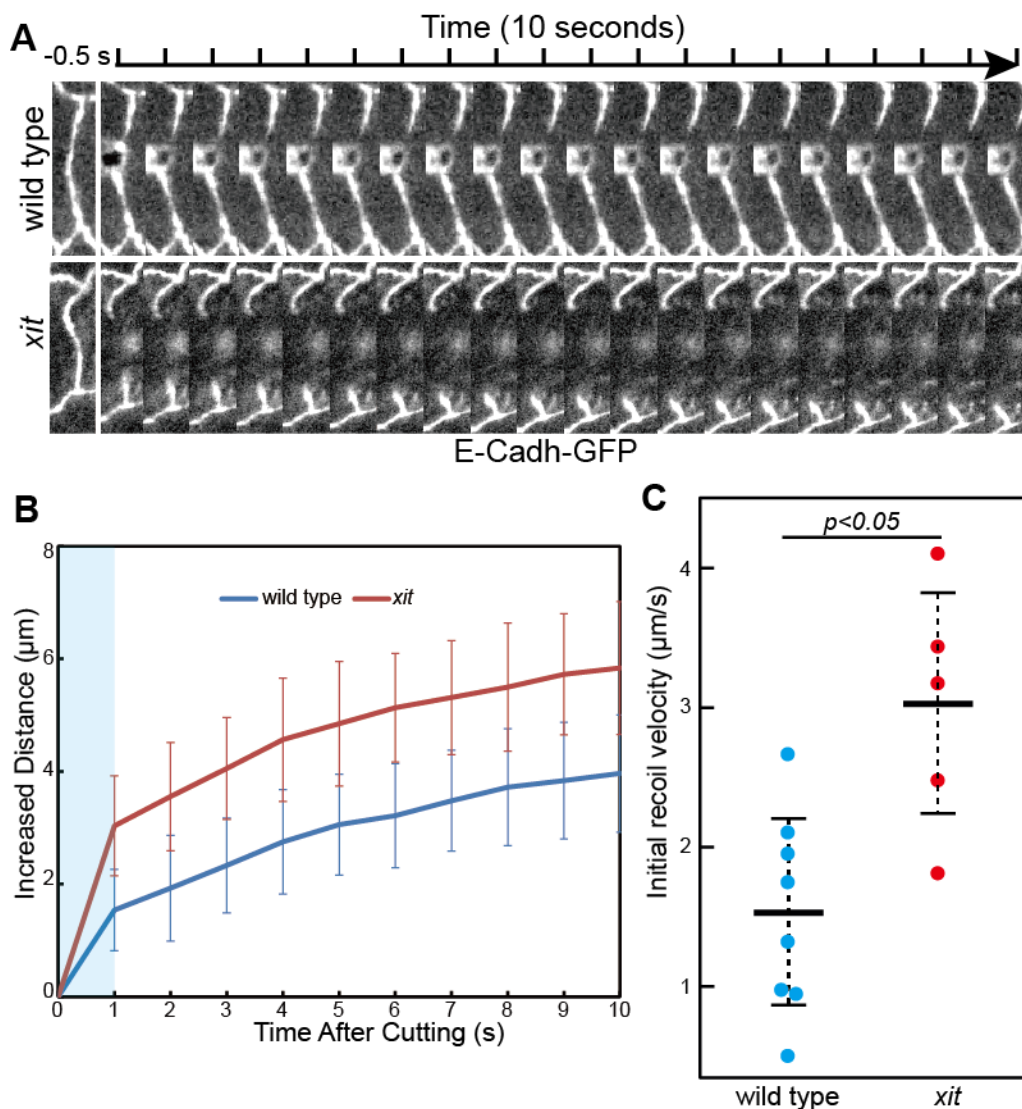


Figure 3.25 *Xit* increases recoil velocity at the junctions after UV-laser cut.

(A) Kymograph of single cell borders of AS cells before and after UV-laser cutting from time lapse movies with wild type and *xit* embryos expressing E-Cad-GFP. (B) Mean of the increased distance between two 3x vertices in both ends of individual junctions after UV-laser cutting. Error bars indicate confidence intervals of the standard error of the mean. (C) The scatter diagram of initial recoil velocity after laser cutting, related with the blue region in (B). Horizontal lines from up to down, second quartiles, mean, third quartiles. $N = 8$ (wild type), 5 (*xit*). The genotypes are indicated. The P values are calculated from paired Student's t -tests.

In collaboration with Dr. Lars Reichl, we analyzed the pulsing periodicity of AS cell fluctuation. As reported previously (Blanchard et al., 2010; David et al., 2010; Solon et al., 2009), we observed robust fluctuations of AS cell surface area with periods 2-3 min driven by actomyosin network contractility (Figure 3.26). In contrast, cell oscillations are faster and with lower amplitude in *xit* embryos. We observed short pulsing periodicity (Figure 3.26) and decreased area variance (Figure 3.23C) of cell fluctuations in *xit* embryos. As the E-Cad/F-actin interaction is assumed to be affected in *xit* embryos, the actin-myosin network fails to generate the efficient cell contraction and the cells start to relax already during cell fluctuation. The output of such a system for cell fluctuation should be high frequency and low amplitude.

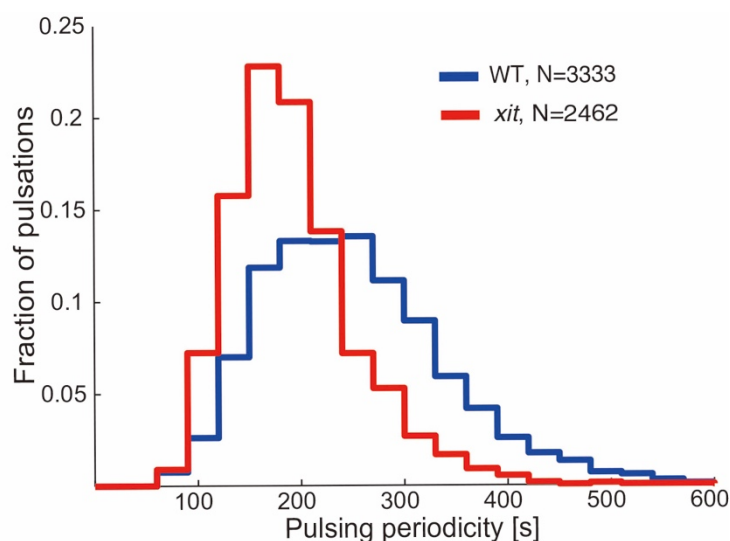


Figure 3.26 Amnioserosa cell oscillation period is reduced in *xit* mutants.

Histograms of pulsation periods in wild type and *xit* AS cells. AS cells from *xit* embryos exhibit pulsations of a substantially reduced period.

3.9 Summary

In this part of my thesis, I characterized the phenotypes of *xit* mutants in detail and confirmed the assumed function of Xit as glucosyl-transferase in the ER. Germ-band extension and cell intercalation are affected in *xit* embryos, similar to the phenotypes in E-Cad RNAi embryos. I next focused on E-Cad as a potential target of *xit* and characterized the function of N-glycosylation modulation for E-Cad. I found that E-Cad

is hypo-N-glycosylated in *xit* embryos. The total amount of E-Cad protein was not affected by *xit*. Hypo-N-glycosylation did not disturb the cell adhesion function of E-Cad, however, it affected proper distribution of E-Cad along adherens junctions, E-Cad clusters dynamics, and adhesion tension generation. Using the AS system, I revealed that *xit* led to affected interaction between adherens junctions and F-actin cytoskeleton, and perturbed the mechanical signal coupling in neighboring cells consequently.

CHAPTER 4. Cell-cell coordination drives neighbor exchanges during epithelial tissue morphogenesis

The results of this part of my thesis were carried out as a collaborative work with Dr. Lars Reichl and Prof. Dr. Fred Wolf (Max Planck Institute for Dynamics and Self-organization). Prof. Dr. Jörg Großhans and Prof. Dr. Fred Wolf guided the project. I performed the experiments and data analysis of the first part (4.1), except the area variance analysis which was performed by Adam Saglem as a bachelor student. For the other parts, I performed all the biological experiments, and time lapsed images recording. Dr. Lars Reichl performed all the computational analysis.

Cell intercalation drives germ-band extension by local neighbor exchange (Figure 1.3) (Irvine and Wieschaus, 1994). The key to neighbor exchanges in epithelial tissue is junction remodeling. The topological T1 transitions are used as a model (Weaire and Rivier, 1984). T1 transitions consist of two phases within cell quadruplets: (1) collapse of a junction in vertical orientation with fusion of two 3x vertices into a single 4x vertex, (2) expansion of a new junction in perpendicular horizontal orientation by splitting of the 4x vertex into two 3x vertices (Figure 1.3C). In the lateral epidermis, the initial collapse concerns junctions in dorsal-ventral orientation (vertical) and new junctions expand in the anterior-posterior direction (horizontal) (Bertet et al., 2004). The anterior (A) and posterior (P) cells are the old neighbors, whereas the dorsal (D) and ventral (V) cells are the new neighbors (Figure 4.1). In following, A and P cells are also called old neighbors, and D and V cells are called new neighbors. In this part of my thesis, I focused on the extension phase of T1 transition within cell quadruplets and investigated the driven force of new junction formation.

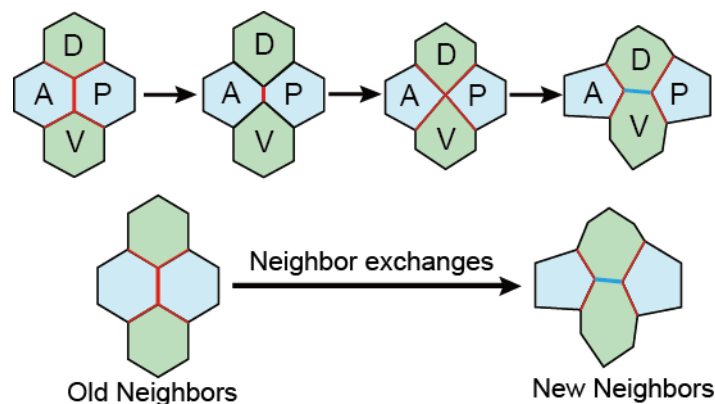


Figure 4.1 Schematic representation of T1 transitions.

Scheme of T1 transition (top pane). A, anterior, P, posterior, D, dorsal and V, ventral cells. Neighbor exchanges during T1 (bottom pane). Anterior (A) and posterior (P) cells are the old neighbors, whereas, dorsal (D) and ventral (V) cells are the new neighbors.

4.1 Simultaneous contraction of cardinal cells induces junction extension

Apical cell area oscillation is required for cell intercalation, driven by actomyosin contractility (Fernandez-Gonzalez and Zallen, 2011; Sawyer et al., 2011). Recently, it has been reported that formation and extension of the new junctions apparently require pulsed contractions of cortical-medial actomyosin clusters (Figure 1.4) and Rho-kinase in the old neighbors (Collinet et al., 2015; Yu and Fernandez-Gonzalez, 2016). I asked whether the cell-autonomous contractions in old neighbors were sufficient for the new cell junction formation. To address this question, I developed an optochemical method to induce apical cell contraction at single cell resolution during the T1 transition by Ca^{2+} uncaging (Figure 4.3B) (see *chapter 6*).

4.1.1 Simultaneous contraction of cardinal cells induces junction extension in wild type embryos

In wild type gastrulating embryos, in which the cell outlines were visualized by E-Cad-GFP, I first induced cell contraction in A and P cells synchronously at 4x vertices phase during the T1 transition and checked the dynamics of new junctions. As predicted, the new junction formation and extension was not impaired (Figure 4.2A, movie 4.1). It

indicates that the optochemical method is compatible with this process. I next applied the same protocol in D and V cells at 4x vertex phase to investigate whether synchronous apical contraction is sufficient for junction extension in dorsal-ventral orientation by inducing contraction in D and V cells. Consistent with the recent report (Yu and Fernandez-Gonzalez, 2016), new dorsal-ventral orientated junctions were extended artificially after its collapse. In this case the synchronous D and V cell contraction were induced (Figure 4.2B, movie 4.2). However, new dorsal-ventral orientated junctions failed to form when I introduced a time lag of 3 min between cell contractions in V and D cells (Figure 4.2C, movie 4.3). Taken together, my data is consistent with the model that local cell contraction promote and orient the extension of new cell-cell interfaces. Importantly, these experiments indicate that contraction of cardinal cells has to be synchronous within cell quadruplets for successful junction extension.

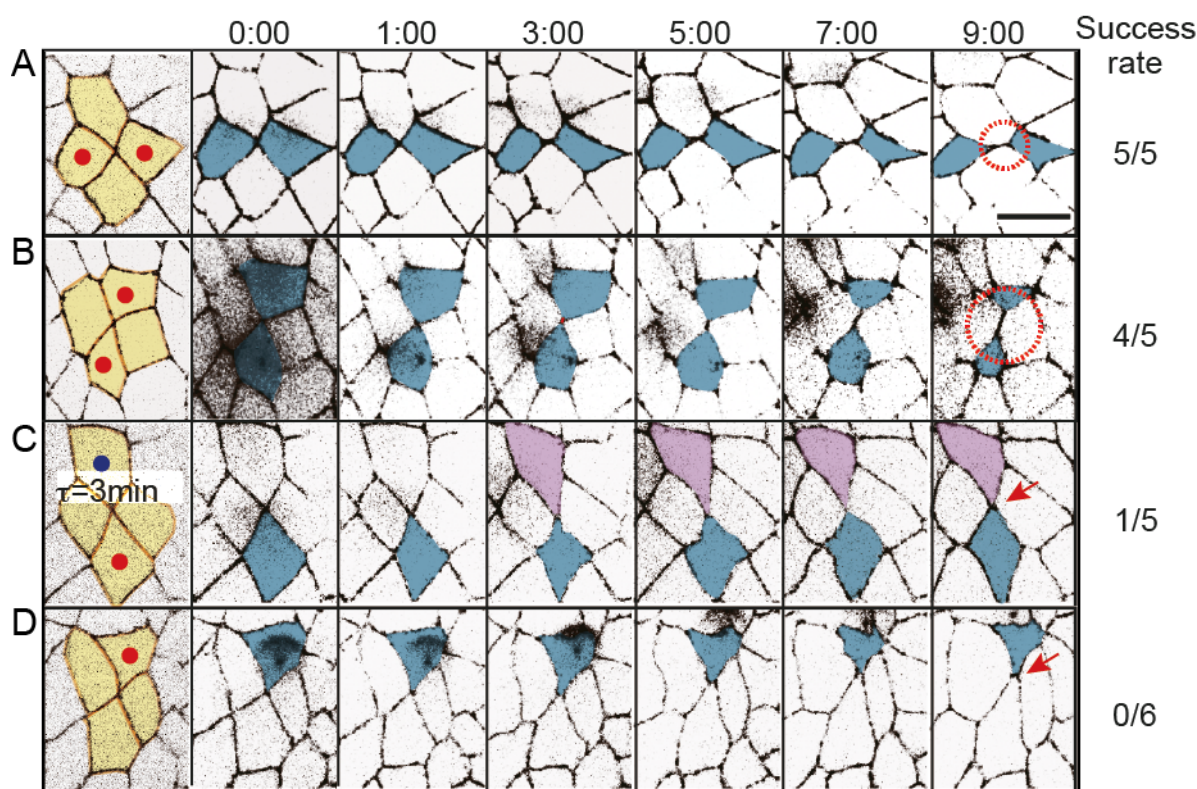


Figure 4.2 Ca^{2+} uncaging in cell quadruplets undergoing T1 transitions in wild type embryos.

Images from time lapse recording of Ca^{2+} uncaging experiments in wild type embryos, inducing cell contraction in cell quadruplets undergoing T1 transitions at 4x vertices (related with Figure A1-A4 in *Appendix*). Cell

junctions were labeled with E-Cad-GFP. Synchronous cell contractions in A and P cells (A), D and V cells (B). Asynchronous cell contractions in D and V cells with 3 min gap (C). Cell contraction in D cell (D). The cell quadruplets are highlighted with yellow, and red or blue dots indicate target cells. Contracting cells are highlighted with blue and purple, red dash circles indicate extended junctions, red arrows indicate 4x vertices. Success rate indicates the rate of DV junction (A and D) and AP junction (B and C) extension. 0:00, minute: second. Scale bars, 10 μm .

The new junction formation and extension failed when the apical actomyosin structures were destroyed by UV-laser in the new neighbors (Yu and Fernandez-Gonzalez, 2016). Thus, I asked whether the synchronous AP or DV cell contractions are sufficient to promote directional cell contact formation, or coordination within cell quadruplets is involved in junction extension. Then I performed the Ca^{2+} uncaging (see *chapter 6*) to induce cell contraction in D cell at 4x vertex phase (Figure 4.2D, movie 4.4). I found that new junction formation is inhibited by D cell contraction in all multiple experiments from different embryos. These results suggest that coordination within cell quadruplets is required for new cell-cell contact formation during T1.

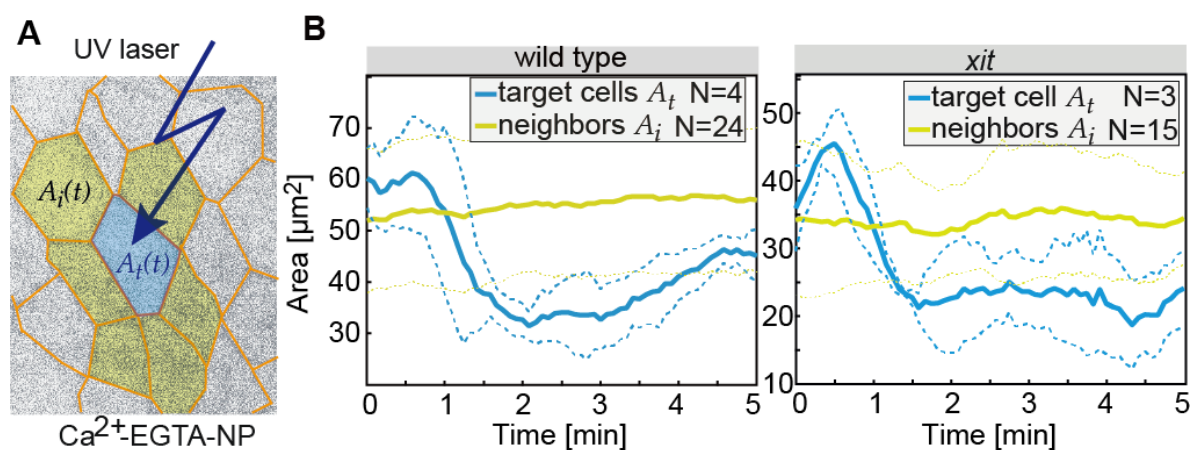


Figure 4.3 Cell contraction by Ca^{2+} uncaging.

(A) Scheme for Ca^{2+} uncaging in single cell. The target cell is highlighted with blue and neighbors are yellow. (B) Comparable cell contractions were induced in wild type and *xit* gastrulating embryos. Mean of target cell (blue curves) and neighboring cells (yellow curves) cross-section area after Ca^{2+} uncaging. Dash lines indicate confidence intervals of the standard error of the mean.

4.1.2 *xit* dependent cell-cell coordination

The new junction formation was affected in *xit* embryos (Y. Zhang et al., 2014). I next asked whether induced local cell contractions in old neighbors can extend new cell-cell contacts during T1 transitions in *xit* embryos. I induced cell contractions in cell quadruplets at 4x vertex phase. Synchronous A and P cells contractions and either A or P cell contractions failed to resolve 4x vertex within 5 minutes, although the cells contracted comparably to cells in wild type embryos (Figure 4.4).

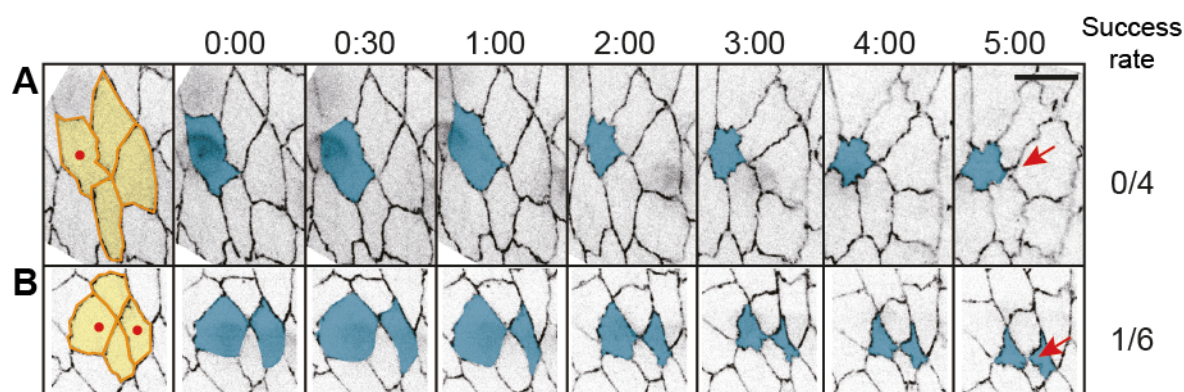


Figure 4.4 Ca^{2+} uncaging in cell quadruplets undergoing T1 transitions in *xit* embryos.

Images from time lapse recording of Ca^{2+} uncaging experiments in *xit* embryos, inducing cell contraction in cell quadruplets undergoing T1 transitions at 4x vertices (related with Figure A5 and A6 in *Appendix*). Cell junctions were labeled with E-Cad-GFP. (A) Synchronous cell contractions in A and P cells. (B) Cell contraction in A cell. The cell quadruplets are highlighted with yellow, and red dots indicate target cells. Contracting cells are highlighted with blue. Red arrows indicate 4x vertices. Success rate indicates the rate of DV junction extension. 0:00, minute: second. Scale bars, 10 μm .

In *chapter 3*, it was already shown that the response of neighboring cells was affected in AS in *xit* embryos (Figure 3.24). Using the Ca^{2+} uncaging, I got the consistent results from the lateral epidermal cell in gastrulating *xit* embryos, in which the cell outlines were visualized by E-Cad-GFP (Figure 4.5). I induced the contraction in single cell via performing Ca^{2+} uncaging and traced behaviors of the neighbors as well as some other cells as control by cross sectional areas measurement (Figure 4.5B). The control cells were at least 5 cells away from the contracting cell in the same embryo being recorded (Figure 4.5A). I observed a cross sectional areas increase in some neighbors

of target cells in wild type embryos (Figure 4.3, 4.5B). Area variance analysis showed that the area variance increased significantly in neighboring cells than in control cells in wild type embryos, indicating larger changes in area of neighbors than control cells during target cells contraction (Figure 4.5C). These data suggest the neighbors actively respond to for target cell contraction and that mechanism of coordination exist. In parallel, I performed the same experiments to wild type in gastrulating *xit* embryos. The target cell contraction was induced comparably as in wild type embryos (Figure 4.3). In contrast, I did not observe any increase of the areas of target cell's neighbors in 5 minutes (Figure 4.3, 4.5B). The area variance analysis showed the comparable results in neighbor and control cells (Figure 4.5C).

Taken together, the data suggest the intercellular coupling coordination occurs in the lateral epidermal cells during germ-band extension, as reported in the ventral epidermal cells during ventral furrow formation (Xie and Martin, 2015). This cell-cell coordination is affected in *xit* embryos. The comparison of wild type and *xit* rules out the option that the response is a geometrically effect due to preservation of total surface area.

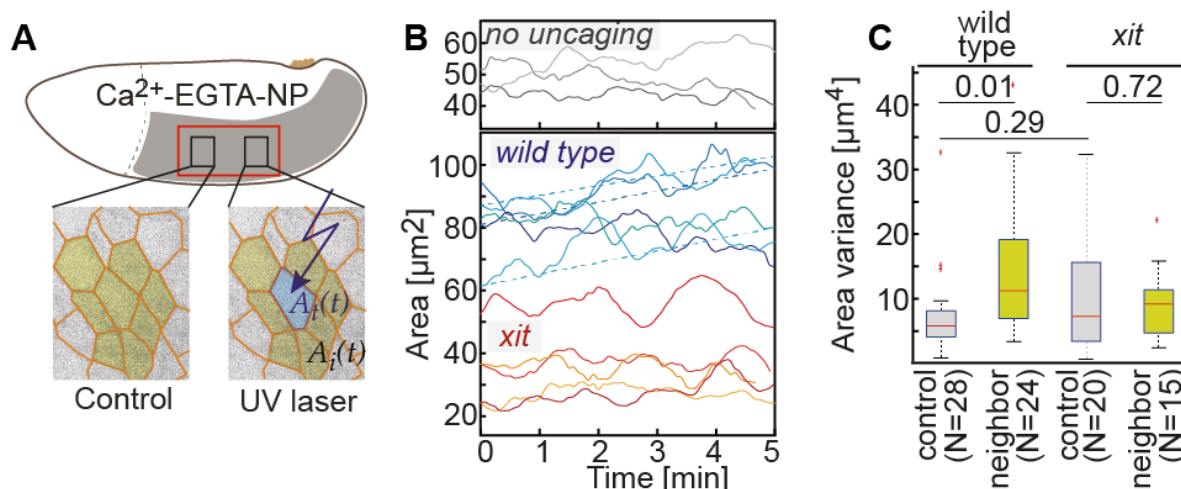


Figure 4.5 Response of neighboring cells depends on *xit* in germ-band epithelial cells.

(A) Scheme for Ca^{2+} uncaging in germ-band cells in the gastrulating embryos. Cell borders were labeled with E-Cad-GFP. (B) Single cell area tracking of no- Ca^{2+} uncaging, neighbors of target cells in wild type and *xit* embryos. (C) Boxplots show the area variance of control cells and neighbors of target cells, in wild type and *xit*

embryos. Red horizontal line, mean. Box, second and third quartiles. Black horizontal line with whisker, confidence interval. The P values are calculated from paired Student's t -tests.

In summary, during T1 in wild type embryos, synchronous cell contractions in D and V cells induce cell junction formation in D-V direction, and cell contraction in D or V cells inhibits the new A-P direction junction formation. Whereas, synchronous cell contractions in A and P cells failed to induce cell junction formation in A-P direction in *xit* embryos. The results suggest that local cell-autonomous contractions in the old neighbors are necessary but not sufficient for new cell junction formation. Thus, I put forward the hypothesis that *xit*-dependent cell-cell coordination in cell quadruplets is required for efficient neighbor exchange.

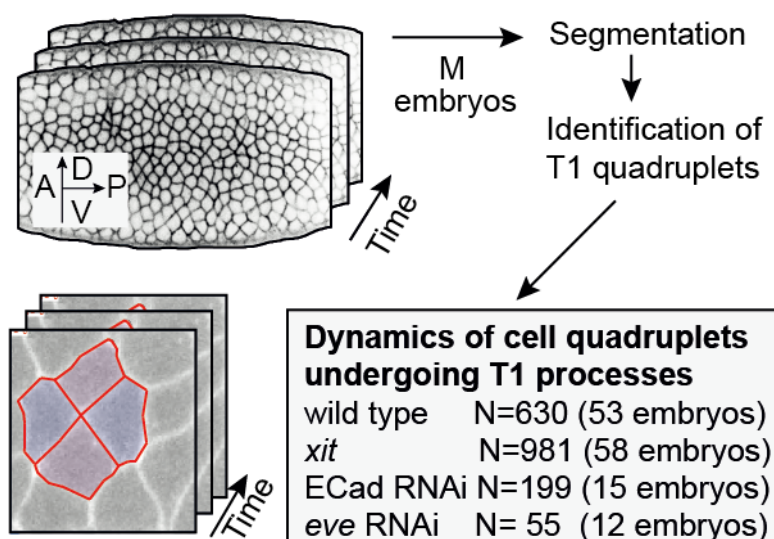


Figure 4.6 Schematic illustration of the overview of the data analysis.

Work flow of automatic image analysis and computational extraction of T1 transitions.

4.2 Temporal alignment of T1 transitions reveals long attempt phases and specific area dynamics in *xit* embryos

Cell contractions by Ca^{2+} uncaging were stronger than naturally occurring contractions. It is therefore a valid question, whether a coordination mechanism also drives normal neighbor exchange (T1process). We conducted a computational analysis of a large data set. The overview of experiments is shown in Figure 4.6. We recorded

time lapse movies from about 50 embryos in which the cell borders were visualized by GFP-resille and GFP-spider (Blankenship et al., 2006b). The images were segmented automatically. Cell quadruplets undergoing T1 were computational identified for the analysis. Large scale data sets of cell quadruplets were assembled from wild type (N=630), *xit* (N=981), E-Cad RNAi (N=199) and Eve RNAi (N=55) embryos respectively, each consisting of a movie with several minutes before and after 4x vertex stage.

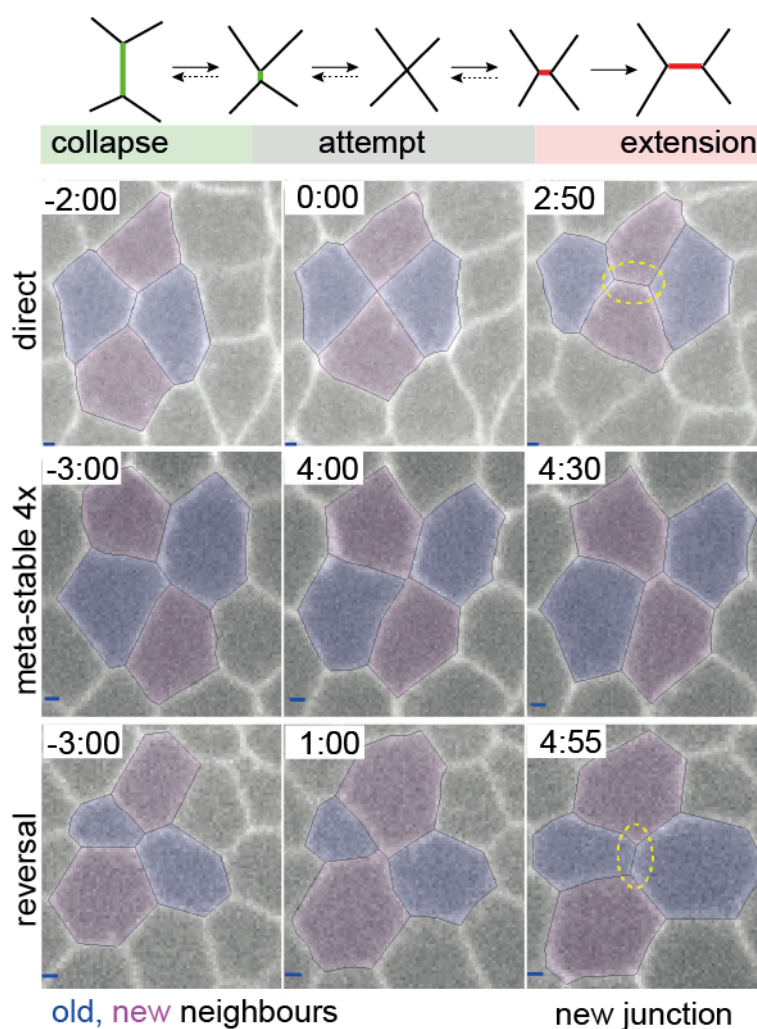


Figure 4.7 Diverse behaviors of cell quadruplets.

Examples of variant T1 transitions. Images from time lapse recordings of wild type embryos in which the cell borders are visualized by GFP tagged membrane proteins. Old and new neighbors are marked in blue and red respectively. The new junction is marked by a circle in yellow. 00:00, minute: second.

4.2.1 Diverse behaviors of cell quadruplets

The large data set of T1 process allowed us to conduct a statistical analysis. The diverse behaviors of cell quadruplets were revealed in wild type embryos (Figure 4.7). In addition to the straight forward T1 processes, we observed aborted T1 processes opening the 4x vertex in the same direction as the collapse. Numerous cell quadruplets

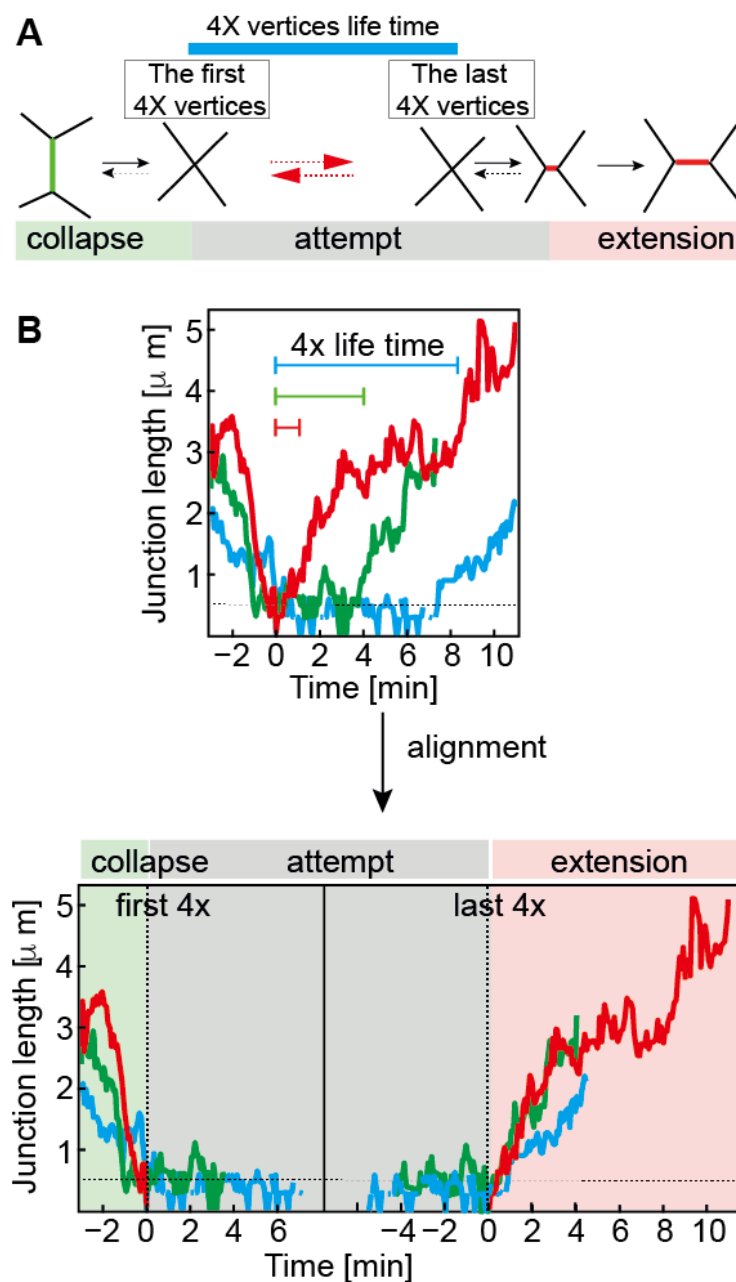


Figure 4.8 Alignment of T1 transitions.

(A) Schematic representation of fluctuation and life time of 4x vertices. (B) Illustration of temporal alignment of three exemplary T1 transitions.

showed fluctuations of 4x vertex during T1 as meta-stable 4x vertices, in which very short junctions formed and collapsed in DV or AP direction temporarily. Then meta-stable 4x vertices resolved finally after several minutes. For quantification, we temporal aligned all T1 processes to the time of the first and last 4x vertices. In this way, an ‘attempt’ phase was introduced between collapse (initial old junctions in D-V direction) and extension (stable new junctions in A-P direction) phases (Figure 4.8). With this alignment, the trajectories of the meta-stable 4x vertices are shown twice, following the first 4x and prior to the last 4x. The high variance of attempt phase deviation indicates that neighbor exchanges seem to have a strong stochastic component. With this alignment of T1 processes, the distribution of attempt phase cumulative sum is shown in Figure 4.9.

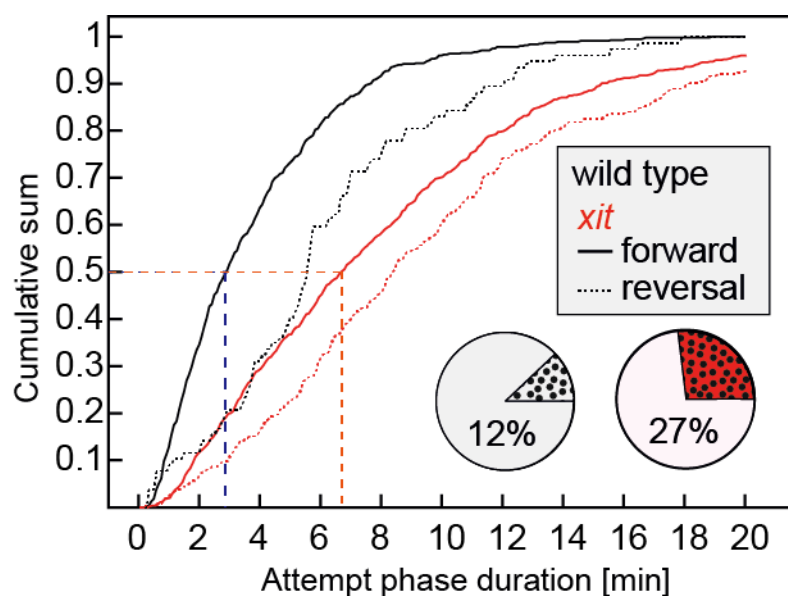


Figure 4.9 Prolonged attempt phase in *xit* mutants.

4x vertices have a prolonged attempt phase in *xit* mutants. Cumulative sum shows the distribution of 4x vertices attempt phase in wild type (black) and *xit* (red) embryos. Dash lines indicate the reversal cases that the new junction extended in D-V direction. Pie charts indicate the proportion of reversal cases in wild type (12%) and *xit* (27%) embryos.

Our quantitative image analysis showed that the reversal 4x vertices were more common in *xit* embryos (27%) than in wild type (12%) embryos (Figure 4.9). And the meta-stable cases were observed more frequently in *xit* embryos as well (Figure 4.9).

The 4x lifetime analysis showed that half of the 4x vertices were resolved successfully within 3 minutes in wild type embryos, whereas, it takes more than 7 minutes in *xit* embryos. Our data indicate that the prolonged attempt phase leads to the delayed cell intercalation in *xit* embryos. Furthermore, together with frequent reversal 4x vertices, prolonged attempt phase results in the observable germ-band extension phenotype in *xit* embryos.

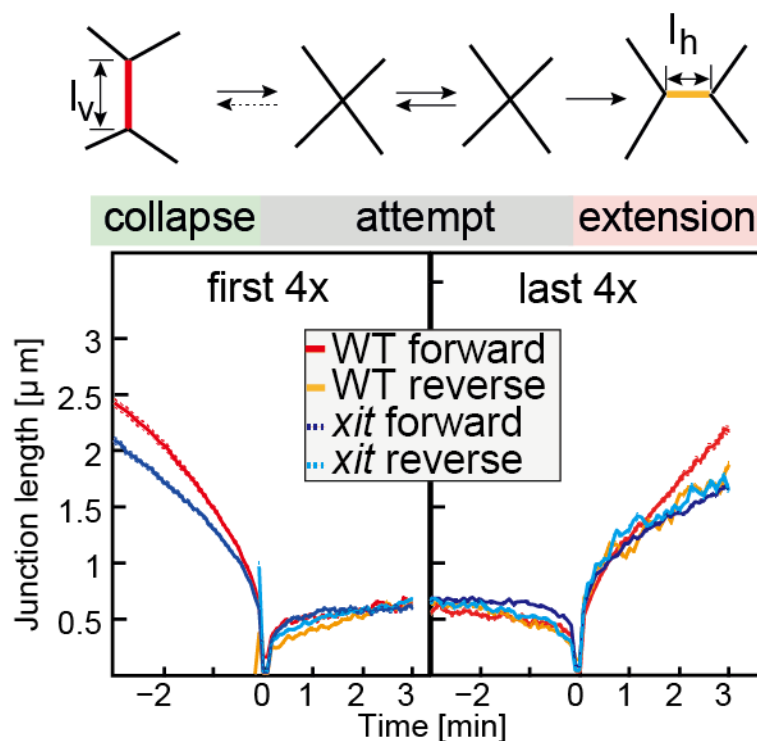


Figure 4.10 Averaged junction in cell quadruplets during T1 transitions.

Mean of junction lengths in cell quadruplets within T1s in wild type and *xit* embryos. The junction length was aligned with the first and last 4x vertex. The measurements are the length of AP junctions in collapse phase and the DV junctions in the extension phase.

4.2.2 Junction dynamics in cell quadruplets during T1

We next quantified junction dynamics in cell quadruplets during T1 (Figure 4.10). We applied the same temporal alignment with the first and last 4x vertex as before. In average, the dynamics of the collapse of AP cell contacts showed comparable but distinct behaviors in wild type and *xit* embryos. The kinetics showed the clear difference in DV junction collapse and extension in A-P and D-V directions, which indicates that

the junction extension is not the reversal case of junction collapse. Interestingly, the kinetics of new DV junctions in *xit* embryos was comparable to reversed AP junctions in wild type embryos.

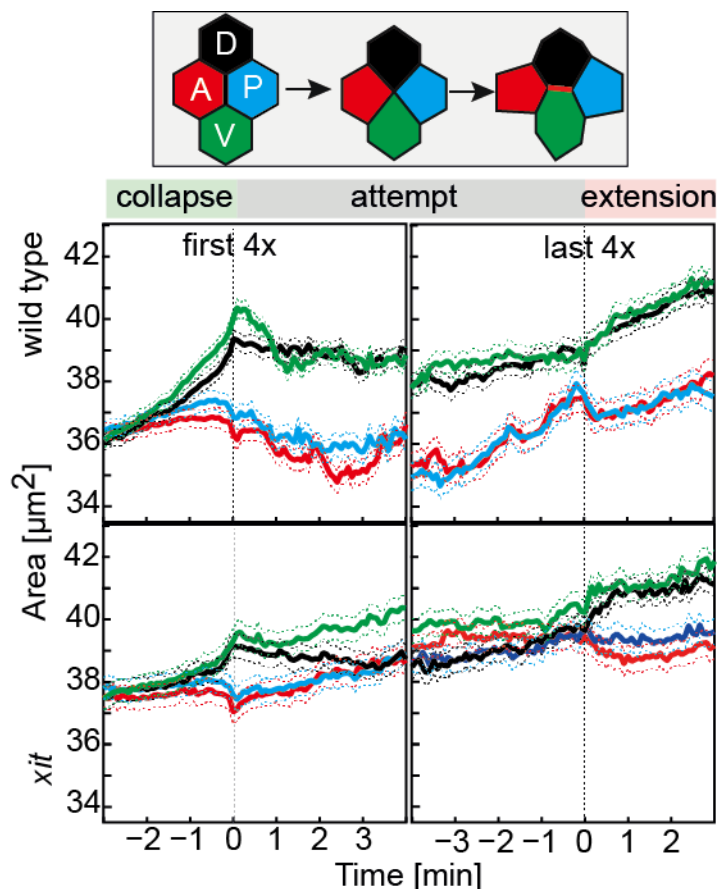


Figure 4.11 Averaged area dynamics in cell quadruplets during T1 transitions.

Mean of cross section areas in cell quadruplets within T1s in wild type and *xit* embryos. The averaged areas were aligned with the first and last 4x vertex. The areas from different cells by different colors, A, red, P, blue, D, black, and V, green. Dash lines indicate confidence intervals of the standard error of the mean.

4.2.3 Cell area dynamics in cell quadruplets during T1

We next quantified the cell cross-section area (cell area in the following) dynamics in cell quadruplets during T1 (Figure 4.11). In average, four cells showed the same cell area size initially. In 1 min before the first 4x vertex, the A and P (old neighbors) cell areas started to display the clear difference with D and V (new neighbors) cell areas and kept the clear difference in the attempt phase as well as extension phase in wild type

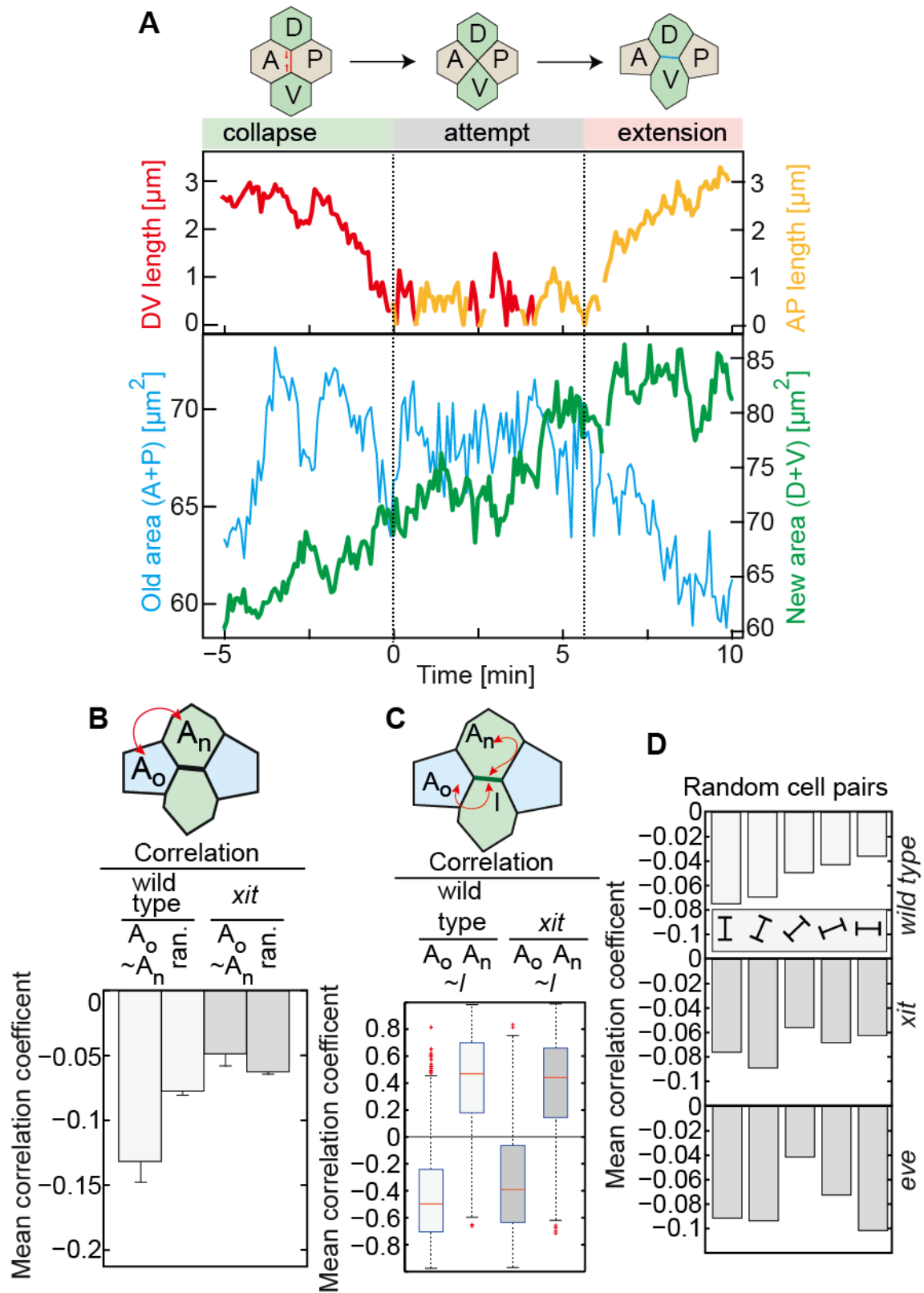


Figure 4.12 Correlated area change in cell quadruplets during T1 transitions.

(A) Exemplary time course of junction length and cell areas. (B) Correlation coefficients of area fluctuations between old and new neighbors in T1 cell quadruplets and random cell duplets in wild type and *xit* embryos averaged over three minutes after the first 4x vertex. N=2000 for random duplets. (C) The average correlation

coefficient in 3 minutes after the first 4x vertex between cell area and horizontal junction length within T1. The patterns are similar in wild type and *xit* mutant. (D) Dependence of area correlations in random cell duplets on junction orientation in wild type, *xit*, and Eve RNAi embryos.

embryos. The old neighbors were going to the contraction slightly, meanwhile, the new neighbors were going to the expansion. However, we did not observe the comparable cell area dynamics in *xit* embryos. The differences between old and new neighbors in average cell size were quite small, especially in the attempt phase. Old neighbors also contracted but in a less prominent and less synchronous manner.

In summary, the analysis of averaged junctional and area dynamics revealed stereotypical patterns and differences between wild type and *xit* embryos with the expansion of new neighbors as a prominent feature during collapse and extension phase. As an obvious difference between wild type and *xit* embryos, we identified the loss of average area difference during the attempt phase and the synchronous contraction at the onset of the extension phase. Based on this and the prolonged attempt phase in *xit* embryos, we hypothesize that coordination of old and new neighbors is important for successful junction extension.

4.3 T1 specific coordinated area fluctuations between old and new neighbors

The analysis of averaged quadruplets revealed that the old neighbors contracted during the last minute of the collapse phase and during onset of the extension phase. The new neighbors expanded during the T1. We next analyzed the individual quadruplets. Traces of old and new neighbor areas showed signs an anti-phasic pattern during T1 transitions. We analyzed the correlation coefficient of the changes in the area of old (A, P) and new (D, V) neighbors and junction length in individual quadruplets (Figure 4.12A). The correlation was averaged between the two area traces over a period of 3 min after the first 4x vertex. This revealed a correlation coefficient of about 0.13. In comparison, we calculated a correlation of less than 0.08 between area traces of random

cell duplets in wild type, about 0.05 in quadruplets and about 0.06 in random cell duplets of *xit* embryos (Figure 4.12B). Consistent with the previous reports (Collinet et al., 2015; Yu and Fernandez-Gonzalez, 2016), the area of old neighbors is anti-correlated with the new junction extension. Furthermore, we revealed that the area of new neighbors correlated with the new junction extension (Figure 4.12C). In contrast, the correlation between area changes and junction length was detected in *xit* embryos as well, suggesting that this correlation is due to geometrical constraints. Thus, we detected a T1 specific and *xit*-dependent cell-cell coordination mechanism, which may drive efficient resolution of 4x vertex.

The coordinated area fluctuations within random cell duplets analysis revealed that the area correlation is dependent on the junction angle of the duplets (Figure 4.12D). The Mean correlation coefficient showed polarity with the junction angle in wild type embryos, whereas, the polarity was broken in *xit* embryos, as well as in *eve* RNAi embryos which are largely devoid of planar polarization. These data indicate that also in random cell duplets, *xit*-dependent mechanisms exist that coordinates area fluctuations in a manner dependent on planar polarity.

4.4 Time-resolved correlation analysis reveals 4x vertex specific

Our large-scale data sets allow a time resolved correlation analysis. We correlated the ensemble of trajectories of old neighbors with that of new neighbors. Via a time-lag introduction into the correlation analysis, the time-resolved correlation analysis was realized (Figure 4.13). All six cell pairs of a quadruplet and averaged 4 anti-correlated and 2 correlated pairs were performed. Two-dimensional cross-correlation function of the time-dependent correlations showed a trace of negative correlations along the diagonal (Figure 4.13B). The strongest negative correlations were observed at the time of the first and last 4x vertex. Conversely, the positively coupled pairs (AP, DV) had the strongest correlation during the attempt phase, when the negatively coupled pairs were close to zero. These features of 4x vertex-specific and attempt phase-specific

correlations of area fluctuations were not detected in *xit* embryos. The time courses of anti-correlated and correlated pairs remained flat and close to zero during collapse and attempt phase. When aligned to successful extension events (last 4x vertex), a negative peak was detected in *xit* embryos similar to wild type. This indicates that when correlated area fluctuations in old and new neighbors occurred, junction extension was successful also in *xit* embryos. These data support the model that *xit*-dependent processes mediate efficient coordination of area fluctuations, which is important for timely resolution of 4x vertices and junction extension.

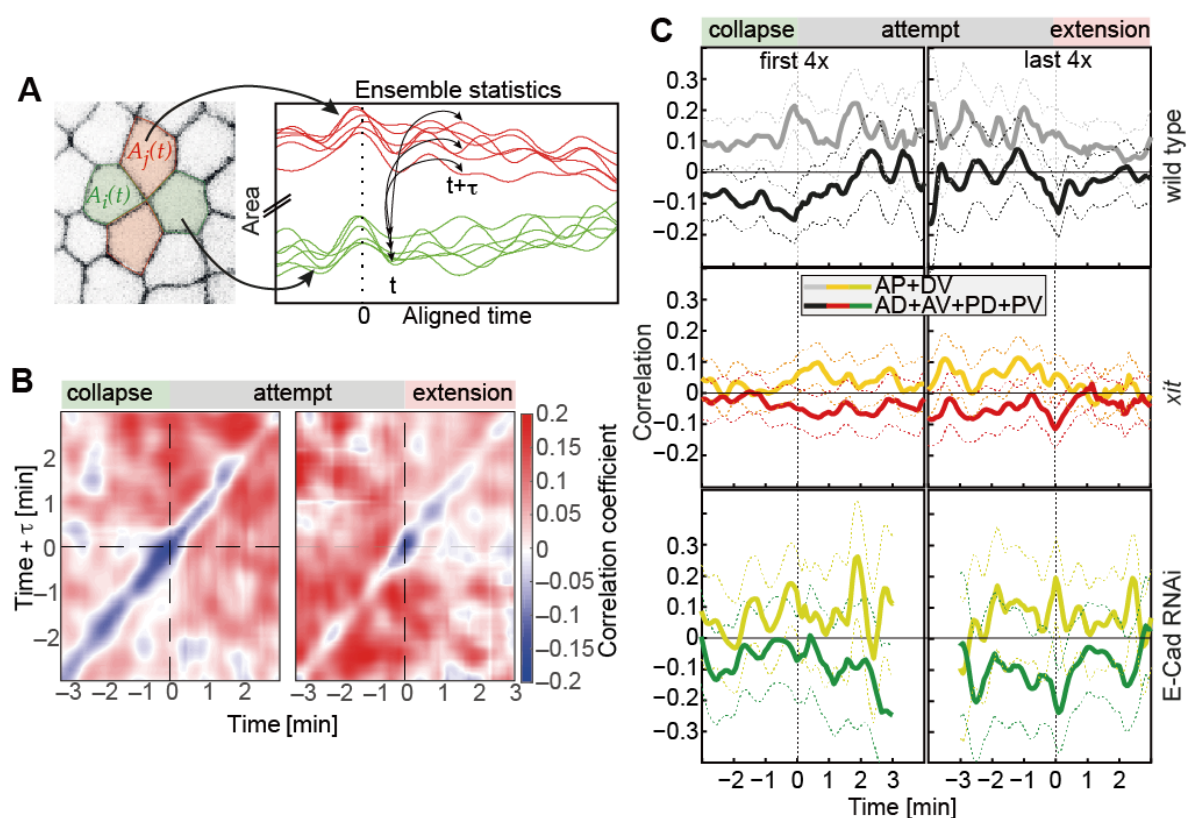


Figure 4.13 Cell coordination depends on Xit and E-Cadherin.

(A) Illustration of ensemble statistics. Schematic drawing of area trajectories of old (green) and new (red) neighbors. (B) Time-resolved correlation maps with the time lag between the old and new neighbor ensembles on the y axis. Correlation is indicated by the color scale. (C) Time-resolved correlation of area fluctuations with confidence intervals for anti-correlated and correlated pairs in wild type, *xit*, and E-Cad RNAi embryos.

4.5 E-Cadherin is involved in coordination

The same computational analysis was performed in the E-Cad RNAi embryos. This analysis revealed results similar to *xit* embryos. In E-Cad RNAi embryos, we observed a high proportion (28%) of aborted T1 transitions and a prolonged attempt phase (Figure 4.14). Furthermore, the correlations of area fluctuations within individual cell quadruplets did not show a specific correlation during the first 4x vertex (Figure 4.13C). In contrast, a negative peak was revealed when aligned to the last 4x vertex. Similar to *xit* embryos, a successful junction extension only occurred when area fluctuations in old and new neighbors were anti-correlated (Figure 4.13C). The lack of coordination in area fluctuations but its presence in successful cell rearrangements indicates that E-Cad is involved in driving timely resolution of 4x vertices and junction extension.

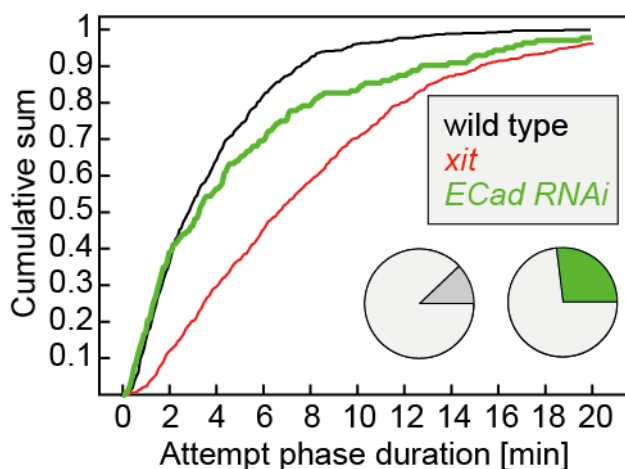


Figure 4.14 Prolonged attempt phase in E-Cadherin RNAi embryos.

4x vertices have a prolonged attempt phase in E-Cad RNAi embryos. Cumulative sum shows the distribution of 4x vertices attempt phase in wild type (black), *xit* (red), and E-Cad RNAi (green) embryos. Pie charts indicate the proportion of reversal cases in wild type (12%) and E-Cad RNAi (28%) embryos.

CHAPTER 5. DISCUSSION

5.1 Role of N-Glycans in E-Cadherin distribution in *Drosophila* embryos.

The last step of the lipid linked oligosaccharide (LLO) biosynthesis in ER is adding the three terminal glucose residues to form the mature LLO in eukaryotic cells (Figure 5.1) (Harada et al., 2015). This process is catalyzed by enzymes ALG5, ALG6, ALG8, and ALG10 in yeast (Aebi, 2013) as well as in mammalian cells (Harada et al., 2015). Afterwards, the mature LLOs as the glycans donor, the glycans are transferred to the asparagine residues of polypeptide chains by the oligosaccharyltransferase (OST) (Figure 5.1). It has been reported that *wol* and *gny* are the homologs of *alg5* and *alg6* respectively in *Drosophila* (Figure 5.1) (Haecker et al., 2008; Shaik et al., 2011).

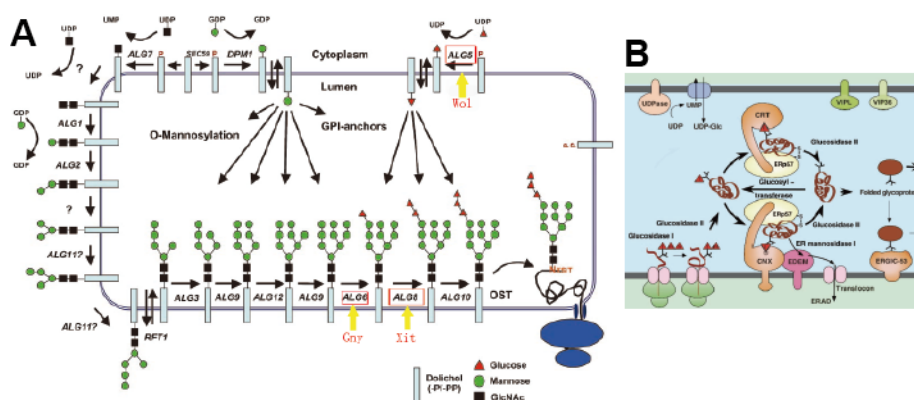


Figure 5.1 ER N-glycosylation and quality control (Helenius and Aebi, 2004).

(A) N-glycosylation enzymes (Alg5, Alg6 and Alg8) are localized in ER membranes. Their function is to transfer the glucose to the tip of the glycan. The enzyme OST transfer the mature oligosaccharide from the lipid-bond precursor to the newly synthesized protein. (B) During the folding process, three glucoses are removed consecutively. Correctly folded proteins could pass the quality control and move forward to golgi and plasma membrane.

My colleague and I identified *xit* as the homolog of *alg8*. As E-Cad was identified as a glycoprotein in *Drosophila* (Oda et al., 1993), I assumed that E-Cad N-glycosylation may be affected in this mutant embryo. As predicted, E-Cad is showing hypo-glycosylated (Figure 5.2). This is consistent with the report in yeast or the human, in which, the *alg5*, *alg6* and, *alg8* mutations lead to the hypo-glycosylation of secreted

proteins (Heesen et al., 1994; Imbach et al., 1999; Reiss et al., 1996; Stagljar et al., 1994b). It supports the same understanding in *Drosophila* as well, which non-glucose oligosaccharides can be transferred to proteins although the $\text{Glc}_3\text{Man}_9\text{GlcNAc}_2$ is the preferred substrate of the OST for N-linked glycosylation of proteins.

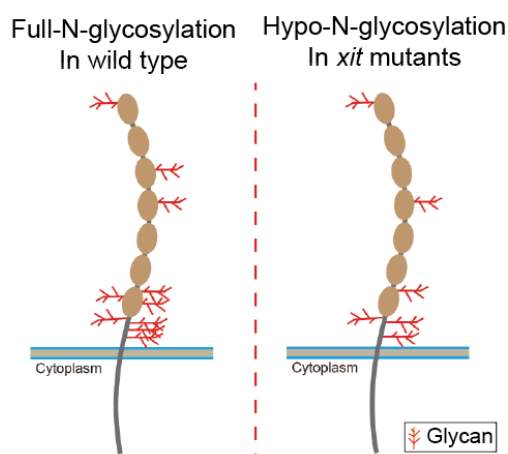


Figure 5.2 Schematic representation of E-Cadherin is hypo-N-glycosylated in *xit* mutants.

Drosophila E-Cad has 11 potential N-glycosylation sites (NetNGlyc 1.0 Server), as shown in red. 7 N-glycosylation sites were identified in mass spectrometry (Zielinska et al., 2012). E-Cad is hypo-N-glycosylated in *xit*.

N-glycosylation is supposed to be involved in the biogenesis of glycoproteins. The three terminal glucose residues have been revealed with the function for the glycoproteins quality control in the ER (Helenius and Aebi, 2004). In my case, the total E-Cad proteins amounts are comparable in wild type and *xit* mutants. It means that the hypo-glycosylated E-Cad is not degraded during its biogenesis. It suggests that at least the Full-N-glycosylation is not required for E-Cad biogenesis in *Drosophila* (Figure 5.3). This is consistent with the case in mammalian cells, in which, only N-Glycan at Asn 633, one of the four N-glycosylation sites, are essential for E-Cad folding, trafficking and its proper expression (Zhou et al., 2008). According to my results, I prefer a model that N-glycans are important for the distribution and clustering of E-Cad in the plasma membrane (Figure 5.3), as the accumulation and cluster formation of E-Cad at adherens junctions, which are the primary E-Cad structures detected in histology, are clearly

reduced in *xit* mutant embryos. The sub-apical enrichment of E-Cad is reduced and over-expressed E-Cad is uniformly distributed along the lateral membrane, which suggests that N-glycosylation is important for the E-Cad apical-basal polar distribution as well (Figure 5.3).

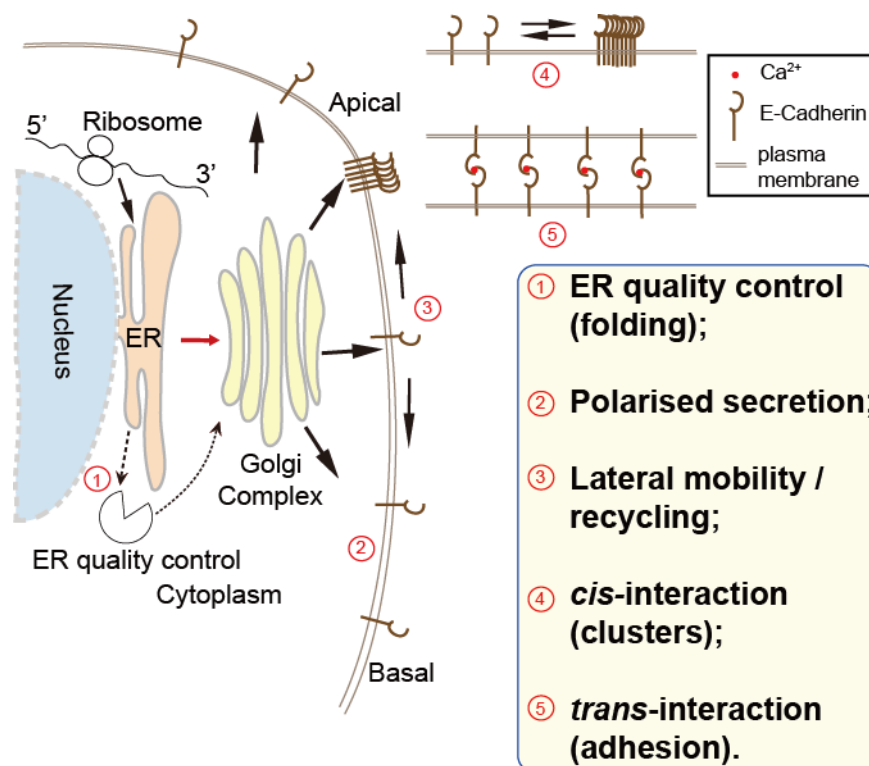


Figure 5.3 Role of N-Glycans in E-Cadherin localization and functions in *Drosophila* embryos.

Full-N-glycosylation of E-Cad is required for its proper distribution on the plasma membrane, apical-basal polar distribution, and *cis*-interaction. E-Cad ER quality control and *trans*-interaction do not require E-Cad full-N-glycosylation.

5.2 N-glycosylation alters the immobilization of E-Cadherin clusters and E-Cadherin-based mechanotransduction in *Drosophila* embryos.

E-Cad plays multiple roles in the epitheliums (Maître and Heisenberg, 2013). As an adhesion protein, it mechanically stabilizes the cell-cell contacts via generating the adherens junctions. E-Cad is a trans-membrane protein, forming the cadherin-catenin (α -catenin and β -catenin) complex via the cytoplasmic domain and interacting with F-actin cytoskeleton. In this way, E-Cad generates adhesion tension and plays a role in mechanotransduction between the neighboring cells. In addition to the genetic and/or

epigenetic level perturbations, a substantial body of evidences have revealed that operations at the post-translational level affect the functions of E-Cad as well, such as N-glycosylation (Pinho et al., 2011) and O-glycosylation (Lommel et al., 2013; Vester-Christensen et al., 2013).

In my case, the epithelial structures appear to be functional in *xit* mutant embryos. and the α -Catenin and Arm staining are comparable between wild type and mutant embryos. This clearly shows that the full N-glycosylation is not essential for the cell-cell contact and the function of adherens junctions.

The distribution of E-Cad on the plasma membrane is not uniform. E-Cad forms obvious super molecular clusters structure. It has been revealed that the cluster E-Cad is more stable than the uniform distributed E-Cad in *Drosophila* embryos (Cavey et al., 2008). Therefore, I focused on the clusters and discovered a developmental control of E-Cad cluster mobility by FRAP experiments. The E-Cad clusters are getting more stable during germ-band extension than before germ-band extension.

As E-Cad expressing levels are increasing during gastrulation, the consequence could be that 1) there are more cluster structures or/and 2) the cluster size is being enlarged during development. Using the super resolution microscope, it has been revealed that E-Cad cluster size is increased during gastrulation (Quang et al., 2013). In addition, the E-Cad/F-actin interaction is required for maintenance of E-Cad cluster (Quang et al., 2013). Furthermore, E-Cad clusters are constrained by the contractile actin network by a tethering mechanism (Matthieu Cavey, 2008). Evidence suggests that a consistent mechanism exists in cultured epithelial cells. Using 3D-STORM, it has been revealed that E-Cad clusters are delimited by cortical F-actin (Wu et al., 2015). It has been reported that local E-Cad recruitment and its immobilization are correlated with myosin II activity in suspended cell doublet, in which, actin turnover is decreased through a myosin II-driven modulation (Engl et al., 2014).

How does E-Cad link to actomyosin network in cell? Biochemical studies have revealed that α -catenin binds strongly to the E-Cad- β -catenin complex ($K_D \sim 1$ nM) (Pokutta et al., 2014; Yamada et al., 2005), but more weakly to the F-actin cytoskeleton ($K_D \sim 1$ μ M) (Rimm et al., 1995). Furthermore, in vitro binding of α -catenin to the cadherin cytoplasmic domain/ β -catenin complex further weakens the affinity of α -catenin for F-actin by at least 20-fold, and this weak binding could not support the force transmitting between E-Cad and the actin cytoskeleton (Borghetti et al., 2012; Yamada et al., 2005). Fortunately, this question has been addressed perfectly by a biochemical study recently (Buckley et al., 2014). This seminal work demonstrates that external force is required for the strong interaction between the minimal cadherin-catenin and F-actin. In cells, the force is originated from myosin II contractility. This force could also promote binding of vinculin via force-dependent conformational change of α -catenin (Yao et al., 2014), thereby creating a self-reinforcing system for strong linkage of the cadherin-catenin complex to the actin cytoskeleton. These in vitro data provide very valuable insight for understanding how the developmental control of E-Cad clusters mobility occurs in *Drosophila* gastrulating embryo.

Therefore, I suppose a model that the developmental control of E-Cad clusters mobility, i.e. the increasing of E-Cad cluster stability during germ-band extension, is due to the increasing myosin II activity during this developmental stage. Myosin II may recruit E-Cad locally to promote E-Cad clustering, maintain E-Cad cluster size via supporting E-Cad/actin interaction, and increase E-cad cluster immobilization. This hypothesis could be tested by performing the FRAP experiments in the embryos, in which the Myosin II activity is inhibited via Y-27632 injection for example.

By super resolution microscope and FRAP experiments, I have found that in *xit* mutants, the E-Cad clusters are smaller, more mobile than in wild type, which suggests full N-glycosylation for E-Cad is required for stable E-Cad cluster formation during germ-band extension. The comparable total protein amount in wild type and *xit* embryos rules out the lacking in E-Cad molecules is the reason of forming smaller and more mobile E-

Cad clusters. How does N-glycosylation affect the E-Cad cluster formation? Here I propose 3 possibilities:

1), the lack of N-glycosylation leads to the loss-of-phosphorylation of β -catenin, which affects the binding between E-Cad-catenin complex-actomyosin. Without the proper actin structure underneath the membrane, E-Cad cluster diffuses along the membrane more easily;

2), the big E-Cad clusters cannot form initially in *xit* mutant embryo due to lack of cis interaction mediated by N-glycosylation;

3), E-Cad *cis*-interaction could be affected by hypo-glycosylation, and E-Cad relative bigger cluster can be formed initially, but the increased myosin activity spits, instead of stabilize the cluster as in wild type.

In order to test the first possibility, an immunoprecipitation of E-Cad and catenin complex should be done in future. In laser cutting experiments, the initial recoil velocity in *xit* mutant was higher than in wild type, which implies the interaction between E-Cad and F-actin was affected in *xit* mutant. This may support the hypothesis that extracellular N-glycosylation of E-Cad is important for binding of F-actin in cytoplasm.

To separate the 2nd and 3rd possibility, I did FRAP experiments using the embryo injected myosin inhibitor Y-27632. E-Cad clusters mobility was decreased in *xit* embryos, in which the actomyosin contractility was inhibited slightly via lower concentration of Y-27632 (2 mM) injection. This result clearly rules out the 2nd possibility. Interestingly, its mobility did not show any decreases in *xit* embryos that the actomyosin contractility was inhibited strongly via high concentration of Y-27632 (5 mM) injection. It could be explained that the actomyosin contractility dependent E-Cad clustering is destroyed in this case. These data further support that the myosin II-dependent E-Cad clustering occurs in *xit* embryos initially.

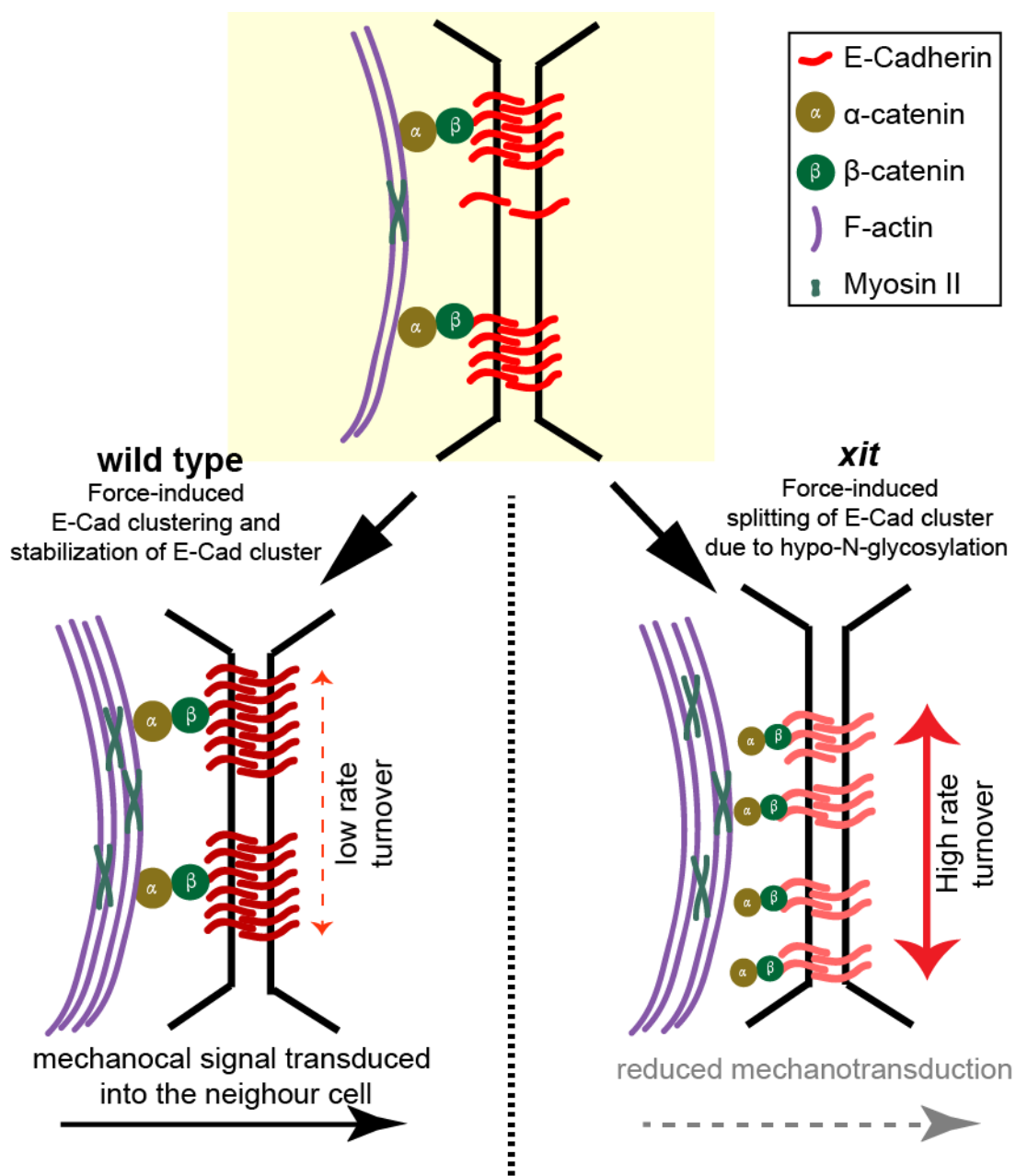


Figure 5.4 N-glycosylation alters the immobilization of E-Cadherin clusters and E-Cadherin-based mechanotransduction in *Drosophila* embryos.

E-Cad *cis*-interaction could be affected by hypo-N-glycosylation, and E-Cad relative bigger cluster can be formed initially, but the increased myosin activity splits, instead of stabilize the cluster as in wild type. The E-Cad-based mechanotransduction is affected consequently in *xit* embryos.

At the onset of germ-band extension, anisotropic tension along the A-P body axis leads to an A-P stretching of the lateral epidermal cells with a gradual increase towards the posterior tip of the embryos. Cell stretching is reduced when cell intercalation occurs, whereas the anisotropic tension is still detected (Collinet et al., 2015; Lye et al., 2015;

Sawyer et al., 2011). E-Cad and adherens junctions are supposed to be the keys in force transmission and coordination on a tissue wide scale via E-Cad-based mechanotransduction. With collaboration, we demonstrated that the mechanical signal coupling within neighboring cells was affected both in the lateral epidermal and AS cells in *xit* embryos. This suggests E-Cad cluster mobility /size and N-glycosylation is important for the proper functions of E-Cad molecules.

I suppose a model that the Full-N-glycosylation of E-Cad is required for its clustering, E-Cad/F-actin interaction, and E-Cad based mechanical signal coupling within neighboring cells during morphogenesis (Figure 5.4). As the CRISPR-based strategy has been successfully applied in *Drosophila* recently (X. Zhang et al., 2014), protein tags have been induced in the gene of E-cad (Pinheiro et al., 2017). The CRISPR-based strategy can be applied to introduce the point mutations at the glycosylation sites of E-Cad to further investigate the modulation of E-Cad function and dysfunction by glycosylation *in vivo*.

5.3 Coordinated cell behaviors are important for tissue extension

Cell intercalation occurs widely in the tissue deformation, such as in fly germ-band extension and in epithelial tubes, including the fly trachea, frog kidney, chick neural tube, and mouse cochlea (Walck-Shannon and Hardin, 2014). The local neighbor exchange is the key to drive cell intercalating by directional cell-cell contacts formation and extension. Using quantitative imaging, biophysical and pharmacological approaches, we demonstrate that coordinated cell area change within the cell quadruplets is the key to resolve the direction of new DV cell contacts assembly during *Drosophila* germ-band extension. And coordinated cell area change requires mechanical signal coupling within the cell quadruplets. We reveal a diverse behavior of quadruplets, and the fluctuations of 4x vertex during T1 transitions. We induced an “attempt” phase defined as the period between the first and last 4x vertex in addition to the collapse and extension phases.

I developed an optochemical method to induce cell contraction at single cell resolution during germ-band extension. Simultaneous contractions of two symmetric positional cells within cell quadruplets direct the cell junction assembly successfully. Contractions in one neighbor block the neighbor exchange at 4x vertex phase, however. By setting up a large-scale data analysis, we demonstrate that an anti-correlation for cell areas in old and new neighbors is detected during the A-P directional resolution of the 4x vertex. This anti-correlation is weakened significantly in *xit* and E-Cad RNAi embryos in which the neighbor exchange is affected by the prolonged attempt phase. Interestingly, when we only pick up the successful T1 cases in *xit* and E-Cad RNAi embryos, the comparable anti-correlation for cell areas in old and new neighbors is re-detected. The anti-correlation for cell areas in old and new neighbors means that cell contractions in old neighbors have to be simultaneous with the cell expansion in new neighbors. We find the mechanical signal coupling within the neighbors is affected in *xit* embryos, in which E-Cad is Hypo-N-glycosylated, thereby affects the E-Cad clustering and the E-Cad/F-actin interaction consequently. Consistently, simultaneous contractions of two symmetric positional cells within cell quadruplets fail to direct the cell junction assembly in *xit* embryos. Our data suggest that the local cell contractions in old neighbors are necessary but not sufficient to drive the directional new junction extension within T1. We suppose a model that the coordinated cell behaviors are the essential to drive the directional resolution of the 4x vertex in T1 transition (Figure 5.5). The simultaneous cell behaviors require the cell communications between the old and new neighbors within cell quadruplets.

The mechanisms of how does the mechanical signal regulate between old and new neighbors within the cell quadruplets remain unclear. The actomyosin contractility in the new neighbors is required for the new junction formation (Yu and Fernandez-Gonzalez, 2016). In this study, we found that the induced cell contractions in one of the new neighbors inhibited the new cell junction formation. It is likely that actomyosin in the new neighbors serves a different function than in the old neighbors, where contractility controls area changes. The adherens junctions were clearly affected in E-Cad RNAi but

not in *xit* embryos. And E-Cad protein amounts were reduced in E-Cad RNAi but not in *xit* embryos. We found the cell coordination was affected in both *xit* and E-Cad RNAi embryos. It suggests that *xit* and E-Cad RNAi effect the mechanotransduction in different manners.

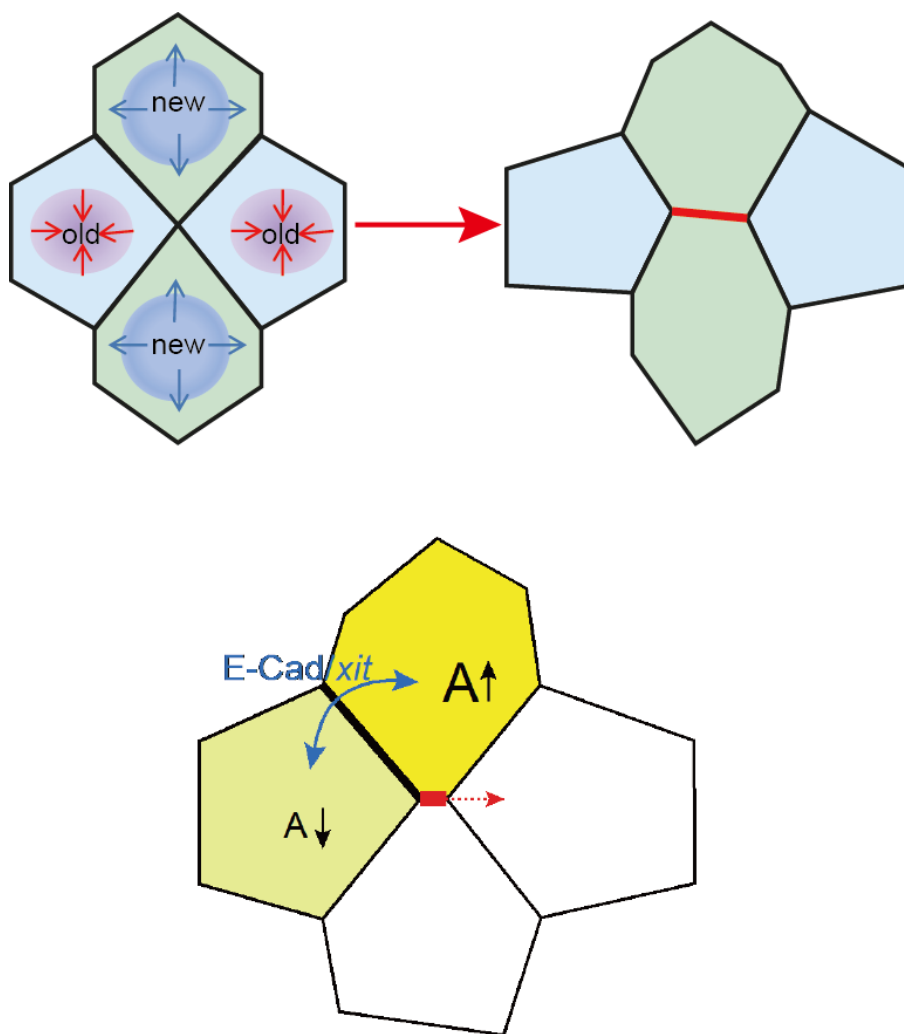


Figure 5.5 Coordinated cell area fluctuations drive expansion of new junctions during cell intercalation in *Drosophila* embryos.

The new junction formation is driven by the cell contractions in old neighbors and simultaneous cell expansion in new neighbors during neighbor exchange. These coordinated cell area fluctuations require Xit/E-Cad.

PART II

**Optochemical control of cell contractility at single
cell resolution in *Drosophila* embryos**

CHAPTER 6. Optochemical control of cell contractility at single cell resolution in *Drosophila* embryos

6.1 Introduction

Apical constriction of cells, driven by apical actomyosin contractility, plays a central role in tissue morphogenesis (Martin and Goldstein, 2014). The contractility of a cell and the resulting cell shape changes are linked to neighboring cells in epithelial tissue. A contractile cell mechanically pulls on its neighbors via adherens junctions and may elicit a specific response via E-Cad based mechano-transduction (Hoffman and Yap, 2015). The contractile activity is controlled autonomously but also influenced by neighboring cells. The mechanisms of mechano-transduction have been investigated by genetic approaches, such as knockouts, knockdowns, mutations and overexpression, revealing correlations without clearly defining causality. Experimental non-invasive interventions are needed, which either inhibit or induce cell contractility with single cell and sub-minute temporal resolution to resolve the causality in correlative relations.

The optogenetic approaches provide ability to control the cell contractility spatiotemporally, which are well-developed in recent years (Toettcher et al., 2011). Cell contractility can be inhibited by optically induced membrane recruitment of PI(4,5)P₂ leading to interference with phospho inositol metabolism and subsequent suppression of cortical actin polymerization (Guglielmi et al., 2015). As well studied, non-muscle myosin II is activated by the RhoA-Rho-kinase pathway in epithelial tissue (Etienne-Manneville and Hall, 2002). Recently, a method was reported for activation of contractility in cultured cells, which is based on light-induced activation of the RhoA pathway (Valon et al., 2017). Despite their well-established effectiveness, the genetically encoded light-sensitive proteins have to be expressed in the cells or organism, therefore this makes the application to be limited in the specific mutant backgrounds. Recently, laser ablation has emerged to perturb single cells by modulating cell contractility via activating wound healing process in the context of developing organisms (Yu and Fernandez-Gonzalez, 2016). However, laser ablation treatment is invasive, displays the poor reversibility and might lead to unwanted cytotoxic effects.

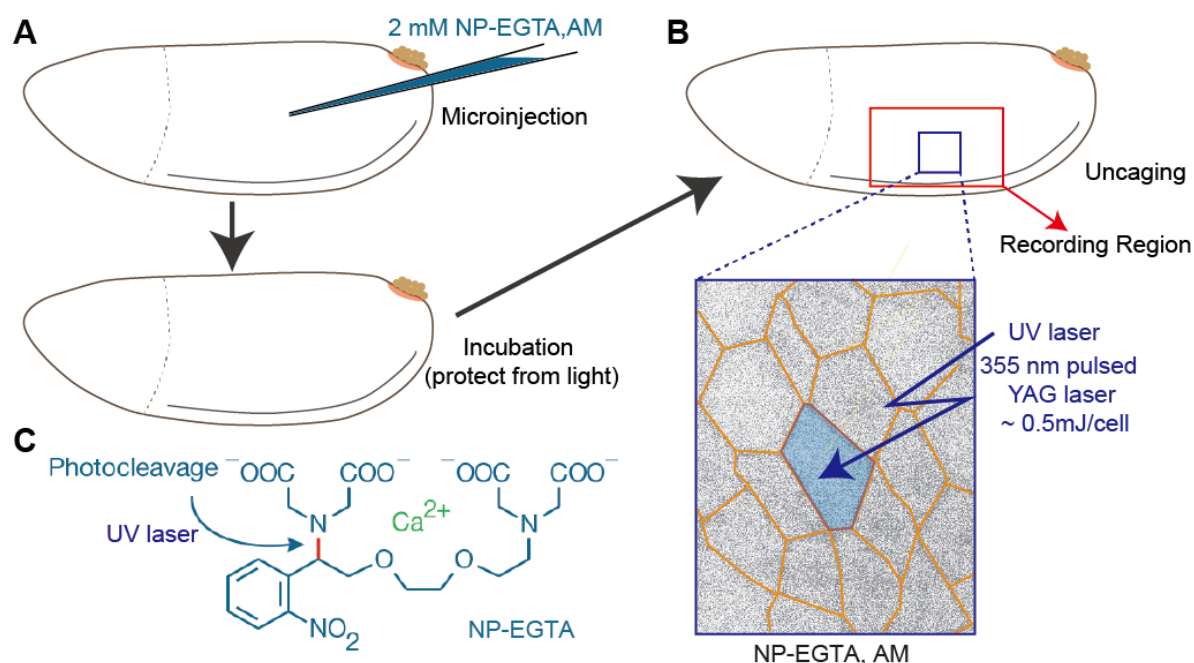


Figure 6.1 Scheme of Ca²⁺ uncaging in epidermal in *Drosophila* embryos.

(A) Schematics for the Ca²⁺ uncaging in *Drosophila* embryos. “NP-EGTA, AM” was injected into the staged embryos and the embryos were incubated for 10 minutes at room temperature protected from light. (B) Application of a UV laser through a second light path while cells are recorded through an imaging light path. Target cell is indicated in blue. (C) Structure of the cage compound, NP-EGTA complexes with Ca²⁺. Upon UV illumination, this complex is cleaved to yield free Ca²⁺ and two iminodiacetic acid photoproducts. The photo-labile bond is indicated in red.

In addition to the RhoA-Rho-kinase pathway, intracellular calcium ions (Ca²⁺) are required for apical contraction in cultured epithelial cells (Lee and Auersperg, 1980), neural tube closure (Lee and Nagele, 1986; Smedley and Stanisstreet, 1986) and folding morphogenesis of the neural plate (Ferreira and Hilfer, 1993). Global perturbation of intracellular Ca²⁺ impairs egg chamber elongation in *Drosophila* oogenesis. Myosin II contraction is activated by increased intracellular Ca²⁺ (He et al., 2010). More recently, evidence shows that Ca²⁺ are required for *Xenopus* neural tube, and apical constriction is induced by transient increase in Ca²⁺ concentration (M. Suzuki et al., 2017). Although the detailed molecular mechanism remains unclear, it has been proposed that intracellular Ca²⁺ contribute to the regulation of apical contraction. Optochemistry is an excellent technique to modulate intracellular ions concentration in high spatiotemporally manner by light sensitive ion channels and caged ions for example (Fehrentz et al., 2011). Here I report a simple and robust optochemical method to induce rapid and reversible cell contraction by increasing intracellular free Ca²⁺ with UV laser in single cell resolution during tissue morphogenesis in *Drosophila* embryos.

6.2 Results

6.2.1 Uncaging induces rapid Ca^{2+} concentration increase in epithelial cells in *Drosophila* embryos.

Ca^{2+} uncaging employing the photolabile Ca^{2+} chelator *o*-nitrophenyl EGTA (NP-EGTA) is widely used in neurobiology to modulate intracellular Ca^{2+} concentration (Burgalossi et al., 2012; Delaney and Shahrezaei, 2013). Ca^{2+} is released from the chelator by a high-energy pulse of UV light, which cleaves a bond within the chelator (Figure 6.1C) (Ellis-Davies and Kaplan, 1994). To modulate intracellular Ca^{2+} concentration, in this study I used the cell-permeant acetoxymethyl (AM) ester of NP-EGTA, which binds to Ca^{2+} once the AM esters are removed by intracellular esterases. An overview of the method is shown in Figure 4.1. To introduce the cage, I microinjected “NP-EGTA, AM” into staged embryos shortly before the experiment. Ca^{2+} was released by one or a few short pulses of a 355 nm laser directed to a single cell (Figure 1A and B). The light paths of the UV laser and the recording laser in the visible spectrum were controlled independently, which allows UV exposure during imaging of a Ca^{2+} sensor or cell behavior in the GFP or RFP channels, for example.

To assess whether my approach enables efficient release of intracellular Ca^{2+} ions rapidly, I first conducted uncaging in cells of the lateral epidermis of *Drosophila* embryos during gastrulation stage. These embryos expressed a membrane bound GCaMP6 (myristoylated variant of GCaMP6) Ca^{2+} sensor protein (Chen et al., 2013) were used to visualize changes of intracellular Ca^{2+} concentrations directly. As predicted, I observed a transient increase of myr-GCaMP6 fluorescence within seconds in the target cell after illuminating “NP-EGTA, AM” injection embryos with 355nm UV light pulses (Figure 6.2B, Supplementary movie 6.1), whereas there was no observable fluorescence change with the same treatment from the buffer injected control embryos (Figure 6.2a, Supplementary movie 6.1). Quantitative image analysis showed that a peak with a factor F/F_0 of about 4 after two seconds, and then the sensor fluorescence gradually decreased to initial levels within a few minutes (Figure 6.2C). Whereas, I did

not detect an increase of Ca^{2+} sensor fluorescence after UV exposure in control embryos (Figure 6.2C).

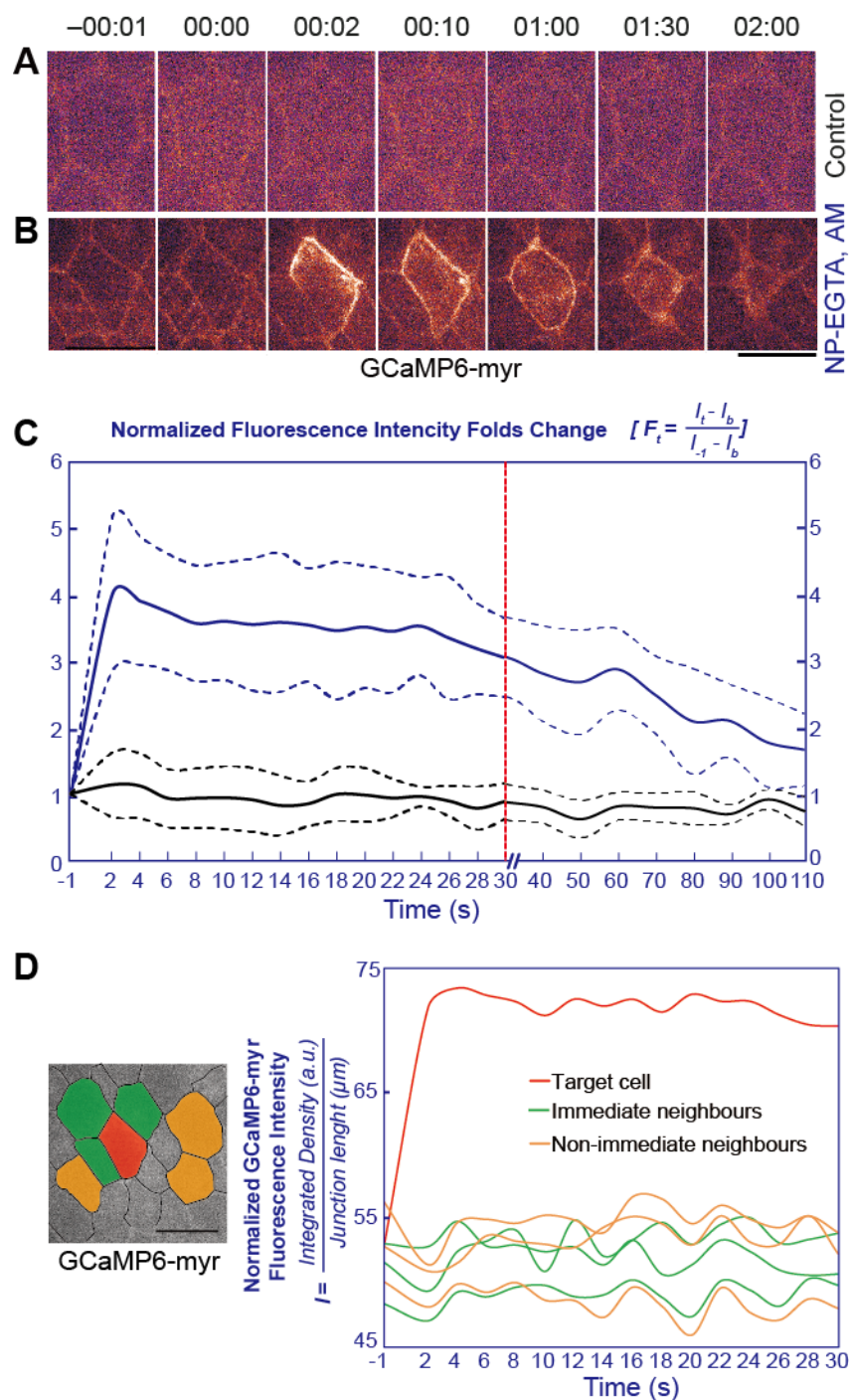


Figure 6.2 Uncaging induces rapid intracellular Ca^{2+} concentration increase in epithelial target cells.

(A, B) Images from time lapse recording with uncaging at $T=0:00$ in cells of the lateral epidermis in embryos (stage 7) expressing a membrane bound Ca^{2+} sensor (GCaMP6-myr). (A) Control embryo injected with buffer, (B) embryo injected with 2 mM “NP-EGTA, AM”, scale bar, 10 μm . (C) Mean of normalized GCaMP6-myr fluorescence intensity changes in folds. Control embryos (buffer injected, black), uncaging embryos (2 mM “NP-EGTA, AM” injected, blue). Fluorescence at $T=0\text{s}$ is not included due to bleed through of the UV light into the recording canal. The x coordinates represent time of uncaging. The y coordinates represent the

normalized GCaMP6-myr fluorescence intensities folds change over time after UV-laser illuminations compared with the initial fluorescence intensities 1 second before uncaging (T0). Dash lines indicate confidence intervals of standard deviation of mean (n=5 embryos in control and 3 embryos in “NP-EGTA, AM”). (D) Target cell (red), next neighbors (green), next-next neighbors (orange). Scale bar, 10 μm . Normalized GCaMP6-myr fluorescence intensities from a target cell, 3 immediate neighbors and 3 non-immediate neighbors. Fluorescence intensities were normalized to the junction length.

The increasing in Ca^{2+} sensor signal was restricted to the single target cell. (Figure 6.2B, Supplementary movie 6.1). Ca^{2+} sensor signal in the next neighbor cells and next-next neighbors of the target cell showed fluctuations, which did not change over time and were comparable to untreated or unexposed embryos (Figure 6.2D). In summary, these experiments have showed that Ca^{2+} uncaging can be applied to epithelial cells of *Drosophila* embryo, controlling intracellular Ca^{2+} levels with a response time of a second at single cell resolution. The magnitude of Ca^{2+} release is comparable to what is observed in neuronal cells (Delaney and Shahrezaei, 2013).

6.2.2 Increasing in intracellular Ca^{2+} induces rapid and transient cell contraction

I next investigated the consequence of the the rapid intracellular Ca^{2+} increase on cell shape. I thereby applied the Ca^{2+} uncaging experiments in the embryos expressing E-Cad-GFP to label epithelial cell-cell contacts. As predicted, I detected a reduction in the apical cross-sectional area of the target cell by half (Figure 6.3A, Supplementary movie 6.2), whereas target cells in control embryos with buffer injection remained largely unaffected (Figure 6.3B). I next measured the apical cross-sectional areas over time in both cases. Target cells in control embryos underwent minute-scale cell shape changes with a 10–20% amplitude of the cross-sectional area (Figure 6.3D and E, purple curve). All target cells with an increased Ca^{2+} reduced the cross-sectional area by half within 1-2 minutes (Figure 6.3D and E, blue curve). After 3 minutes, some of the target cells started to relax, but they did not fully recover to their original cross-sectional area in 5 minutes (Figure 6.3D and E, blue curve).

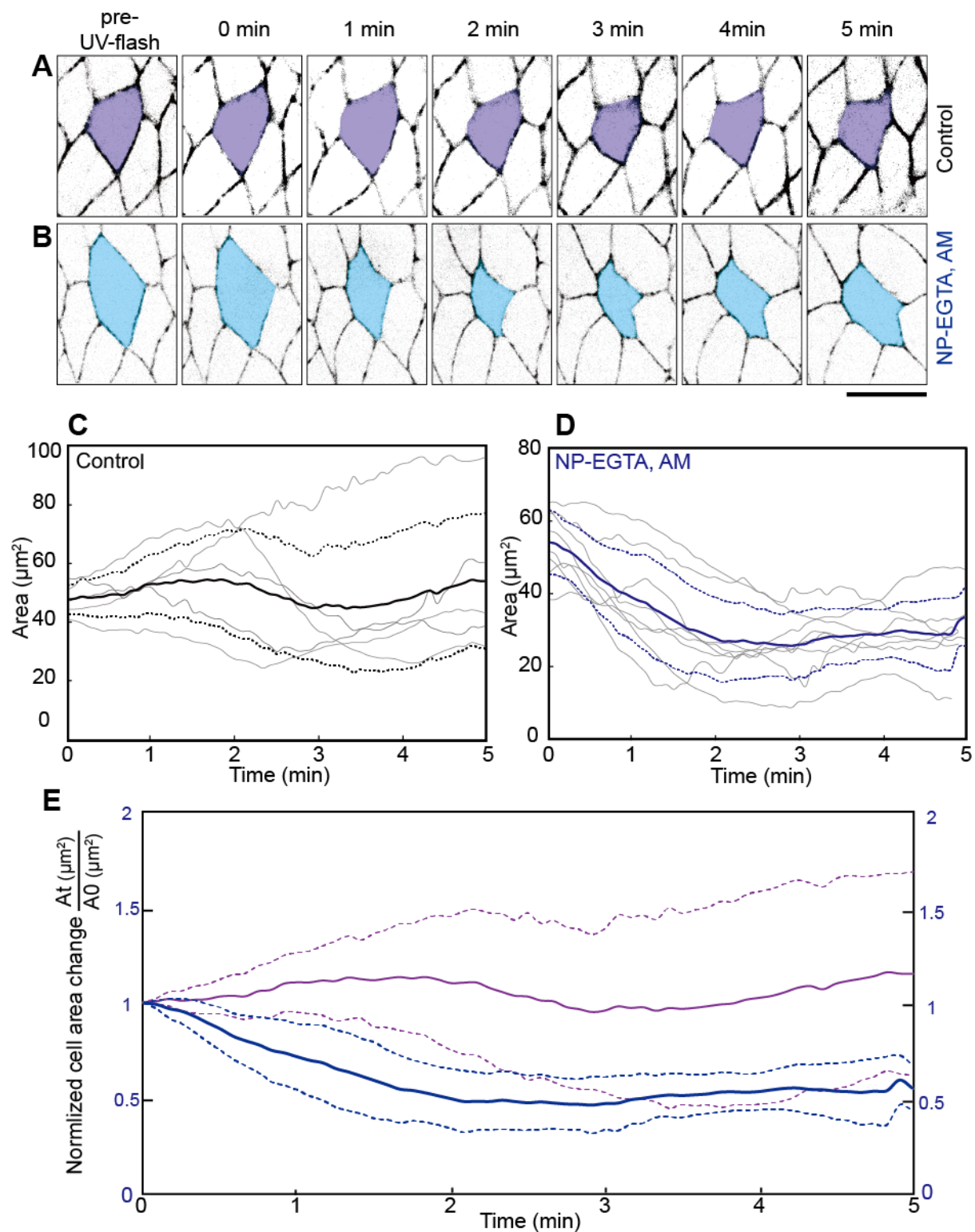


Figure 6.3 Ca^{2+} uncaging induces rapid contraction of epidermal cells.

(A, B) Images from time lapse recording of epithelial cells in embryos (stage 7) expressing E-Cad-GFP and injected with (A, C) buffer (control, $n=5$ embryos) or (B, D) 2 mM “NP-EGTA, AM” ($n=8$ embryos). Scale bar, 10 μm . Target cells are highlighted in blue. (C, D) Cross-sectional area of target cells exposed to UV light. Dash lines indicate confidence intervals of standard deviation of mean. Each gray line represents a single cell. (E) Mean of normalized cross-sectional cell area changes of target cells with UV-laser illuminations from the buffer injected control embryos (purple curve, $n=5$ embryos) and 2 mM “NP-EGTA, AM” injected embryos

(blue curve, $n=8$ embryos). Cell area (A_t) was normalized by the initial size (A_0). Dash lines indicate confidence intervals of standard deviation of mean.

Exposure to pulses of UV light and Ca^{2+} uncaging did not affect the behavior of the target cells within the tissue. I tracked target cells over an extended period of 15 min by time lapse imaging. The experiments were conducted during gastrulation stage when the embryo undergoes germband extension and epidermal cells rearrange by intercalation. It is difficult to get images larger than 15 min, since the cells move out of the field of view due to the gastrulation movement. Following the initial contraction phase during the first two minutes after UV exposure, the cell area was recovered, albeit it did not relax to initial size (Figure 6.4). The oscillatory changes of the cell area were observed. The period of this oscillation is in minutes and the amplitudes is 10-20%. This is a typical epithelial cell behavior (Fernandez-Gonzalez and Zallen, 2011; Yu and Fernandez-Gonzalez, 2016), which indicated that the target cells remained their epithelial property, as a part of the tissue (Figure 6.4). I did not observe any cases of target cell extrusion or loss from epithelial tissue.

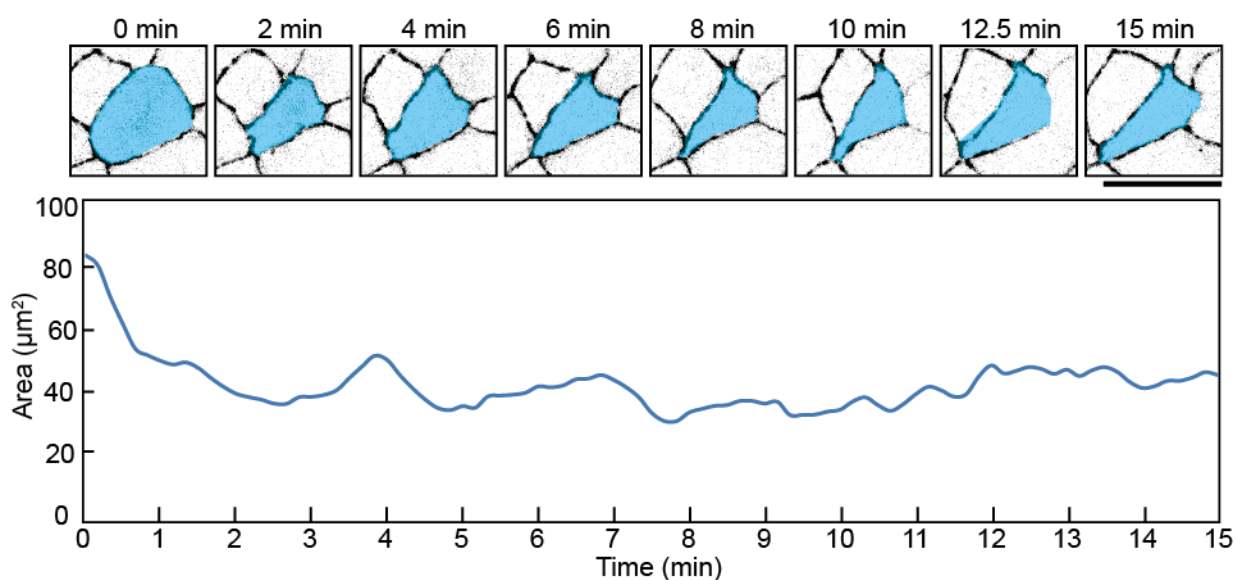


Figure 6.4 Apical area dynamics of target cell over 15 minutes.

Cross-sectional area of a target cell with extended recording over 15 minutes after an Ca^{2+} uncaging. Target cell is highlighted in blue. Scale bar, 10 μm .

In summary, the profiles of cell tracking and area measurements show that the uncaging method works robustly in the epithelial cells of the gastrulating *Drosophila* embryo. Consistent with Ca^{2+} imaging, I find that the induced contraction is restricted to the target cell. The area profiles showed a small variance and were consistent in multiple experiments (Figure 6.3D and E, blue curve). The exposure of UV light and the induced increase in intracellular Ca^{2+} were compatible with normal cell behavior as the target cells remained integrated in the epithelium and participated in tissue morphogenesis.

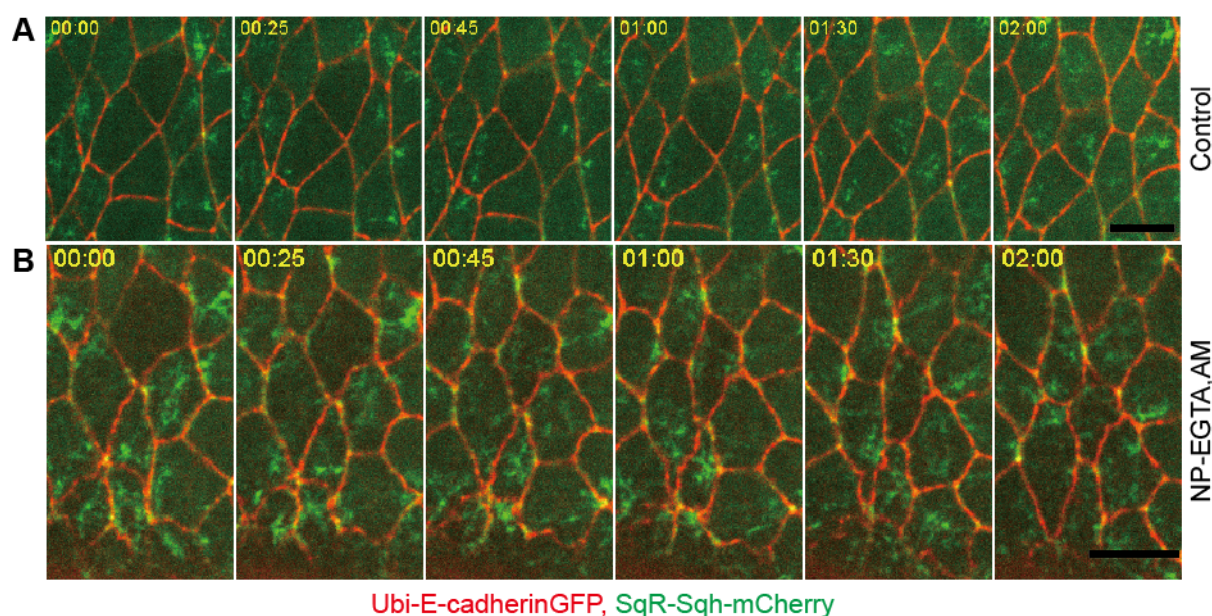


Figure 6.5 Myosin II dynamics in target cells.

Myosin II labelled with Sqh-mCherry. Images from time lapse recording in cells of the lateral epidermis in embryos (stage 7) expressing E-Cad-GFP (red) and Sqh-mCherry (green) after UV exposure. (A) buffer injected, (B) 2 mM “NP-EGTA, AM” injected. Yellow arrowheads point to target cells. Scale bar, 10 μm .

6.2.3 Role of Myosin II in Ca^{2+} induced cell contraction

The Ca^{2+} induced cell contraction can be caused by multiple mechanism. Given the time scale of a minute, it is unlikely that a transcriptional or translational response is involved. A change in cell volume may be involved. The increased Ca^{2+} may induce activation of non-muscle myosin II, comparable to what has been reported for the *Drosophila* egg chamber (He et al., 2010). Myosin II may be activated via Rho signaling, via Ca^{2+} dependent protein kinases or phosphatases controlling myosin II activity or directly by a Troponin C related mechanism. As the first step into investigating the mechanism of cell contraction, I imaged myosin II dynamics in embryos subjected to uncaging (Figure 6.5). I conducted the uncaging experiment in embryos expressing E-

Cad-GFP to label cell-cell contacts and Sqh-mCherry (myosin regulatory light chain), which forms visible cluster at sites of active myosin II mini filaments. Due to the exposure of UV light, the Sqh-mCherry signal was bleached in the target cell. However, a faster recovery of the Sqh-mCherry signal was observed in the target cells of embryos with induced cell contraction, whereas only a late recovery (>1min) of signal in control embryo. These observations are consistent with a myosin II based mechanism of Ca^{2+} induced cell contraction.

6.3 Discussion

I developed and validated a simple opto-chemical method to increase intracellular free Ca^{2+} concentration by Ca^{2+} uncaging, and induce apical constriction consequently in epithelial cells during tissue morphogenesis. This approach enables us to increase intracellular free Ca^{2+} concentration dramatically in single cell within seconds and induce very obvious apical contraction within 1 minute. The induced apical constriction are reversible and do not perturb cell fate. According to my knowledge, this is the first study which could induce the reversible and rapid epithelial cell contraction at single cell resolution during tissue morphogenesis.

The opto-chemical system that we used is based on photo-labile Ca^{2+} chelators and UV-laser of epi-fluorescence microscopy. The cage compound “NP-EGTA, AM” is cell-permeant, which can be loaded into cells conveniently and free Ca^{2+} can be released rapidly upon UV-laser illumination. Importantly, the method does not require any genetically encoded protein expressions in addition to application of cage compound. Furthermore, no recording channel in the visible spectrum is blocked by the uncaging laser, as this employs the UV range and is not applied continuously.

This uncaging approach thereby is particularly suitable for study of tissue morphogenesis. Comparison of cell and tissue behavior in wild type and mutants can be easily conducted without introducing additional genetic elements. This method can be easily adopted to other tissue and organism. The parameters for uncaging, such as light intensity and concentration of the cage compound, can be easily adopted in a controlled manner with Ca^{2+} sensors prior to the actual experiment.

Cell contractility has previously been modulated by different strategies. These optogenetic strategies include recruitment of $\text{PI}(4,5)\text{P}_2$ to deplete the actin cortex (Guglielmi et al., 2015), overexpressing of RhoA (Bugaj et al., 2013) and recruitment of

RhoA activator ARHGEF11 (Valon et al., 2017). Other strategies include ablation at single cell junctions (Rauzi et al., 2008; Solon et al., 2009), destruction of subcellular actomyosin network and activating wound healing locally by laser ablation (Yu and Fernandez-Gonzalez, 2016). Here I chose to induce rapid apical contraction by increasing the intracellular free Ca^{2+} in *Drosophila* embryos during tissue morphogenesis. By application of my optochemical approach, the apical area of target cells decreased to 50% in 1 minute (Figure 6.3). These results illustrate that intracellular free Ca^{2+} of neighbors remains unaffected while it increases rapidly in the target cells (Figure 6.2). It therefore suggests that my approach works at single cell resolution. Specifically, intercellular coupling coordination between immediate neighbors during cell contraction was demonstrated to be required for tissue morphogenesis, such as dorsal closure (Solon et al., 2009) and ventral furrow formation (Xie and Martin, 2015). This approach, which could work at single cell resolution, could be applied to investigate the detail mechanism of non-autonomous cell behavior mediated by mechanotransduction between immediate neighbors in the living organisms.

Although the details of mechanism for contraction need to be resolved, this method allows optically to induce cell contraction in a time scale relevant for tissue morphogenesis. The method can be applied to a wide range of processes and organisms and should greatly improve our understanding of the role of cell contractility and the mechanics during tissue morphogenesis.

6.4 Materials and Methods

See *chapter 2*.

REFERENCES

- Aebi, M., 2013. N-linked protein glycosylation in the ER. *Biochim. Biophys. Acta* 1833, 2430–2437. doi:10.1016/j.bbamcr.2013.04.001
- Aebi, M., Bernasconi, R., Clerc, S., Molinari, M., 2010. N-glycan structures: recognition and processing in the ER. *Trends Biochem. Sci.* 35, 74–82. doi:10.1016/j.tibs.2009.10.001
- Aigouy, B., Umetsu, D., Eaton, S., 2016. Segmentation and Quantitative Analysis of Epithelial Tissues. *Methods Mol. Biol.* 1478, 227–239. doi:10.1007/978-1-4939-6371-3_13
- Antunes, M., Pereira, T., Cordeiro, J.V., Almeida, L., Jacinto, A., 2013. Coordinated waves of actomyosin flow and apical cell constriction immediately after wounding. *J Cell Biol* 202, 365–379. doi:10.1083/jcb.201211039
- Aoki, K., Perlman, M., Lim, J.-M., Cantu, R., Wells, L., Tiemeyer, M., 2007. Dynamic developmental elaboration of N-linked glycan complexity in the *Drosophila melanogaster* embryo. *J. Biol. Chem.* 282, 9127–9142. doi:10.1074/jbc.M606711200
- Benton, M.A., Pechmann, M., Frey, N., Stappert, D., Conrads, K.H., Chen, Y.-T., Stamatakis, E., Pavlopoulos, A., Roth, S., 2016. Toll Genes Have an Ancestral Role in Axis Elongation. *Current Biology*. doi:10.1016/j.cub.2016.04.055
- Bertet, C., Sulak, L., Lecuit, T., 2004. Myosin-dependent junction remodelling controls planar cell intercalation and axis elongation. *Nature* 429, 667–671. doi:10.1038/nature02590
- Bischof, J., Maeda, R.K., Hediger, M., Karch, F., Basler, K., 2007. An optimized transgenesis system for *Drosophila* using germ-line-specific phiC31 integrases. *Proceedings of the National Academy of Sciences* 104, 3312–3317. doi:10.1073/pnas.0611511104
- Blanchard, G.B., Murugesu, S., Adams, R.J., Martinez-Arias, A., Gorfinkiel, N., 2010. Cytoskeletal dynamics and supracellular organisation of cell shape fluctuations during dorsal closure. *Development* 137, 2743–2752. doi:10.1242/dev.045872
- Blankenship, J.T., Backovic, S.T., Sanny, J.S.P., Weitz, O., Zallen, J.A., 2006a. Multicellular Rosette Formation Links Planar Cell Polarity to Tissue Morphogenesis. *Developmental Cell* 11, 459–470. doi:10.1016/j.devcel.2006.09.007
- Blankenship, J.T., Backovic, S.T., Sanny, J.S.P., Weitz, O., Zallen, J.A., 2006b. Multicellular Rosette Formation Links Planar Cell Polarity to Tissue Morphogenesis. *Developmental Cell* 11, 459–470.
- Borghini, N., Sorokina, M., Shcherbakova, O.G., Weis, W.I., Pruitt, B.L., Nelson, W.J., Dunn, A.R., 2012. E-cadherin is under constitutive actomyosin-generated tension that is increased at cell-cell contacts upon externally applied stretch. *Proc. Natl. Acad. Sci. U.S.A.* 109, 12568–12573. doi:10.1073/pnas.1204390109

REFERENCES

- Brand, A.H., Perrimon, N., 1993. Targeted gene expression as a means of altering cell fates and generating dominant phenotypes. *Development*.
- Brodland, G.W., Conte, V., Cranston, P.G., Veldhuis, J., Narasimhan, S., Hutson, M.S., Jacinto, A., Ulrich, F., Baum, B., Miodownik, M., 2010. Video force microscopy reveals the mechanics of ventral furrow invagination in *Drosophila*. *Proc. Natl. Acad. Sci. U.S.A.* 107, 22111–22116. doi:10.1073/pnas.1006591107
- Buckley, C.D., Tan, J., Anderson, K.L., Hanein, D., Volkman, N., Weis, W.I., Nelson, W.J., Dunn, A.R., 2014. Cell adhesion. The minimal cadherin-catenin complex binds to actin filaments under force. *Science* 346, 1254211–1254211. doi:10.1126/science.1254211
- Bugaj, L.J., Choksi, A.T., Mesuda, C.K., Kane, R.S., Schaffer, D.V., 2013. Optogenetic protein clustering and signaling activation in mammalian cells. *Nat Meth* 10, 249–252. doi:10.1038/nmeth.2360
- Burgalossi, A., Jung, S., Man, K.-N.M., Nair, R., Jockusch, W.J., Wojcik, S.M., Brose, N., Rhee, J.-S., 2012. Analysis of neurotransmitter release mechanisms by photolysis of caged Ca^{2+} in an autaptic neuron culture system. *Nature Protocols* 7, 1351–1365. doi:10.1038/nprot.2012.074
- Butler, L.C., Blanchard, G.B., Kabla, A.J., Lawrence, N.J., Welchman, D.P., Mahadevan, L., Adams, R.J., Sanson, B., 2009. Cell shape changes indicate a role for extrinsic tensile forces in *Drosophila* germ-band extension. *Nature Publishing Group* 11, 859–864. doi:10.1038/ncb1894
- Cai, D., Chen, S.-C., Prasad, M., He, L., Wang, X., Choesmel-Cadamuro, V., Sawyer, J.K., Danuser, G., Montell, D.J., 2014. Mechanical Feedback through E-Cadherin Promotes Direction Sensing during Collective Cell Migration. *Cell* 157, 1146–1159.
- Campinho, P., Behrndt, M., Ranft, J., Risler, T., Minc, N., Heisenberg, C.-P., 2013. Tension-oriented cell divisions limit anisotropic tissue tension in epithelial spreading during zebrafish epiboly. *Nat Cell Biol* 15, 1405–1414. doi:10.1038/ncb2869
- Campos-Ortega, J.A., Hartenstein, V., 1997. *The Embryonic Development of Drosophila melanogaster*. Springer Berlin Heidelberg, Berlin, Heidelberg. doi:10.1007/978-3-662-22489-2
- Cavey, M., Rauzi, M., Lenne, P.-F., Lecuit, T., 2008. A two-tiered mechanism for stabilization and immobilization of E-cadherin. *Nature* 453, 751–756. doi:10.1038/nature06953
- Chae, J., Kim, M.J., Goo, J.H., Collier, S., Gubb, D., Charlton, J., Adler, P.N., Park, W.J., 1999. The *Drosophila* tissue polarity gene *starry night* encodes a member of the protocadherin family. *Development* 126, 5421–5429. doi:10.1002/bies.950141103
- Chen, T.-W., Wardill, T.J., Sun, Y., Pulver, S.R., Renninger, S.L., Baohan, A., Schreiter, E.R., Kerr, R.A., Orger, M.B., Jayaraman, V., Looger, L.L., Svoboda, K., Kim, D.S., 2013. Ultrasensitive fluorescent proteins for imaging neuronal activity. *Nature* 499, 295–300. doi:10.1038/nature12354

REFERENCES

- Chou, T.B., Perrimon, N., 1992. Use of a yeast site-specific recombinase to produce female germline chimeras in *Drosophila*. *Genetics* 131, 643–653.
- Collinet, C., Rauzi, M., Lenne, P.-F., Lecuit, T., 2015. Local and tissue-scale forces drive oriented junction growth during tissue extension. *Nat Cell Biol* 17, 1247–1258. doi:10.1038/ncb3226
- Cost, A.-L., Ringer, P., Chrostek-Grashoff, A., Grashoff, C., 2015. How to Measure Molecular Forces in Cells: A Guide to Evaluating Genetically-Encoded FRET-Based Tension Sensors. *Cell Mol Bioeng* 8, 96–105. doi:10.1007/s12195-014-0368-1
- Curtin, J.A., Quint, E., Tsipouri, V., Arkell, R.M., Cattanach, B., Copp, A.J., Henderson, D.J., Spurr, N., Stanier, P., Fisher, E.M., Nolan, P.M., Steel, K.P., Brown, S.D.M., Gray, I.C., Murdoch, J.N., 2003. Mutation of *Celsr1* Disrupts Planar Polarity of Inner Ear Hair Cells and Causes Severe Neural Tube Defects in the Mouse. *Current Biology* 13, 1129–1133.
- da Silva, S.M., Vincent, J.P., 2007. Oriented cell divisions in the extending germband of *Drosophila*. *Development* 134, 3049–3054. doi:10.1242/dev.004911
- David, D.J.V., Tishkina, A., Harris, T.J.C., 2010. The PAR complex regulates pulsed actomyosin contractions during amnioserosa apical constriction in *Drosophila*. *Development* 137, 1645–1655. doi:10.1242/dev.044107
- de Matos Simões, S., Blankenship, J.T., Weitz, O., Farrell, D.L., Tamada, M., Fernandez-Gonzalez, R., Zallen, J.A., 2010. Rho-Kinase Directs Bazooka/Par-3 Planar Polarity during *Drosophila* Axis Elongation. *Developmental Cell* 19, 377–388. doi:10.1016/j.devcel.2010.08.011
- Delaney, K.R., Shahrezaei, V., 2013. Uncaging Calcium in Neurons. *Cold Spring Harbor Protocols*.
- Eldon, E., Kooyer, S., D'Evelyn, D., Duman, M., Lawinger, P., Botas, J., Bellen, H., 1994. The *Drosophila* 18 wheeler is required for morphogenesis and has striking similarities to Toll. *Development* 120, 885–899. doi:10.1038/341282a0
- Ellis-Davies, G.C., Kaplan, J.H., 1994. Nitrophenyl-EGTA, a photolabile chelator that selectively binds Ca²⁺ with high affinity and releases it rapidly upon photolysis. *Proceedings of the National Academy of Sciences* 91, 187–191.
- Engl, W., Arasi, B., Yap, L.L., Thiery, J.P., Viasnoff, V., 2014. Actin dynamics modulate mechanosensitive immobilization of E-cadherin at adherens junctions. *Nature Publishing Group* 16, 587–594. doi:10.1038/ncb2973
- Etienne-Manneville, S., Hall, A., 2002. Rho GTPases in cell biology. *Nature* 420, 629–635. doi:10.1038/nature01148
- Fehrentz, T., Schönberger, M., Trauner, D., 2011. Optochemical Genetics. *Angewandte Chemie International Edition* 50, 12156–12182. doi:10.1002/anie.201103236

REFERENCES

- Fernandez-Gonzalez, R., de Matos Simões, S., Roper, J.-C., Eaton, S., Zallen, J.A., 2009. Myosin II Dynamics Are Regulated by Tension in Intercalating Cells. *Developmental Cell* 17, 736–743. doi:10.1016/j.devcel.2009.09.003
- Fernandez-Gonzalez, R., Zallen, J.A., 2011. Oscillatory behaviors and hierarchical assembly of contractile structures in intercalating cells. *Phys. Biol.* 8, 045005–14. doi:10.1088/1478-3975/8/4/045005
- Ferreira, M.C., Hilfer, S.R., 1993. Calcium Regulation of Neural Fold Formation: Visualization of the Actin Cytoskeleton in Living Chick Embryos. *Dev. Biol.* 159, 427–440.
- Foe, V.E., 1989. Mitotic domains reveal early commitment of cells in *Drosophila* embryos. *Development* 107, 1–22.
- Forces for Morphogenesis Investigated with Laser Microsurgery and Quantitative Modeling, 2003. Forces for Morphogenesis Investigated with Laser Microsurgery and Quantitative Modeling 300, 145–149. doi:10.1126/science.1079552
- Leptin, M., Gastrulation in *Drosophila*: the formation of the ventral furrow and posterior midgut invaginations. 112, 775–789.
- Gaul, U., Seifert, E., Schuh, R., Jäckle, H., 1987. Analysis of Krüppel protein distribution during early *Drosophila* development reveals posttranscriptional regulation. *Cell* 50, 639–647.
- Gelbart, M.A., He, B., Martin, A.C., Thiberge, S.Y., Wieschaus, E.F., Kaschube, M., 2012. Volume conservation principle involved in cell lengthening and nucleus movement during tissue morphogenesis. *Proc. Natl. Acad. Sci. U.S.A.* 109, 19298–19303. doi:10.1073/pnas.1205258109
- González-Reyes, A., Morata, G., 1991. Organization of the *Drosophila* head as revealed by the ectopic expression of the Ultrathorax product. *Development* 113, 1459–1471.
- Grashoff, C., Hoffman, B.D., Brenner, M.D., Zhou, R., Parsons, M., Yang, M.T., McLean, M.A., Sligar, S.G., Chen, C.S., Ha, T., Schwartz, M.A., 2010. Measuring mechanical tension across vinculin reveals regulation of focal adhesion dynamics. *Nature* 466, 263–266. doi:10.1038/nature09198
- Großhans, J., Wenzl, C., Herz, H.-M., Bartoszewski, S., Schnorrer, F., Vogt, N., Schwarz, H., Müller, H.A., 2005. RhoGEF2 and the formin Dia control the formation of the furrow canal by directed actin assembly during *Drosophila* cellularisation. *Development* 132, 1009–1020. doi:10.1242/dev.01669
- Guglielmi, G., Barry, J.D., Huber, W., De Renzis, S., 2015. An Optogenetic Method to Modulate Cell Contractility during Tissue Morphogenesis. *Developmental Cell* 35, 646–660.
- Haecker, A., Bergman, M., Neupert, C., Moussian, B., Luschnig, S., Aebi, M., Mannervik, M., 2008. Wollknäuel is required for embryo patterning and encodes the *Drosophila* ALG5 UDP-glucose:dolichylphosphate glucosyltransferase. *Development* 135, 1745–1749. doi:10.1242/dev.020891

REFERENCES

- Hagen, ten, K.G., Zhang, L., Tian, E., Zhang, Y., 2009. Glycobiology on the fly: developmental and mechanistic insights from *Drosophila*. *Glycobiology* 19, 102–111. doi:10.1093/glycob/cwn096
- Harada, Y., Hirayama, H., Suzuki, T., 2015. Generation and degradation of free asparagine-linked glycans. *Cell. Mol. Life Sci.* 72, 2509–2533. doi:10.1007/s00018-015-1881-7
- Harden, N., 2002. Signaling pathways directing the movement and fusion of epithelial sheets: lessons from dorsal closure in *Drosophila*. *Differentiation* 70, 181–203. doi:10.1046/j.1432-0436.2002.700408.x
- Harris, T.J.C., Peifer, M., 2005. The positioning and segregation of apical cues during epithelial polarity establishment in *Drosophila*. *J Cell Biol* 170, 813–823. doi:10.1083/jcb.200505127
- Harris, T.J.C., Peifer, M., 2004. Adherens junction-dependent and -independent steps in the establishment of epithelial cell polarity in *Drosophila*. *J Cell Biol* 167, 135–147. doi:10.1083/jcb.200406024
- Hartman, M.A., Spudich, J.A., 2012. The myosin superfamily at a glance. *Journal of Cell Science* 125, 1627–1632. doi:10.1242/jcs.094300
- He, L., Wang, X., Tang, H.L., Montell, D.J., 2010. Tissue elongation requires oscillating contractions of a basal actomyosin network. *Nat Cell Biol* 12, 1133–1142. doi:10.1038/ncb2124
- Heesen, S.T., Lehle, L., Weissmann, A., Aebi, M., 1994. Isolation of the ALG5 Locus Encoding the UDP-Glucose:Dolichyl-Phosphate Glucosyltransferase from *Saccharomyces cerevisiae*. *The FEBS Journal* 224, 71–79. doi:10.1111/j.1432-1033.1994.tb19996.x
- Helenius, A., Aebi, M., 2004. Roles of N-Linked Glycans in the Endoplasmic Reticulum. <http://dx.doi.org/10.1146/annurev.biochem.73.011303.073752> 73, 1019–1049. doi:10.1146/annurev.biochem.73.011303.073752
- Hoffman, B.D., Yap, A.S., 2015. Towards a Dynamic Understanding of Cadherin-Based Mechanobiology. *Trends in Cell Biology* 25, 803–814.
- Hoyer, H., 1882. Beitrage zur histologischen Technik. *Biologisches Zentralblatt*.
- Huang, J., Zhou, W., Dong, W., Watson, A.M., Hong, Y., 2009. Directed, efficient, and versatile modifications of the *Drosophila* genome by genomic engineering. *Proceedings of the National Academy of Sciences* 106, 8284–8289. doi:10.1073/pnas.0900641106
- Hunter, G.L., Crawford, J.M., Jenkins, J.Z., Kiehart, D.P., 2014. Ion channels contribute to the regulation of cell sheet forces during *Drosophila* dorsal closure. *Development* 141, 325–334. doi:10.1242/dev.097097
- Hunter, M.V., Lee, D.M., Harris, T.J.C., Fernandez-Gonzalez, R., 2015. Polarized E-cadherin endocytosis directs actomyosin remodeling during embryonic wound repair. *J Cell Biol* 210, 801–816. doi:10.1083/jcb.201501076
- Imbach, T., Burda, P., Kuhnert, P., Wevers, R.A., Aebi, M., Berger, E.G., Hennet, T., 1999. A mutation in the human ortholog of the *Saccharomyces cerevisiae* ALG6 gene causes carbohydrate-deficient glycoprotein

REFERENCES

- syndrome type-Ic. *Proceedings of the National Academy of Sciences* 96, 6982–6987. doi:10.1073/pnas.96.12.6982
- Irvine, K.D., Wieschaus, E., 1994. Cell intercalation during *Drosophila* germband extension and its regulation by pair-rule segmentation genes. *Development* 120, 827–841.
- Jordan, P., Karess, R., 1997. Myosin light chain-activating phosphorylation sites are required for oogenesis in *Drosophila*. *J Cell Biol* 139, 1805–1819. doi:10.1083/jcb.139.7.1805
- Kam, Z., Minden, J.S., Agard, D.A., Sedat, J.W., Leptin, M., 1991. *Drosophila* gastrulation: analysis of cell shape changes in living embryos by three-dimensional fluorescence microscopy. *Development* 112, 365–370.
- Kambris, Z., Hoffmann, J.A., Imler, J.-L., Capovilla, M., 2002. Tissue and stage-specific expression of the Tolls in *Drosophila* embryos. *Gene Expression Patterns* 2, 311–317. doi:10.1016/S1567-133X(02)00020-0
- Kasza, K.E., Farrell, D.L., Zallen, J.A., 2014. Spatiotemporal control of epithelial remodeling by regulated myosin phosphorylation. *Proc. Natl. Acad. Sci. U.S.A.* 111, 11732–11737. doi:10.1073/pnas.1400520111
- Katoh, T., Tiemeyer, M., 2013. The Ns and Os of *Drosophila* glycoprotein glycobiology. *Glycoconj. J.* 30, 57–66. doi:10.1007/s10719-012-9442-x
- Keller, R., 2002. Shaping the vertebrate body plan by polarized embryonic cell movements. *Science* 298, 1950–1954. doi:10.1126/science.1079478
- Kerridge, S., Munjal, A., Philippe, J.-M., Jha, A., las Bayonas, de, A.G., Saurin, A.J., Lecuit, T., 2016. Modular activation of Rho1 by GPCR signalling imparts polarized myosin II activation during morphogenesis. *Nat Cell Biol* 18, 261–270. doi:10.1038/ncb3302
- Kitazawa, T., Gaylinn, B.D., Denney, G.H., Somlyo, A.P., 1991. G-protein-mediated Ca^{2+} sensitization of smooth muscle contraction through myosin light chain phosphorylation. *J. Biol. Chem.* 266, 1708–1715.
- Kolesnikov, T., Beckendorf, S.K., 2007. 18 Wheeler regulates apical constriction of salivary gland cells via the Rho-GTPase-signaling pathway. *Dev. Biol.* 307, 53–61. doi:10.1016/j.ydbio.2007.04.014
- Lee, H., Nagele, R.G., 1986. Toxic and teratologic effects of verapamil on early chick embryos: Evidence for the involvement of calcium in neural tube closure. *Teratology* 33, 203–211. doi:10.1002/tera.1420330207
- Lee, H.C., Auersperg, N., 1980. Calcium in epithelial cell contraction. *J Cell Biol* 85, 325–336.
- Leptin, M., 1995. *Drosophila* Gastrulation: From Pattern Formation to Morphogenesis. *Annual Review of Cell and Developmental Biology* 11, 189–212. doi:10.1146/annurev.cb.11.110195.001201
- Leptin, M., Grunewald, B., 1990. Cell shape changes during gastrulation in *Drosophila*. *Development* 110, 73–84.

REFERENCES

- Levayer, R., Lecuit, T., 2013. Oscillation and Polarity of E-Cadherin Asymmetries Control Actomyosin Flow Patterns during Morphogenesis. *Developmental Cell* 26, 162–175. doi:10.1016/j.devcel.2013.06.020
- Levayer, R., Pelissier-Monier, A., Lecuit, T., 2011. Spatial regulation of Dia and Myosin-II by RhoGEF2 controls initiation of E-cadherin endocytosis during epithelial morphogenesis. *Nature Publishing Group* 13, 529–540. doi:10.1038/ncb2224
- Liu, Z., Tan, J.L., Cohen, D.M., Yang, M.T., Sniadecki, N.J., Ruiz, S.A., Nelson, C.M., Chen, C.S., 2010. Mechanical tugging force regulates the size of cell-cell junctions. *Proc. Natl. Acad. Sci. U.S.A.* 107, 9944–9949. doi:10.1073/pnas.0914547107
- Liwoz, A., Lei, T., Kukuruzinska, M.A., 2006. N-glycosylation affects the molecular organization and stability of E-cadherin junctions. *J. Biol. Chem.* 281, 23138–23149. doi:10.1074/jbc.M512621200
- Lommel, M., Winterhalter, P.R., Willer, T., Dahlhoff, M., Schneider, M.R., Bartels, M.F., Renner-Müller, I., Ruppert, T., Wolf, E., Strahl, S., 2013. Protein O-mannosylation is crucial for E-cadherin-mediated cell adhesion. *Proc. Natl. Acad. Sci. U.S.A.* 110, 21024–21029. doi:10.1073/pnas.1316753110
- Lye, C.M., Blanchard, G.B., Naylor, H.W., Muresan, L., Huisken, J., Adams, R.J., Sanson, B., 2015. Mechanical Coupling between Endoderm Invagination and Axis Extension in *Drosophila*. *PLoS Biol* 13, e1002292–27. doi:10.1371/journal.pbio.1002292
- Lye, C.M., Sanson, B., 2011. Tension and epithelial morphogenesis in *Drosophila* early embryos. *Curr. Top. Dev. Biol.* 95, 145–187. doi:10.1016/B978-0-12-385065-2.00005-0
- Maitre, J.-L., Heisenberg, C.-P., 2013. Three Functions of Cadherins in Cell Adhesion. *Current Biology* 23, R626–R633.
- Maley, F., Trimble, R.B., Tarentino, A.L., 1989. Characterization of glycoproteins and their associated oligosaccharides through the use of endoglycosidases. *Anal Biochem* 180(2):195-204.
- Markova, O., Sénatore, S., Chardès, C., Lenne, P.-F., 2015. Calcium Spikes in Epithelium: study on *Drosophila* early embryos. *Scientific Reports* 5, 11379. doi:10.1038/srep11379
- Martin, A.C., Goldstein, B., 2014. Apical constriction: themes and variations on a cellular mechanism driving morphogenesis. *Development* 141, 1987–1998. doi:10.1242/dev.102228
- Martin, A.C., Kaschube, M., Wieschaus, E.F., 2009. Pulsed contractions of an actin–myosin network drive apical constriction. *Nature* 457, 495–499. doi:10.1038/nature07522
- Mayer, M., Depken, M., Bois, J.S., Jülicher, F., Grill, S.W., 2010. Anisotropies in cortical tension reveal the physical basis of polarizing cortical flows. *Nature* 467, 617–621. doi:10.1038/nature09376
- Morais-de-Sá, E., Mirouse, V., St Johnston, D., 2010. aPKC Phosphorylation of Bazooka Defines the Apical/Lateral Border in *Drosophila* Epithelial Cells. *Cell* 141, 509–523. doi:10.1016/j.cell.2010.02.040

REFERENCES

- Muliyil, S., Krishnakumar, P., Narasimha, M., 2011. Spatial, temporal and molecular hierarchies in the link between death, delamination and dorsal closure. *Development* 138, 3043–3054. doi:10.1242/dev.060731
- Munjal, A., Philippe, J.-M., Munro, E., Lecuit, T., 2015. A self-organized biomechanical network drives shape changes during tissue morphogenesis. *Nature* 524, 351–355. doi:10.1038/nature14603
- Müller, H.A., Wieschaus, E., 1996. armadillo, bazooka, and stardust are critical for early stages in formation of the zonula adherens and maintenance of the polarized blastoderm epithelium in *Drosophila*. *J Cell Biol* 134, 149–163.
- Nasiadka, A., Dietrich, B.H., Krause, H.M., 2002. Anterior-posterior patterning in the *Drosophila* embryo, in: *Gene Expression at the Beginning of Animal Development, Advances in Developmental Biology and Biochemistry*. Elsevier, pp. 155–204. doi:10.1016/S1569-1799(02)12027-2
- Nicholas D Poulson, T.L., 2012. Asymmetric Cell Divisions in the Epidermis. *International review of cell and molecular biology* 295, 199–232. doi:10.1016/B978-0-12-394306-4.00012-5
- Nowotarski, S.H., Peifer, M., 2014. Cell Biology: A Tense but Good Day for Actin at Cell–Cell Junctions. *Current Biology* 24, R688–R690.
- Oda, H., Tsukita, S., 2001. Real-time imaging of cell-cell adherens junctions reveals that *Drosophila* mesoderm invagination begins with two phases of apical constriction of cells. *Journal of Cell Science* 114, 493–501. doi:10.1016/S0092-8674(00)80482-1
- Oda, H., Uemura, T., Shiomi, K., Nagafuchi, A., Tsukita, S., Takeichi, M., 1993. Identification of a *Drosophila* homologue of alpha-catenin and its association with the armadillo protein. *J Cell Biol* 121, 1133–1140. doi:10.1083/jcb.121.5.1133
- Paré, A.C., Vichas, A., Fincher, C.T., Mirman, Z., Farrell, D.L., Mainieri, A., Zallen, J.A., 2014. A positional Toll receptor code directs convergent extension in *Drosophila*. *Nature* 515, 523–527. doi:10.1038/nature13953
- Parnas, D., Haghighi, A.P., Fetter, R.D., Kim, S.W., 2001. Regulation of postsynaptic structure and protein localization by the Rho-type guanine nucleotide exchange factor dPix. *Neuron*.
- Patel, N.H., Martin-Blanco, E., Coleman, K.G., Poole, S.J., 1989. Expression of engrailed proteins in arthropods, annelids, and chordates. *Cell*.
- Perrimon, N., Mahowald, A.P., 1987. Multiple functions of segment polarity genes in *Drosophila*. *Dev. Biol.* 119, 587–600. doi:10.1016/0012-1606(87)90061-3
- Perry, M.W., Bothma, J.P., Luu, R.D., Levine, M., 2012. Precision of Hunchback Expression in the *Drosophila* Embryo. *Current Biology* 22, 2247–2252.

REFERENCES

- Pinheiro, D., Hannezo, E., Herszterg, S., Bosveld, F., Gaugue, I., Balakireva, M., Wang, Z., Cristo, I., Rigaud, S.U., Markova, O., Bellaïche, Y., 2017. Transmission of cytokinesis forces via E-cadherin dilution and actomyosin flows. *Nature* 545, 103–107. doi:10.1038/nature22041
- Pinho, S.S., Seruca, R., Gärtner, F., Yamaguchi, Y., Gu, J., Taniguchi, N., Reis, C.A., 2011. Modulation of E-cadherin function and dysfunction by N-glycosylation. *Cell. Mol. Life Sci.* 68, 1011–1020. doi:10.1007/s00018-010-0595-0
- Pokutta, S., Choi, H.-J., Ahlsen, G., Hansen, S.D., Weis, W.I., 2014. Structural and thermodynamic characterization of cadherin- β -catenin- α -catenin complex formation. *J. Biol. Chem.* 289, 13589–13601. doi:10.1074/jbc.M114.554709
- Pope, K.L., Harris, T.J.C., 2008. Control of cell flattening and junctional remodeling during squamous epithelial morphogenesis in *Drosophila*. *Development* 135, 2227–2238. doi:10.1242/dev.019802
- Quang, B.-A.T., Mani, M., Markova, O., Lecuit, T., Lenne, P.-F., 2013. Principles of E-Cadherin Supramolecular Organization *In-Vivo*. *Current Biology* 23, 2197–2207. doi:10.1016/j.cub.2013.09.015
- Rauzi, M., Krzic, U., Saunders, T.E., Krajnc, M., Zihler, P., Hufnagel, L., Leptin, M., 2015. Embryo-scale tissue mechanics during *Drosophila* gastrulation movements. *Nature Communications* 6, 8677. doi:10.1038/ncomms9677
- Rauzi, M., Lenne, P.-F., Lecuit, T., 2010. Planar polarized actomyosin contractile flows control epithelial junction remodelling. *Nature* 468, 1110–1114. doi:10.1038/nature09566
- Rauzi, M., Verant, P., Lecuit, T., Lenne, P.-F., 2008. Nature and anisotropy of cortical forces orienting *Drosophila* tissue morphogenesis. *Nat Cell Biol* 10, 1401–1410. doi:10.1038/ncb1798
- Reiss, G., Heesen, S., Zimmerman, J., Robbins, P., 1996. Isolation of the ALG6 locus of *Saccharomyces cerevisiae* required for glucosylation in the N-linked glycosylation pathway.
- Riggleman, B., Schedl, P., Wieschaus, E., 1990. Spatial expression of the *Drosophila* segment polarity gene *armadillo* is posttranscriptionally regulated by *wingless*. *Cell*.
- Rimm, D.L., Koslov, E.R., Kebriaei, P., Cianci, C.D., Morrow, J.S., 1995. Alpha (E)-catenin is an actin-binding and -bundling protein mediating the attachment of F-actin to the membrane adhesion complex. *Proceedings of the National Academy of Sciences* 92, 8813–8817.
- Sambrook, J., Russell, D.W., 2001. *Molecular cloning. A Laboratory Manual*. 3era. ed. 1: 1.32-1.34.
- Santos, dos, G., Schroeder, A.J., Goodman, J.L., Strelets, V.B., Crosby, M.A., Thurmond, J., Emmert, D.B., Gelbart, W.M., FlyBase Consortium, 2015. FlyBase: introduction of the *Drosophila melanogaster* Release 6 reference genome assembly and large-scale migration of genome annotations. *Nucl. Acids Res.* 43, D690–7. doi:10.1093/nar/gku1099

REFERENCES

- Sawyer, J.K., Choi, W., Jung, K.-C., He, L., Harris, N.J., Peifer, M., 2011. A contractile actomyosin network linked to adherens junctions by Canoe/afadin helps drive convergent extension. *Mol. Biol. Cell* 22, 2491–2508. doi:10.1091/mbc.E11-05-0411
- Schindelin, J., Arganda-Carreras, I., Frise, E., Kaynig, V., 2012. Fiji: an open-source platform for biological-image analysis. *Nature*.
- Schupbach, T., Wieschaus, E., 1986. Germline autonomy of maternal-effect mutations altering the embryonic body pattern of *Drosophila*. *Dev. Biol.* 113, 443–448.
- Sellers, J.R., Spudich, J.A., Sheetz, M.P., 1985. Light chain phosphorylation regulates the movement of smooth muscle myosin on actin filaments. *J Cell Biol* 101, 1897–1902. doi:10.1083/jcb.101.5.1897
- Shaik, K.S., Pabst, M., Schwarz, H., Altmann, F., Moussian, B., 2011. The Alg5 ortholog Wollknäuel is essential for correct epidermal differentiation during *Drosophila* late embryogenesis. *Glycobiology* 21, 743–756. doi:10.1093/glycob/cwq213
- Simões, S. de M., Mainieri, A., Zallen, J.A., 2014. Rho GTPase and Shroom direct planar polarized actomyosin contractility during convergent extension. *J Cell Biol* 204, 575–589. doi:10.1083/jcb.201307070
- Small, S., Kraut, R., Hoey, T., Warrior, R., Levine, M., 1991. Transcriptional regulation of a pair-rule stripe in *Drosophila*. *Genes Dev.* 5, 827–839. doi:10.1101/gad.5.5.827
- Smedley, M.J., Stanisstreet, M., 1986. Calcium and neurulation in mammalian embryos. II. Effects of cytoskeletal inhibitors and calcium antagonists on the neural folds of rat embryos. *J Embryol Exp Morphol* 93, 167–178.
- Soap, cells and statistics—random patterns in two dimensions, 2006. *Soap, cells and statistics—random patterns in two dimensions* 25, 59–99. doi:10.1080/00107518408210979
- Solon, J., Kaya-?opur, A., Colombelli, J., Brunner, D., 2009. Pulsed Forces Timed by a Ratchet-like Mechanism Drive Directed Tissue Movement during Dorsal Closure. *Cell* 137, 1331–1342. doi:10.1016/j.cell.2009.03.050
- Spencer, A.K., Siddiqui, B.A., Thomas, J.H., 2015. Cell shape change and invagination of the cephalic furrow involves reorganization of F-actin. *Dev. Biol.* 402, 192–207. doi:10.1016/j.ydbio.2015.03.022
- Spirov, A., Fahmy, K., Schneider, M., Frei, E., Noll, M., Baumgartner, S., 2009. Formation of the bicoid morphogen gradient: an mRNA gradient dictates the protein gradient. *Development* 136, 605–614. doi:10.1242/dev.031195
- Stagljar, I., Heesen, te, S., Aebi, M., 1994a. New phenotype of mutations deficient in glucosylation of the lipid-linked oligosaccharide: cloning of the ALG8 locus. *Proceedings of the National Academy of Sciences* 91, 5977–5981.

REFERENCES

- Stagljar, I., Heesen, te, S., Aebi, M., 1994b. New phenotype of mutations deficient in glucosylation of the lipid-linked oligosaccharide: cloning of the ALG8 locus. *Proceedings of the National Academy of Sciences* 91, 5977–5981.
- Sung, H.-W., Spangenberg, S., Vogt, N., Großhans, J., 2013. Number of Nuclear Divisions in the *Drosophila* Blastoderm Controlled by Onset of Zygotic Transcription. *Current Biology* 23, 133–138. doi:10.1016/j.cub.2012.12.013
- Suzuki, H., ONISHI, H., TAKAHASHI, K., Watanabe, S., 1978. Structure and function of chicken gizzard myosin. *J Biochem* 84, 1529–1542.
- Suzuki, M., Sato, M., Koyama, H., Hara, Y., Hayashi, K., Yasue, N., Imamura, H., Fujimori, T., Nagai, T., Campbell, R.E., Ueno, N., 2017. Distinct intracellular Ca(2+) dynamics regulate apical constriction and differentially contribute to neural tube closure. *Development* 144, 1307–1316. doi:10.1242/dev.141952
- T H Plummer, J., Tarentino, A.L., 1991. Purification of the oligosaccharide-cleaving enzymes of *Flavobacterium meningosepticum*. *Glycobiology* 1, 257–263. doi:10.1093/glycob/1.3.257
- Takeichi, M., 2014. Dynamic contacts: rearranging adherens junctions to drive epithelial remodelling. *Nat Rev Mol Cell Biol* 15, 397–410. doi:10.1038/nrm3802
- Tamada, M., Farrell, D.L., Zallen, J.A., 2012. Abl Regulates Planar Polarized Junctional Dynamics through Beta-Catenin Tyrosine Phosphorylation. *Developmental Cell* 22, 309–319. doi:10.1016/j.devcel.2011.12.025
- Tamada, M., Zallen, J.A., 2015. Square Cell Packing in the *Drosophila* Embryo through Spatiotemporally Regulated EGF Receptor Signaling. *Developmental Cell* 35, 151–161. doi:10.1016/j.devcel.2015.09.015
- Tepass, U., 2014. Developmental biology: Polarize to elongate. *Nature* 515, 499–501. doi:10.1038/nature13937
- Toettcher, J.E., Voigt, C.A., Weiner, O.D., Lim, W.A., 2011. The promise of optogenetics in cell biology: interrogating molecular circuits in space and time. *Nat Meth.*
- Tomer, R., Khairy, K., Amat, F., Keller, P.J., 2012. Quantitative high-speed imaging of entire developing embryos with simultaneous multiview light-sheet microscopy. *Nat Meth* 9, 755–763. doi:10.1038/nmeth.2062
- Toyama, Y., Peralta, X.G., Wells, A.R., Kiehart, D.P., Edwards, G.S., 2008. Apoptotic Force and Tissue Dynamics During *Drosophila* Embryogenesis. *Science* 321, 1683–1686. doi:10.1126/science.1157052
- Truong Quang, B.-A., Mani, M., Markova, O., Lecuit, T., Lenne, P.-F., 2013. Principles of E-Cadherin Supramolecular Organization In Vivo. *Current Biology* 23, 2197–2207. doi:10.1016/j.cub.2013.09.015
- Valon, L., Marín-Llauradó, A., Wyatt, T., Charras, G., Trepac, X., 2017. Optogenetic control of cellular forces and mechanotransduction. *Nature Communications* 8, 14396. doi:10.1038/ncomms14396

REFERENCES

- Vester-Christensen, M.B., Halim, A., Joshi, H.J., Steentoft, C., Bennett, E.P., Levery, S.B., Vakhrushev, S.Y., Clausen, H., 2013. Mining the O-mannose glycoproteome reveals cadherins as major O-mannosylated glycoproteins. *Proc. Natl. Acad. Sci. U.S.A.* 110, 21018–21023. doi:10.1073/pnas.1313446110
- Vichas, A., Zallen, J.A., 2011. Translating cell polarity into tissue elongation. *Seminars in Cell & Developmental Biology* 22, 858–864. doi:10.1016/j.semcd.2011.09.013
- Vincent, A., Blankenship, J.T., Wieschaus, E., 1997. Integration of the head and trunk segmentation systems controls cephalic furrow formation in *Drosophila*. *Development* 124, 3747–3754.
- Vogt, N., Koch, I., Schwarz, H., Schnorrer, F., Nüsslein-Volhard, C., 2006. The gammaTuRC components Grip75 and Grip128 have an essential microtubule-anchoring function in the *Drosophila* germline. *Development* 133, 3963–3972. doi:10.1242/dev.02570
- Wakefield, S., Tear, G., 2006. The *Drosophila* reticulon, Rtnl-1, has multiple differentially expressed isoforms that are associated with a sub-compartment of the endoplasmic reticulum. *Cell. Mol. Life Sci.* 63, 2027–2038. doi:10.1007/s00018-006-6142-3
- Walck-Shannon, E., Hardin, J., 2014. Cell intercalation from top to bottom. *Nat Rev Mol Cell Biol* 15, 34–48. doi:10.1038/nrm3723
- Wang, Y.-C., Khan, Z., Kaschube, M., Wieschaus, E.F., 2012. Differential positioning of adherens junctions is associated with initiation of epithelial folding. *Nature* 484, 390–393. doi:10.1038/nature10938
- Warrington, S.J., Strutt, H., Strutt, D., 2013. The Frizzled-dependent planar polarity pathway locally promotes E-cadherin turnover via recruitment of RhoGEF2. *Development* 140, 1045–1054. doi:10.1242/dev.088724
- Weaire, D., Rivier, N., 1984. *Statistical Crystallography: Hidden Order in Chaos*. Contemp. Physics.
- Wei, S.-Y., Escudero, L.M., Yu, F., Chang, L.-H., Chen, L.-Y., Ho, Y.-H., Lin, C.-M., Chou, C.-S., Chia, W., Modolell, J., Hsu, J.-C., 2005. Echinoid Is a Component of Adherens Junctions That Cooperates with DE-Cadherin to Mediate Cell Adhesion. *Developmental Cell* 8, 493–504. doi:10.1016/j.devcel.2005.03.015
- Weitkunat, M., Kaya-Çopur, A., Grill, S.W., Schnorrer, F., 2014. Tension and Force-Resistant Attachment Are Essential for Myofibrillogenesis in *Drosophila* Flight Muscle. *Current Biology* 24, 705–716.
- Whitehead, J., Vignjevic, D., Fütterer, C., Beaupaire, E., Robine, S., Farge, E., 2008. Mechanical factors activate β -catenin-dependent oncogene expression in APC 1638N/+mouse colon. *HFSP Journal* 2, 286–294. doi:10.2976/1.2955566
- Winter, C.G., Wang, B., Ballew, A., Royou, A., Karess, R., Axelrod, J.D., Luo, L., 2001. *Drosophila* Rho-Associated Kinase (Drok) Links Frizzled-Mediated Planar Cell Polarity Signaling to the Actin Cytoskeleton. *Cell* 105, 81–91. doi:10.1016/S0092-8674(01)00298-7
- Wodarz, A., Ramrath, A., Kuchinke, U., Knust, E., 1999. Bazooka provides an apical cue for Inscuteable localization in *Drosophila* neuroblasts. *Nature* 402, 544–547. doi:10.1038/990128

REFERENCES

- Worby, C.A., Simonson-Leff, N., Dixon, J.E., 2001. RNA interference of gene expression (RNAi) in cultured *Drosophila* cells. *Sci. STKE* 2001, p11–p11. doi:10.1126/stke.2001.95.p11
- Wu, Y., Kanchanawong, P., Zaidel-Bar, R., 2015. Actin-Delimited Adhesion-Independent Clustering of E-Cadherin Forms the Nanoscale Building Blocks of Adherens Junctions. *Developmental Cell* 32, 139–154.
- Xie, S., Martin, A.C., 2015. Intracellular signalling and intercellular coupling coordinate heterogeneous contractile events to facilitate tissue folding. *Nature Communications* 6, 7161. doi:10.1038/ncomms8161
- Yamada, S., Pokutta, S., Drees, F., Weis, W.I., Nelson, W.J., 2005. Deconstructing the Cadherin-Catenin-Actin Complex. *Cell* 123, 889–901.
- Yang, Y., Mlodzik, M., 2015. Wnt-Frizzled/planar cell polarity signaling: cellular orientation by facing the wind (Wnt). *Annual Review of Cell and Developmental Biology* 31, 623–646. doi:10.1146/annurev-cellbio-100814-125315
- Yao, M., Qiu, W., Liu, R., Efremov, A.K., Cong, P., Seddiki, R., Payre, M., Lim, C.T., Ladoux, B., Mège, R.-M., Yan, J., 2014. Force-dependent conformational switch of α -catenin controls vinculin binding. *Nature Communications* 5. doi:10.1038/ncomms5525
- Yu, J.C., Fernandez-Gonzalez, R., 2016. Local mechanical forces promote polarized junctional assembly and axis elongation in *Drosophila*. *eLife* 5, 20246. doi:10.7554/eLife.10757
- Zallen, J.A., Wieschaus, E., 2004. Patterned gene expression directs bipolar planar polarity in *Drosophila*. *Developmental Cell* 6, 343–355.
- Zhang, X., Koolhaas, W.H., Schnorrer, F., 2014. A Versatile Two-Step CRISPR- and RMCE-Based Strategy for Efficient Genome Engineering in *Drosophila*. *G3: Genes|Genomes|Genetics* 4, 2409–2418. doi:10.1534/g3.114.013979
- Zhang, Y., Kong, D., Reichl, L., Vogt, N., Wolf, F., Großhans, J., 2014. The glucosyltransferase Xiantuan of the endoplasmic reticulum specifically affects E-Cadherin expression and is required for gastrulation movements in *Drosophila*. *Dev. Biol.* 390, 208–220. doi:10.1016/j.ydbio.2014.03.007
- Zhao, H., Liang, Y., Xu, Z., Wang, L., Zhou, F., Li, Z., Jin, J., Yang, Y., Fang, Z., Hu, Y., Zhang, L., Su, J., Zha, X., 2008. N-glycosylation affects the adhesive function of E-Cadherin through modifying the composition of adherens junctions (AJs) in human breast carcinoma cell line MDA-MB-435. *J. Cell. Biochem.* 104, 162–175. doi:10.1002/jcb.21608
- Zhou, F., Su, J., Fu, L., Yang, Y., Zhang, L., Wang, L., Zhao, H., Zhang, D., Li, Z., Zha, X., 2008. Unglycosylation at Asn-633 made extracellular domain of E-cadherin folded incorrectly and arrested in endoplasmic reticulum, then sequentially degraded by ERAD. *Glycoconj. J.* 25, 727–740. doi:10.1007/s10719-008-9133-9

REFERENCES

Zielinska, D.F., Gnad, F., Schropp, K., Wiśniewski, J.R., Mann, M., 2012. Mapping N-Glycosylation Sites across Seven Evolutionarily Distant Species Reveals a Divergent Substrate Proteome Despite a Common Core Machinery. *Mol. Cell* 46, 542–548.

APPENDIX

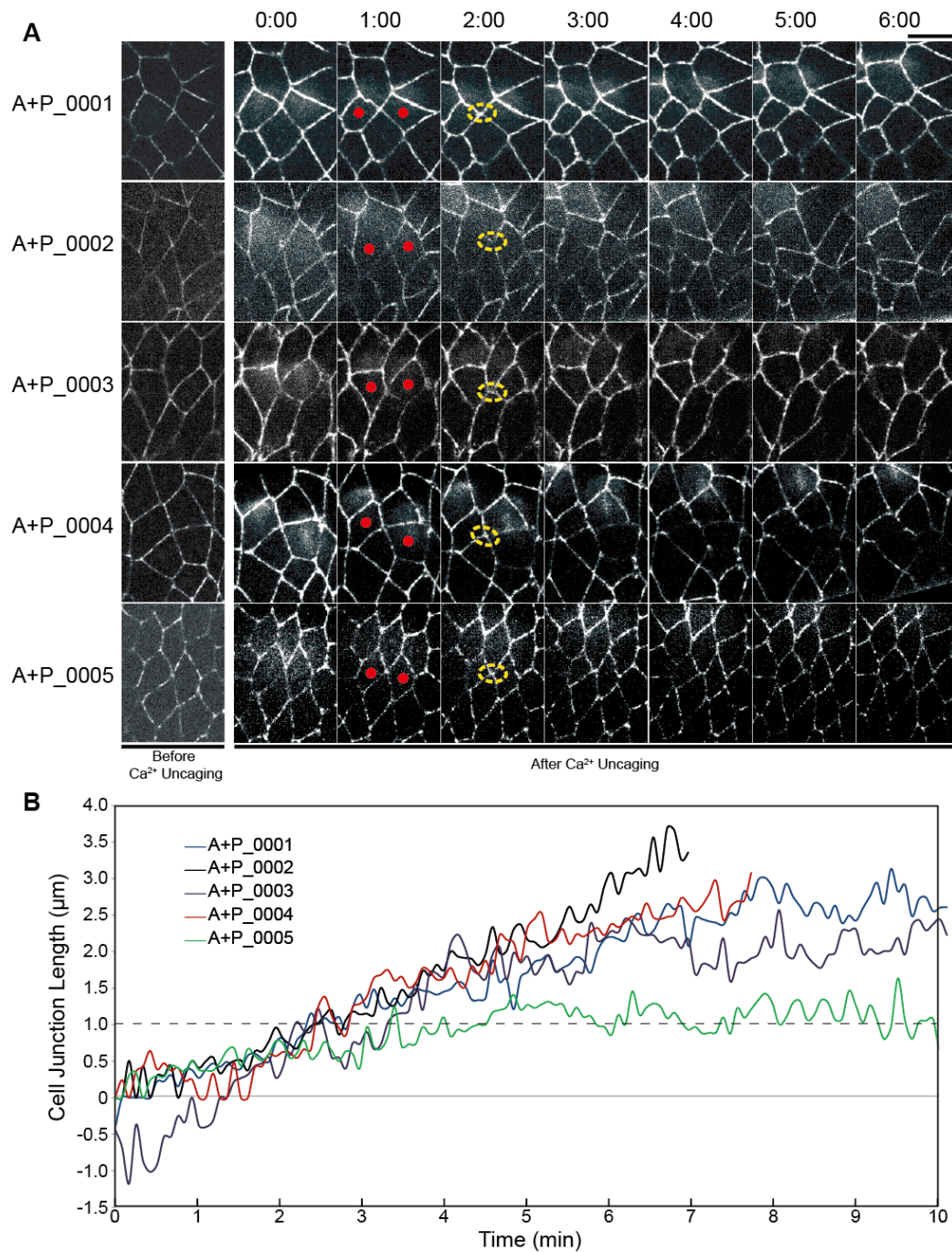


Figure A.1 Synchronous cell contractions in anterior and posterior cells induce cell junction formation in AP direction (relevant to Figure 4.2A).

(A) The images from the time-lapse recording from the individual Ca²⁺ uncaging experiments. The cell outlines were visualized by E-Cad-GFP. The target cells are indicated by red dots and the yellow dash cycles indicate the new junctions. Scale bar, 5 μm . (B) Length of cell junctions, the positive and negative values were measured from the AP and DV junctions respectively.

APPENDIX

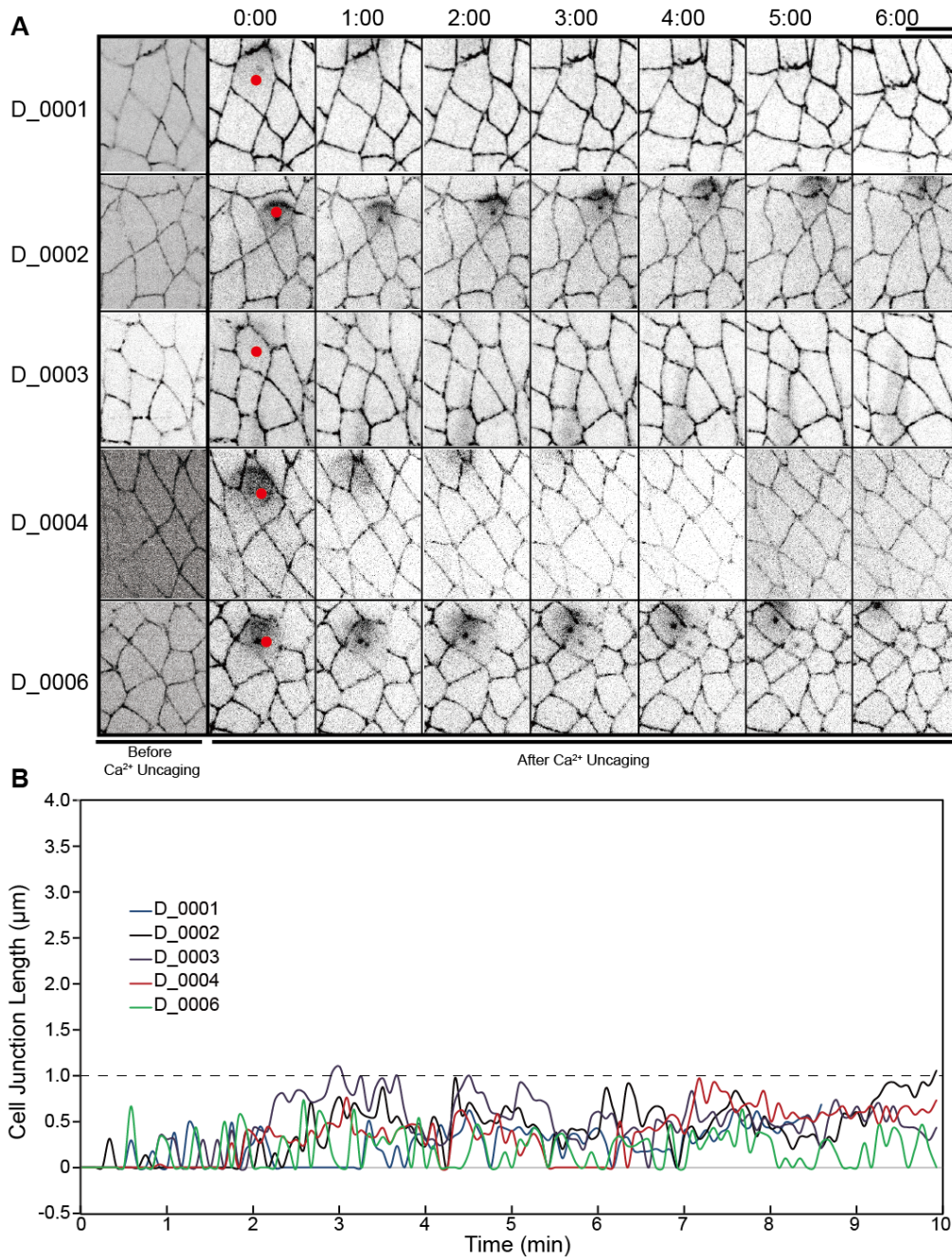


Figure A.2 Cell contractions in dorsal cell block the new junction formation (relevant to Figure 4.2D).

(A) The images from the time-lapse recording from the individual Ca²⁺ uncaging experiments. The cell outlines were visualized by E-Cad-GFP. The target cells are indicated by red dots. Scale bar, 5 µm. (B) Length of cell junctions, the positive and negative values were measured from the AP and DV junctions respectively.

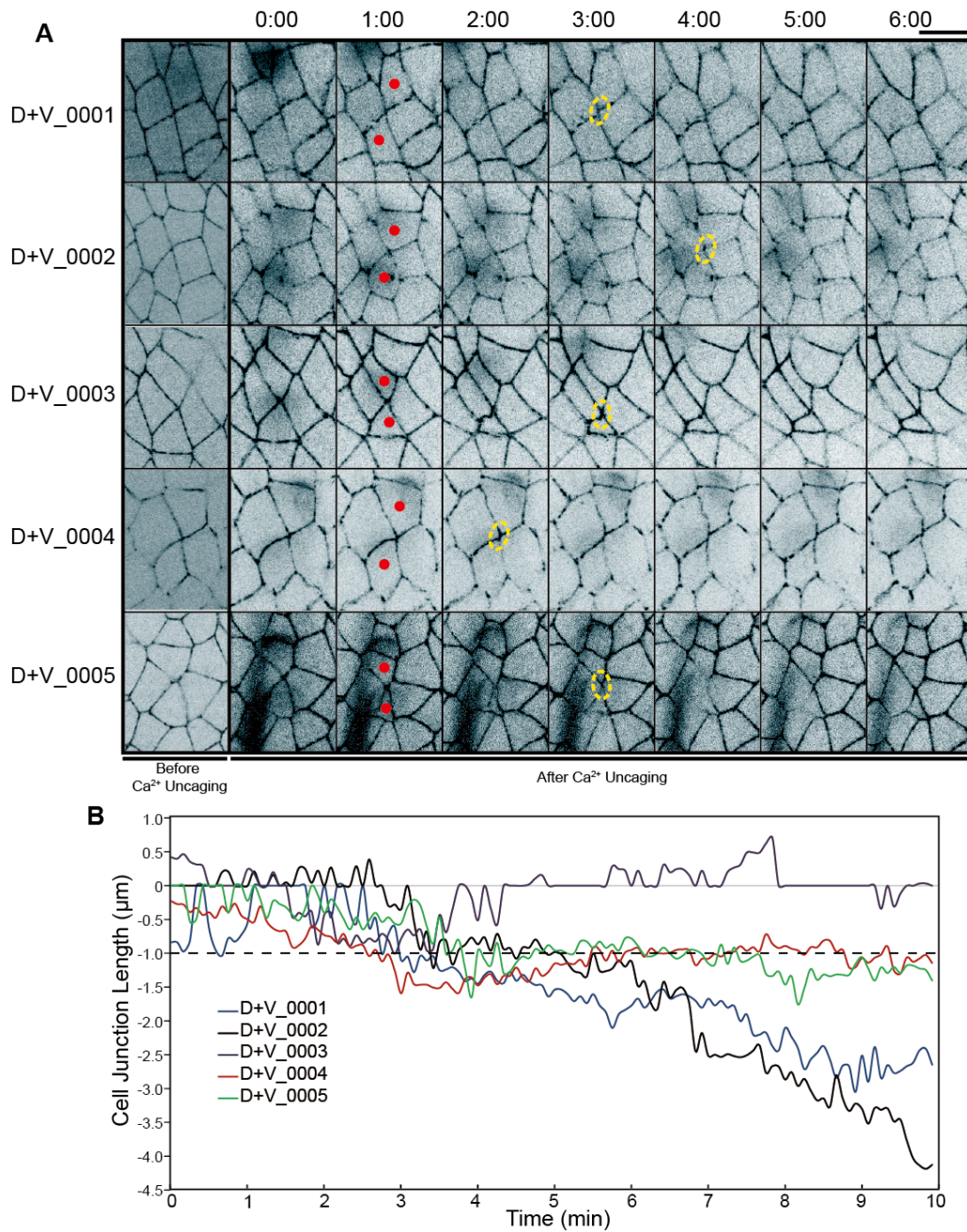


Figure A.3 Synchronous cell contractions in dorsal and ventral cells induce cell junction formation in DV direction (relevant to Figure 4.2B).

(A) The images from the time-lapse recording from the individual Ca²⁺ uncaging experiments. The cell outlines were visualized by E-Cad-GFP. The target cells are indicated by red dots and the yellow dash cycles indicate the induced junctions. Scale bar, 5 μm. (B) Length of cell junctions, the positive and negative values were measured from the AP and DV junctions respectively.

APPENDIX

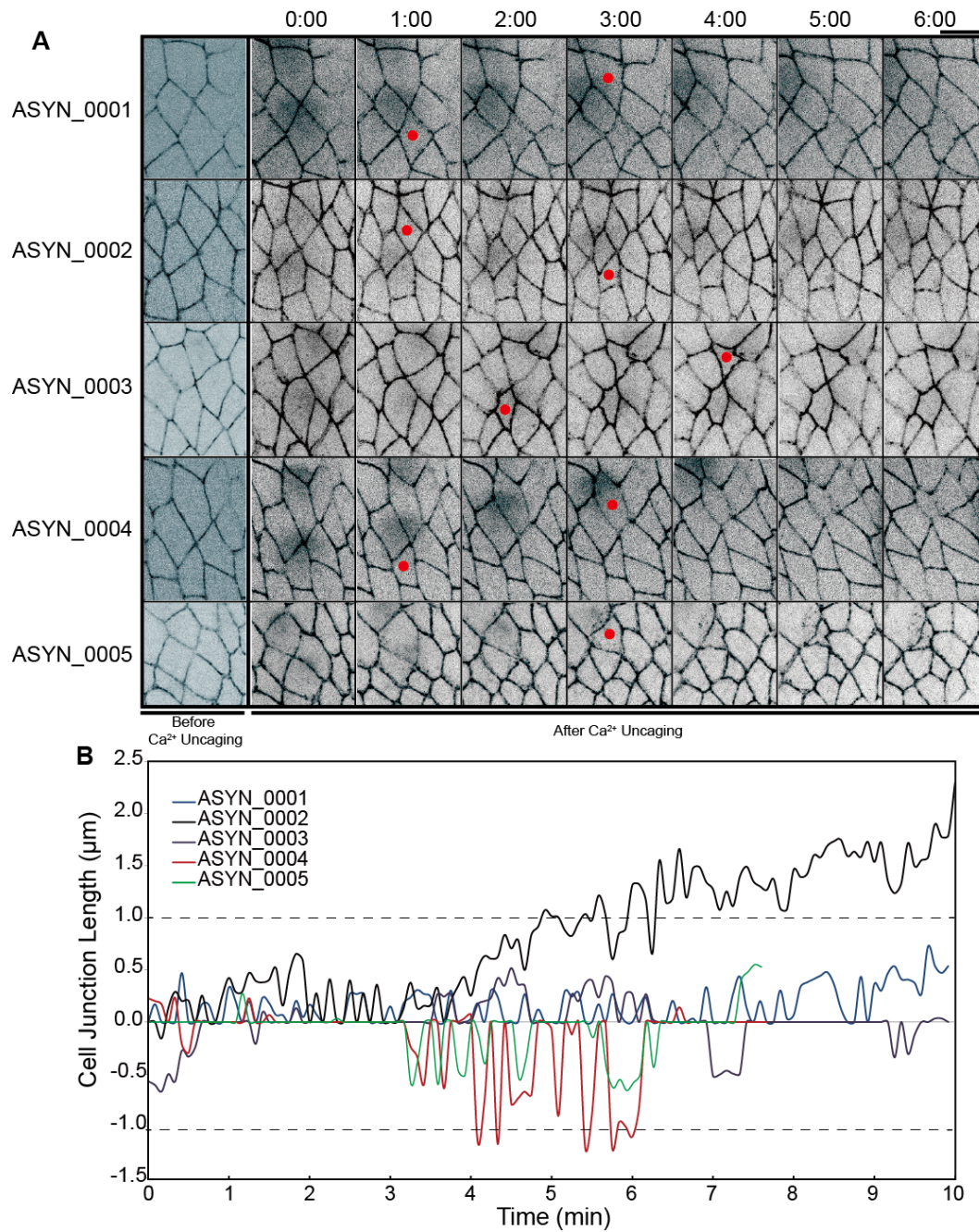


Figure A.4 Asynchronous cell contractions in dorsal and ventral cells fail to induce cell junction formation in DV direction (relevant to Figure 4.2C).

(A) The images from the time-lapse recording from the individual Ca²⁺ uncaging experiments. The cell outlines were visualized by E-Cad-GFP. The target cells are indicated by red dots. Scale bar, 5 µm. (B) Length of cell junctions, the positive and negative values were measured from the AP and DV junctions respectively.

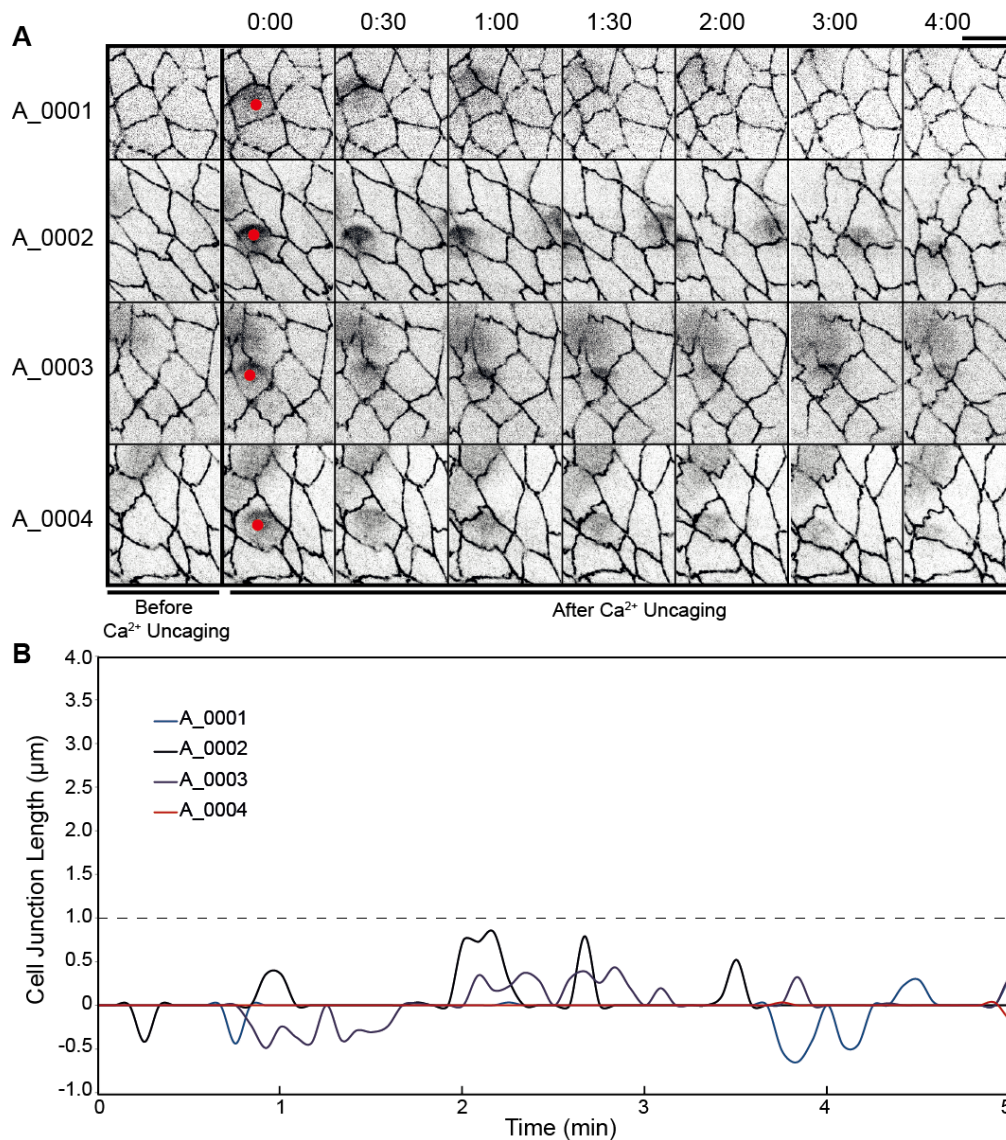


Figure A.5 Cell contractions in anterior cells fail to induce cell junction formation in AP direction in *xit* embryos (relevant to Figure 4.5A).

(A) The images from the time-lapse recording from the individual Ca²⁺ uncaging experiments. The cell outlines were visualized by E-Cad-GFP. The target cells are indicated by red dots. Scale bar, 5 µm. (B) Length of cell junctions, the positive and negative values were measured from the AP and DV junctions respectively.

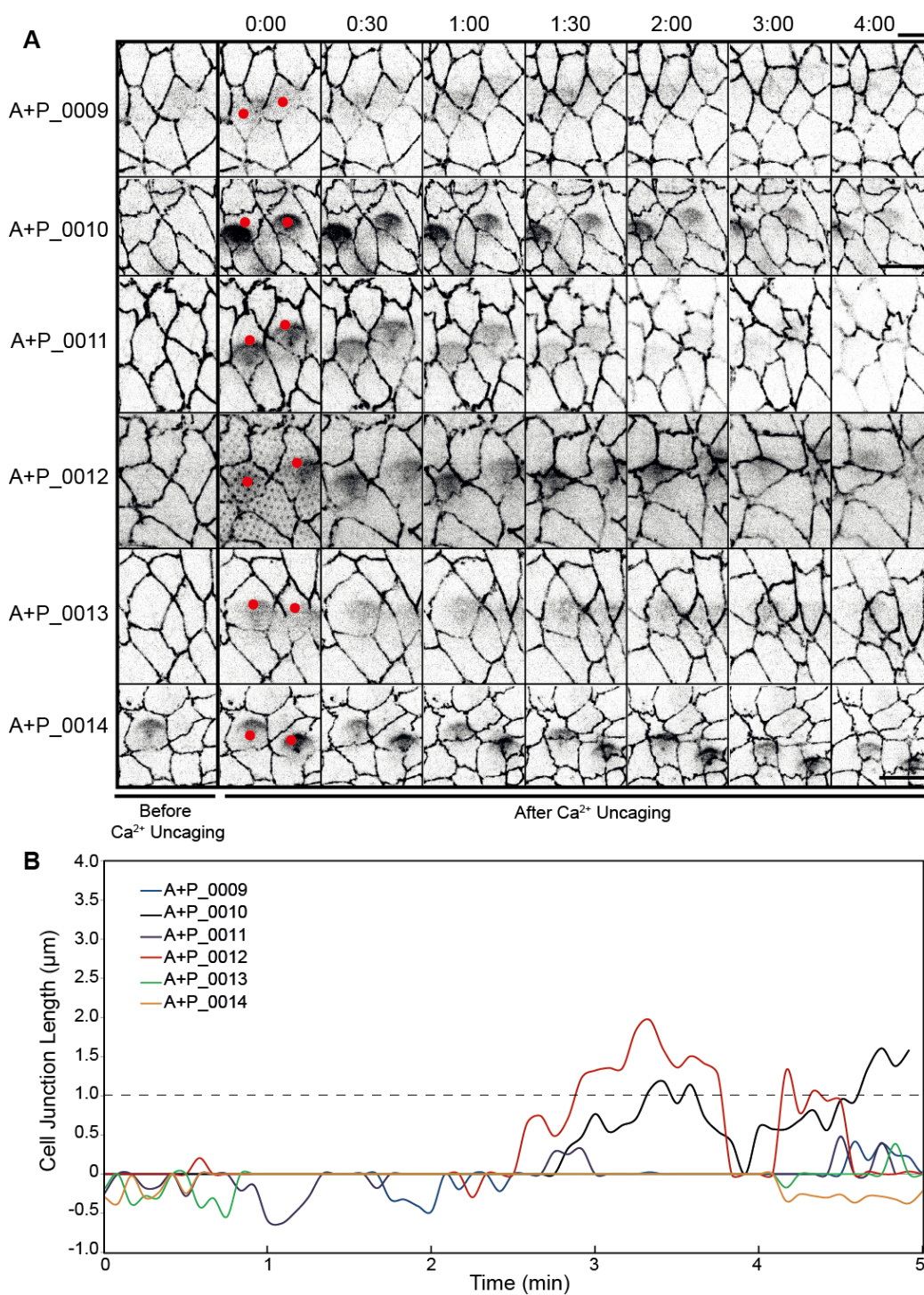
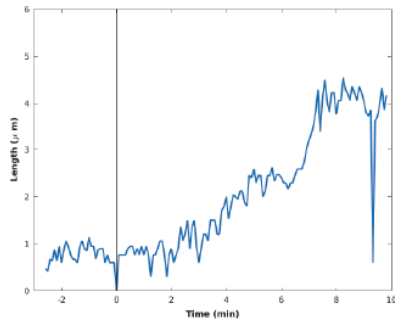
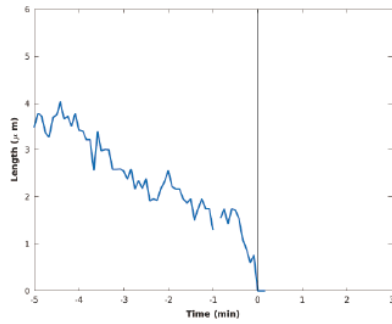
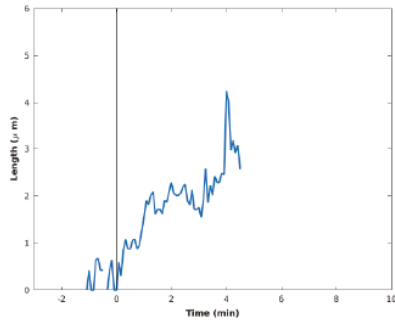
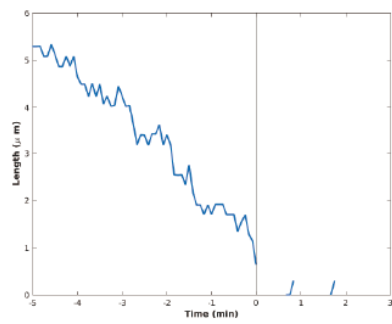
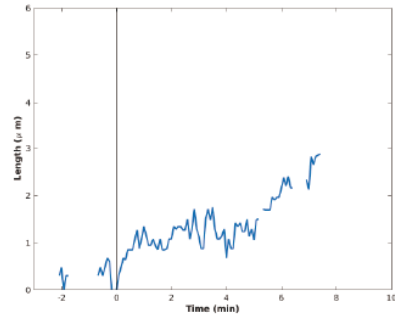
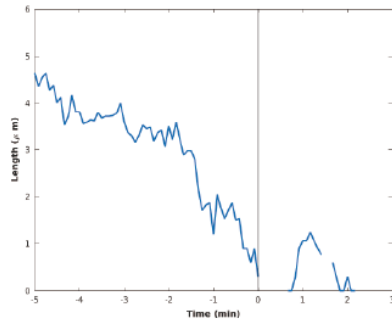
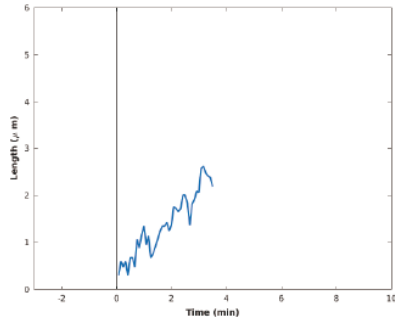
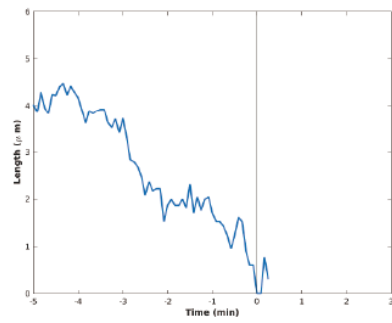
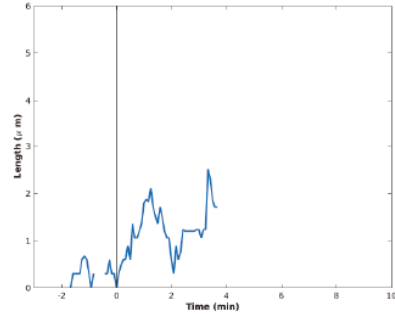
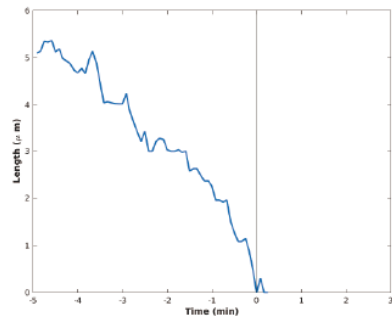


Figure A.6 Synchronous cell contractions in anterior and posterior cells fail to induce cell junction formation in AP direction in *xit* mutant embryos (relevant to Figure 4.5B).

(A) The images from the time-lapse recording from the individual Ca²⁺ uncaging experiments. The cell outlines were visualized by E-Cad-GFP. The target cells are indicated by red dots. Scale bar, 5 μm . (B) Length of cell junctions, the positive and negative values were measured from the AP and DV junctions respectively.

APPENDIX



APPENDIX

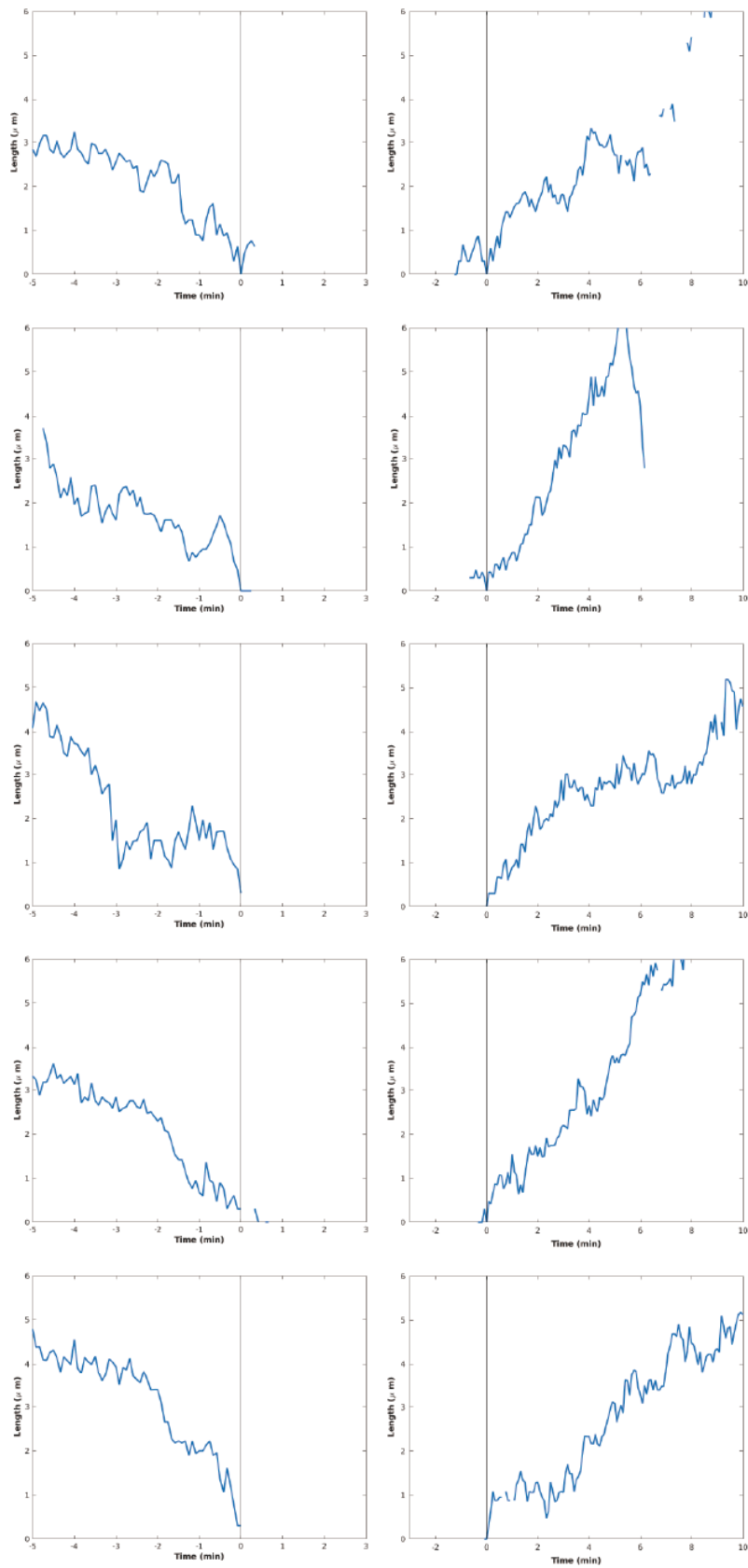
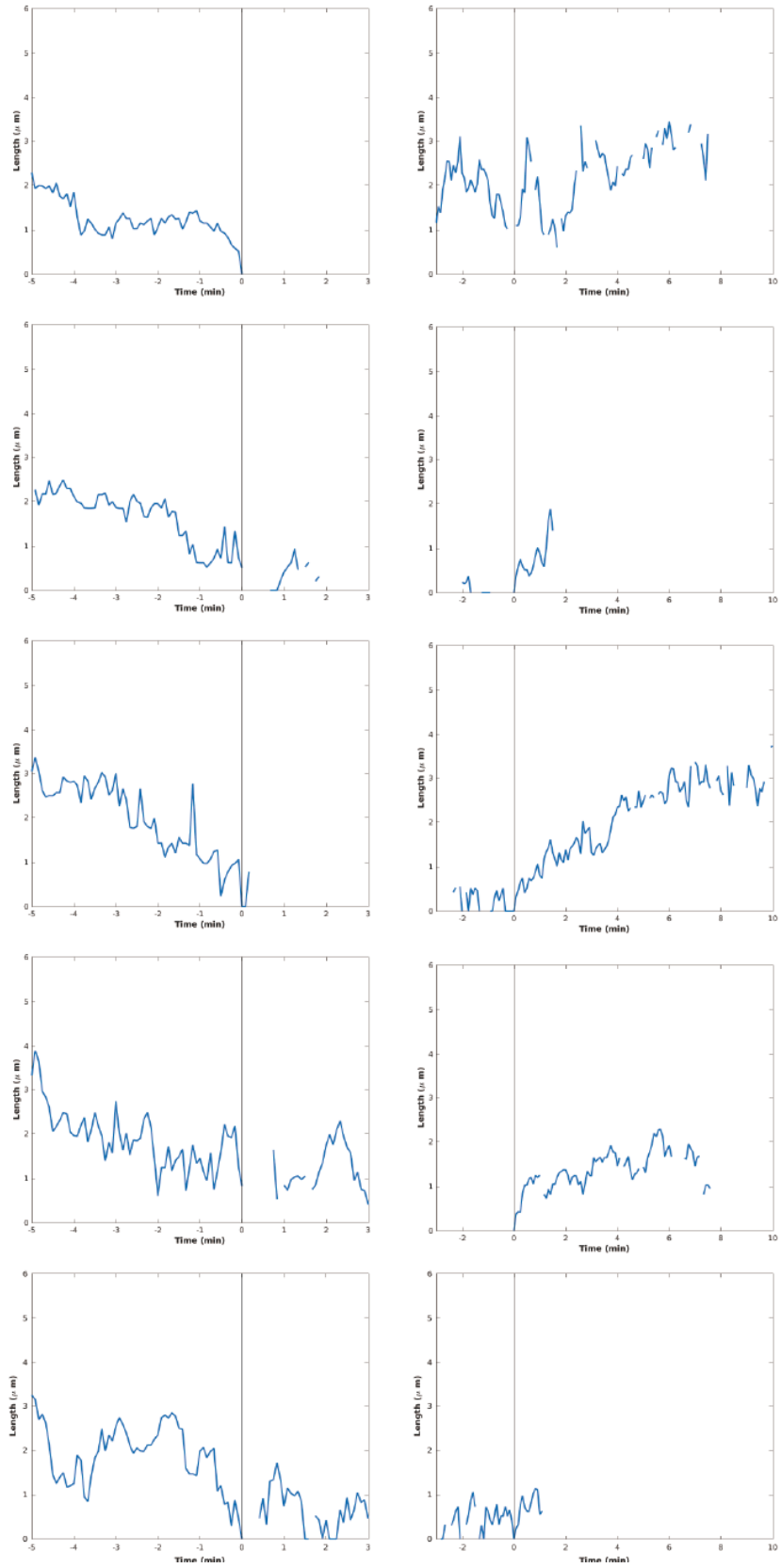


Figure A.7 Junctions in 10 individual cell quadruplets during T1 transitions in wild type embryos.

The junction length was aligned with the first (left panel) and last (right panel) 4x vertex. The measurements are the length of AP junctions (left panel) in collapse phase and the DV junctions (right panel) in the extension phase, relevant to Figure 4.10.

APPENDIX



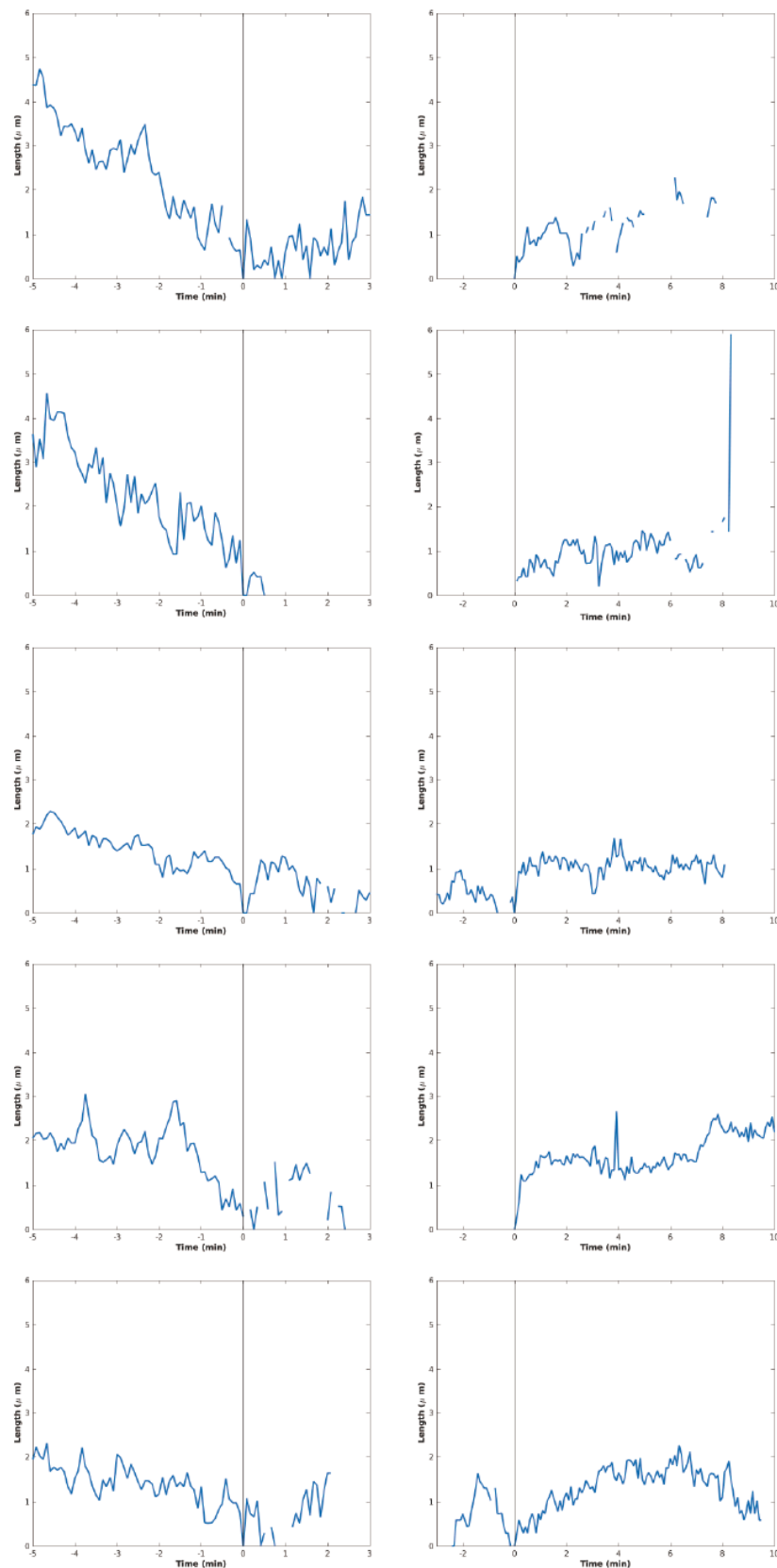


Figure A.8 Junctions in 10 individual cell quadruplets during T1 transitions in *xit* embryos.

The junction length was aligned with the first (left panel) and last (right panel) 4x vertex. The measurements are the length of AP junctions (left panel) in collapse phase and the DV junctions (right panel) in the extension phase, relevant to Figure 4.10.

APPENDIX

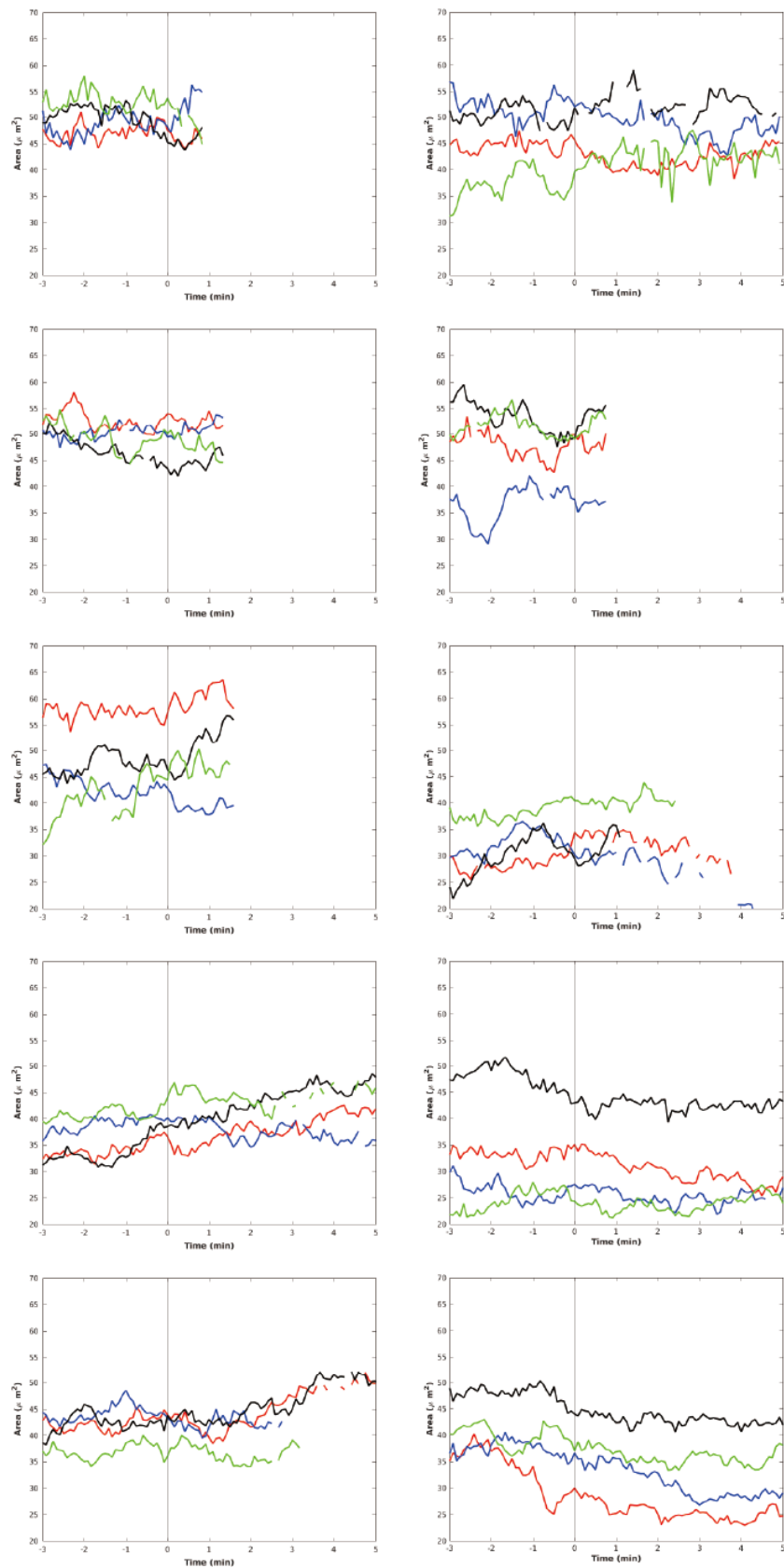


Figure A.9 Cell area dynamics in 10 individual cell quadruplets during T1 transitions in wild type embryos.

The areas were aligned with the first 4x vertex. The areas from different cells by different colors, A, red, P, blue, D, black, and V, green. relevant to Figure 4.11.

APPENDIX

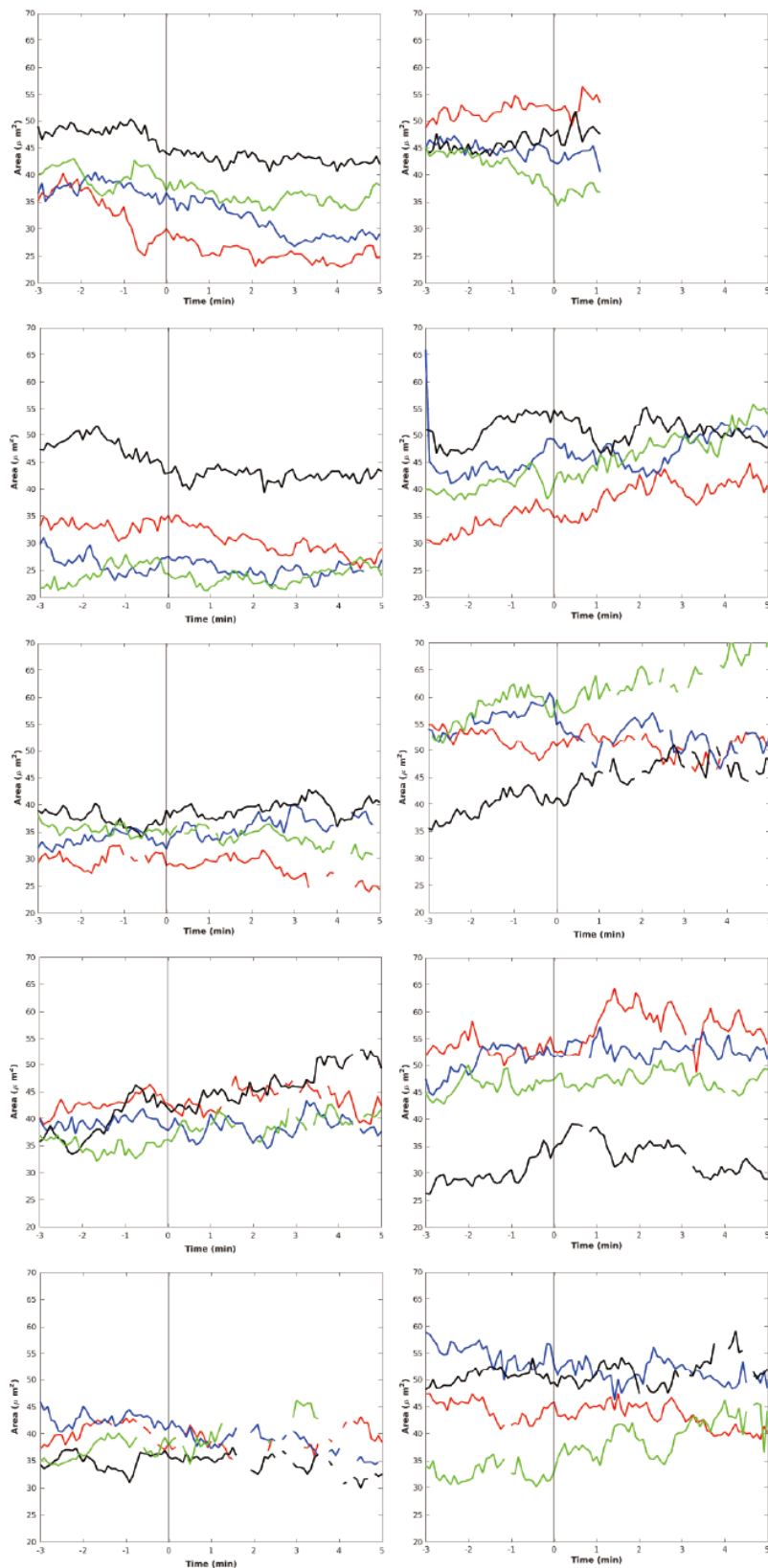


Figure A.10 Cell area dynamics in 10 individual cell quadruplets during T1 transitions in *xit* embryos. The areas were aligned with the first 4x vertex. The areas from different cells by different colors, A, red, P, blue, D, black, and V, green. relevant to Figure 4.11.

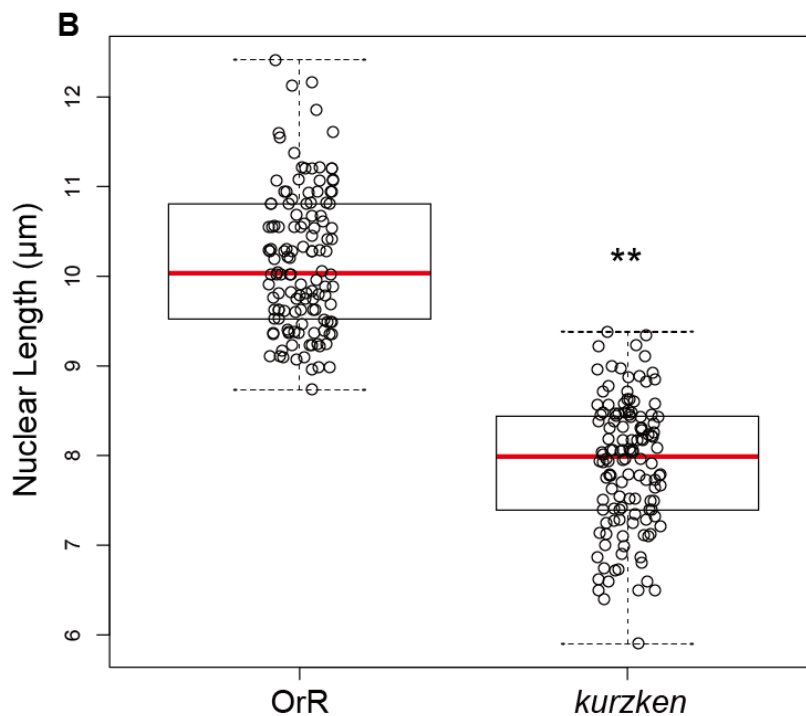
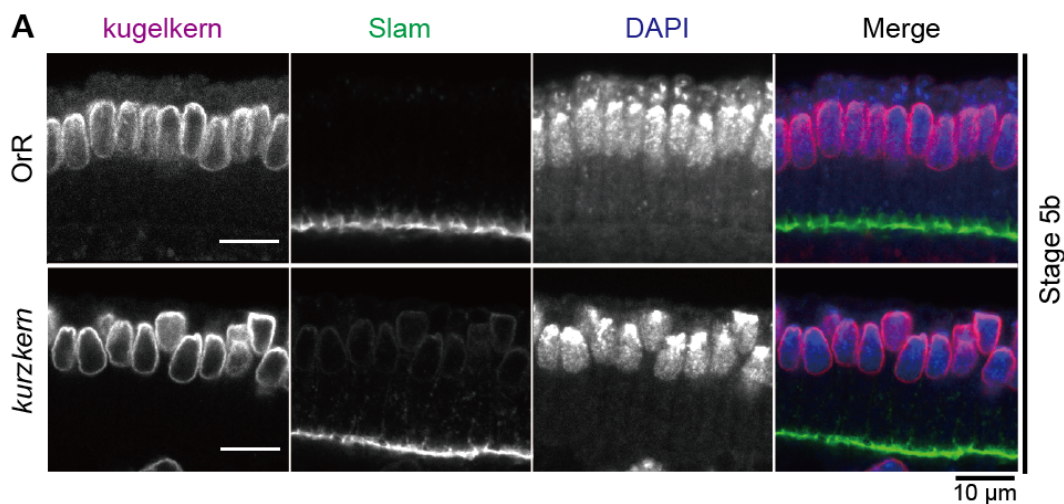


Figure A.11 Nuclear elongation is affected during cellularization in *kurzken* embryos.

xit mutant is carried in X330 line. Shorter nuclear during cellularization is another phenotype in X330 line. The putative mutant is named "*kurzkern*". (A) Images from the fixed wild type and *kurzken* embryos stained with Kugelkern (nuclear envelop), Slam (furrow canal, basal) and DAPI at stage 5b. (B) Nuclear length (apical-basal) was significantly shorter in *kurzken* embryos at stage 5b. The stage of embryos was based on Slam staining. Red horizontal line, mean. Box, second and third quartiles. Black horizontal dash line with whisker, maximums and minimums. $P < 0.0001$, the P values are calculated from paired Student's t -tests. $N = 130$ nucleus from 5 wild type and *kurzken* embryos respectively.

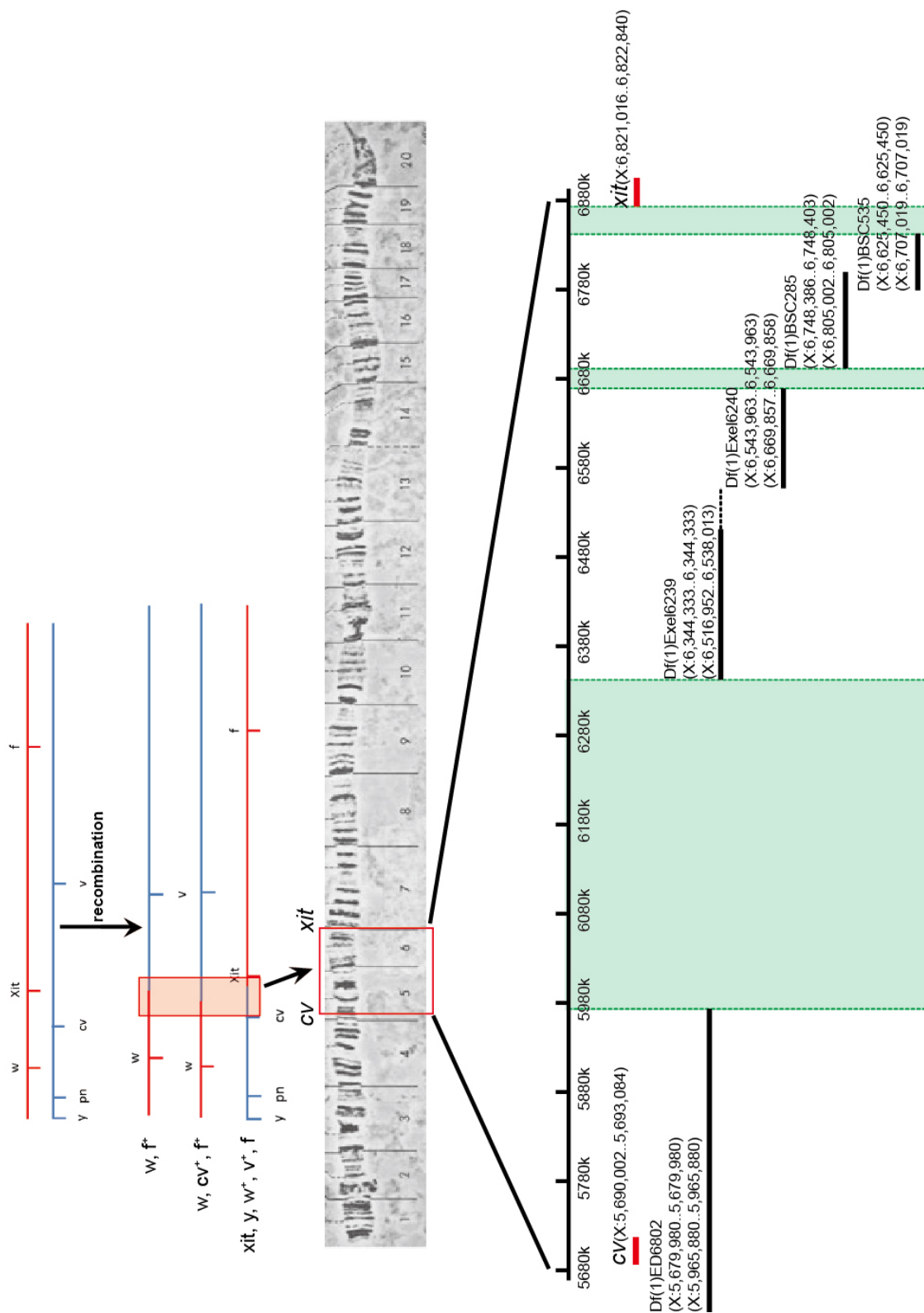


Figure A.12 Mapping of *kurz kern*.

Mapping of *kurz kern* by *xit* lethality and deficiencies. *kurz kern* localizes at the green region. I did the mapping of *kurz kern* based on meiosis recombination. *Kurz kern* is a viable allele, and *kurz kern* gene locates at 5' of *xit*.

LIST OF FIGURES

Figure 1.1 <i>Drosophila</i> embryonic germ-band extension.....	4
Figure 1.2 Anterior-posterior patterning system and polarized planar polarity.....	6
Figure 1.3 Germ-band extension is driven by cell intercalation.....	9
Figure 1.4 Actomyosin dynamics within the cell quadruplets during the T1 transition.	15
Figure 1.5 Methods for mechanical forces measurement <i>in vivo</i>	23
Figure 2.1 Schema of the response of target cells for different size of UV-laser illumination.	42
Figure 3.1 <i>xit</i> is required for germ-band extension.....	46
Figure 3.2 Schematic representation of genomic rescue of <i>xit</i> mutants.....	46
Figure 3.3 <i>xit</i> encodes a glucosyltransferase.	47
Figure 3.4 Xit colocalises with KDEL and reticulon.	48
Figure 3.5 Xit and E-Cadherin are required for germ-band extension.	49
Figure 3.6 Xit and E-Cadherin are required for new junction formation during T1 transitions.	50
Figure 3.7 Embryonic polarities in <i>xit</i> mutants.....	51
Figure 3.8 Xit is required for E-Cadherin distribution.	52
Figure 3.9 Xit is required for the polarized secretion of E-Cadherin.....	53
Figure 3.10 Overexpression of E-Cadherin in embryos.	55
Figure 3.11 E-Cadherin is Hypo-N-glycosylated in <i>xit</i> mutants.	56
Figure 3.12 Western blots of total lysates treated by Endo H with E-Cadherin antibody.	57
Figure 3.13 Adherens junctions are not obviously affected in <i>xit</i> mutants.	58
Figure 3.14 E-Cadherin protein level is reduced by RNAi treatment.....	59
Figure 3.15 Dynamics of E-Cadherin are affected in <i>xit</i> mutants.	60
Figure 3.16 E-Cadherin clusters are more mobile in <i>xit</i> mutants.	61
Figure 3.17 E-Cadherin clusters mobility is normal at the early stage in <i>xit</i> mutants. ...	62
Figure 3.18 Developmental control of E-Cadherin clusters mobility.....	63

LIST OF FIGURES

Figure 3.19 E-Cadherin cluster size is reduced in <i>xit</i> mutants.	64
Figure 3.20 E-Cadherin clusters mobility is increased by Myosin-II in <i>xit</i> mutant.	65
Figure 3.21 Cell morphology in Amnioserosa in <i>Drosophila</i> embryos.....	66
Figure 3.22 Oscillatory dynamics are correlative between neighboring cells in amnioserosa.....	67
Figure 3.23 Morphology of amnioserosa in wild type and <i>xit</i> embryos.....	69
Figure 3.24 Response of neighboring cells depends on <i>xit</i> in amnioserosa.	70
Figure 3.25 Xit increases recoil velocity at the junctions after UV-laser cut.....	71
Figure 3.26 Amnioserosa cell oscillation period is reduced in <i>xit</i> mutants.	72
Figure 4.1 Schematic representation of T1 transitions.....	75
Figure 4.2 Ca^{2+} uncaging in cell quadruplets undergoing T1 transitions in wild type embryos.....	76
Figure 4.3 Cell contraction by Ca^{2+} uncaging.....	77
Figure 4.4 Ca^{2+} uncaging in cell quadruplets undergoing T1 transitions in <i>xit</i> embryos.	78
Figure 4.5 Response of neighboring cells depends on <i>xit</i> in germ-band epithelial cells.	79
Figure 4.6 Schematic illustration of the overview of the data analysis.	80
Figure 4.7 Diverse behaviors of cell quadruplets.	81
Figure 4.8 Alignment of T1 transitions.....	82
Figure 4.9 Prolonged attempt phase in <i>xit</i> mutants.....	83
Figure 4.10 Averaged junction in cell quadruplets during T1 transitions.	84
Figure 4.11 Averaged area dynamics in cell quadruplets during T1 transitions.....	85
Figure 4.12 Correlated area change in cell quadruplets during T1 transitions.....	86
Figure 4.13 Cell coordination depends on Xit and E-Cadherin.	89
Figure 4.14 Prolonged attempt phase in E-Cadherin RNAi embryos.....	90
Figure 5.1 ER N-glycosylation and quality control.....	91
Figure 5.2 Schematic representation of E-Cadherin is hypo-N-glycosylated in <i>xit</i> mutants.....	92

LIST OF FIGURES

Figure 5.3 Role of N-Glycans in E-Cadherin localization and functions in <i>Drosophila</i> embryos.....	93
Figure 5.4 N-glycosylation alters the immobilization of E-Cadherin clusters and E-Cadherin-based mechanotransduction in <i>Drosophila</i> embryos.....	97
Figure 5.5 Coordinated cell area fluctuations drive expansion of new junctions during cell intercalation in <i>Drosophila</i> embryos.....	100
Figure 6.1 Scheme of Ca ²⁺ uncaging in epidermal in <i>Drosophila</i> embryos.....	104
Figure 6.2 Uncaging induces rapid intracellular Ca ²⁺ concentration increase in epithelial target cells.....	106
Figure 6.3 Ca ²⁺ uncaging induces rapid contraction of epidermal cells.	108
Figure 6.4 Apical area dynamics of target cell over 15 minutes.....	109
Figure 6.5 Myosin II dynamics in target cells.	110
Figure A.1 Synchronous cell contractions in anterior and posterior cells induce cell junction formation in AP direction (relevant to Figure 4.2A).	127
Figure A.2 Cell contractions in dorsal cell block the new junction formation (relevant to Figure 4.2D).	128
Figure A.3 Synchronous cell contractions in dorsal and ventral cells induce cell junction formation in DV direction (relevant to Figure 4.2B).....	129
Figure A.4 Asynchronous cell contractions in dorsal and ventral cells fail to induce cell junction formation in DV direction (relevant to Figure 4.2C).....	130
Figure A.5 Cell contractions in anterior cells fail to induce cell junction formation in AP direction in <i>xit</i> embryos (relevant to Figure 4.5A).....	131
Figure A.6 Synchronous cell contractions in anterior and posterior cells fail to induce cell junction formation in AP direction in <i>xit</i> mutant embryos (relevant to Figure 4.5B).	132
Figure A.7 Junctions in 10 individual cell quadruplets during T1 transitions in wild type embryos.....	134
Figure A.8 Junctions in 10 individual cell quadruplets during T1 transitions in <i>xit</i> embryos.....	136

LIST OF FIGURES

Figure A.9 Cell area dynamics in 10 individual cell quadruplets during T1 transitions in wild type embryos.....	137
Figure A.9 Cell area dynamics in 10 individual cell quadruplets during T1 transitions in <i>xit</i> embryos	138
Figure A.11 Nuclear elongation is affected during cellularization in <i>kurzken</i> embryos.	139
Figure A.12 Mapping of <i>kurzkern</i>	140

LIST OF TABLES

Table 2.1 Oligonucleotides used in the study.....	26
Table 2.2 Primary antibodies used in the study.....	27
Table 2.3 Fly stocks used in the study.....	28
Table 2.4 Fly stocks generated in the study.....	30
Table 3.1 E-Cadherin protein levels in total embryonic extracts.....	56

LIST OF MOVIES

Movie 4.1 Synchronous cell contractions in anterior and posterior cells induce cell junction formation in AP direction.

Germ-band cell in embryos was expressing E-Cad-GFP. Ca^{2+} uncaging was applied in anterior and posterior cells in cell quadruplets. Target cells are indicated with yellow and red dots. New junction is indicated with green arrowhead. 4x vertices is indicated with red arrowhead. A stack was acquired every 5 s. Time is indicated as min:s. Anterior left, dorsal up. This movie relates to Figure 4.2A.

Movie 4.2 Synchronous cell contractions in dorsal and ventral cells induce cell junction formation in DV direction.

Germ-band cell in embryos was expressing E-Cad-GFP. Ca^{2+} uncaging was applied in dorsal and ventral cells in cell quadruplets. Target cells are indicated with yellow and red dots. New junction is indicated with green arrowhead. 4x vertices is indicated with red arrowhead. A stack was acquired every 5 s. Time is indicated as min:s. Anterior left, dorsal up. This movie relates to Figure 4.2B.

Movie 4.3 Asynchronous cell contractions in dorsal and ventral cells induce cell junction formation in DV direction.

Germ-band cell in embryos was expressing E-Cad-GFP. Ca^{2+} uncaging was applied in dorsal and ventral cells in cell quadruplets with 3 min gap. Target cells are indicated with yellow and red dots. 4x vertices is indicated with red arrowhead. A stack was acquired every 5 s. Time is indicated as min:s. Anterior left, dorsal up. This movie relates to Figure 4.2C.

Movie 4.4 Cell contractions in dorsal cells block cell junction formation in AP direction.

Germ-band cell in embryos was expressing E-Cad-GFP. Ca^{2+} uncaging was applied in dorsal cell in cell quadruplets. Target cells are indicated with red dot. 4x vertices is indicated with red arrowhead. A stack was acquired every 5 s. Time is indicated as min:s. Anterior left, dorsal up. This movie relates to Figure 4.2D.

Movie 6.1 Uncaging induces rapid intracellular Ca^{2+} concentration increase in epithelial target cells.

Germ-band cell in embryos was expressing UAS-myr-GCaMP6m, driving by maternal GAL4. Ca^{2+} uncaging was applied in single cell at $t = 0$. A stack was acquired every second. Time is indicated as seconds. Anterior left, dorsal up. This movie relates to Figure 6.2.

Movie 6.2 Ca^{2+} uncaging induces rapid contraction of epidermal cells.

Germ-band cell in embryos was expressing E-Cad-GFP. Ca^{2+} uncaging was applied in single. A stack was acquired every 5 s. Time is indicated as min:s. Anterior left, dorsal up. This movie relates to Figure 6.3.

ABBREVIATIONS

bp: base pairs

cDNA: complementary DNA

DAPI: 4', 6' – Diamidino-2-phenylindole

ddH₂O: double distilled water

°C: degree Celsius

DNA: deoxyribonucleic acid

EDTA: ethylenediaminetetraacetic acid

FRT: flippase recognition target

FRAP: fluorescence recovery after photobleaching

GFP: green fluorescent protein

g: gram(s)

h: hour(s)

kb: kilobases

kDa: kiloDalton

l: litre(s)

m: milli

μ: micro

min: minute(s)

s: second(s)

PCR: polymerase chain reaction

RNA: ribonucleic acid

RNAi: RNA interference

dsRNA: Double-stranded RNA

rpm: revolutions per minute

RT: room temperature

SDS: sodiumdodecylsulphate

SDS-PAGE: SDS-polyacrylamide gel electrophoresis

ABBREVIATIONS

Tris: tris(hydroxymethyl)aminomethne hydrochloride

Ca²⁺: calcium ion

STED: Stimulated emission depletion

LLO: lipid linked oligosaccharide

ER: Endoplasmic Reticulum

LIST OF PUBLICATIONS

Deqing Kong, Fred Wolf, Jörg Großhans. Forces directing germ-band extension in *Drosophila* embryos (review). *Mechanisms of Development*, 144 (2017) 11–22.

Yujun Zhang*, **Deqing Kong***, Lars Reichl, Nina Vogt, Fred Wolf, Jörg Großhans. The glucosyltransferase Xiantuan of the endoplasmic reticulum specifically affects E-Cadherin expression and is required for gastrulation movements in *Drosophila*. *Developmental Biology*, 390 (2014) 208–220.

* equally contribution

Susanne Karsch, **Deqing Kong**, Jörg Großhans, Andreas Janshoff. Single cell defects cause a collective and remote mechanical response in a confluent cell layer. *Biophysical Journal*, (2017).

Achintya Prahlad, Christian Spalthoff, **Deqing Kong**, Jörg Großhans, Martin C. Göpfert, Christoph F. Schmidt. Mechanical properties of a *Drosophila* larval chordotonal organ. *Biophysical Journal*, (2017), *in press*.

Manuscript in preparation

Deqing Kong, Fred Wolf, Jörg Großhans. Optochemical control of epithelial cell contractility at single cell resolution in *Drosophila* embryos.

Deqing Kong*, Lars Reichl*, Yujun Zhang, Adem Saglem, Stefan Eule, Fred Wolf, Jörg Großhans. Coordinated cell area fluctuations drive junction extension in epithelial cell quadruplets.

* equally contribution

CURRICULUM VITAE

Personal information

Name: Deqing Kong
Birthplace: Shaanxi, China
Citizenship: China
E-mail: deqingk@gmail.com

Education

2004 - 2008 Undergraduate studies of Veterinary medicine,
Northwest A&F University, Yangling, China

2008 Bachelor of Veterinary medicine

2009 - 2012 Graduate student, Zoology program.
Northwest A&F University, Yangling, China

2012 Master of Science

2012- present Doctoral thesis at Institute for developmental
biochemistry, University of Göttingen, Göttingen,
Germany

Göttingen, August, 2017